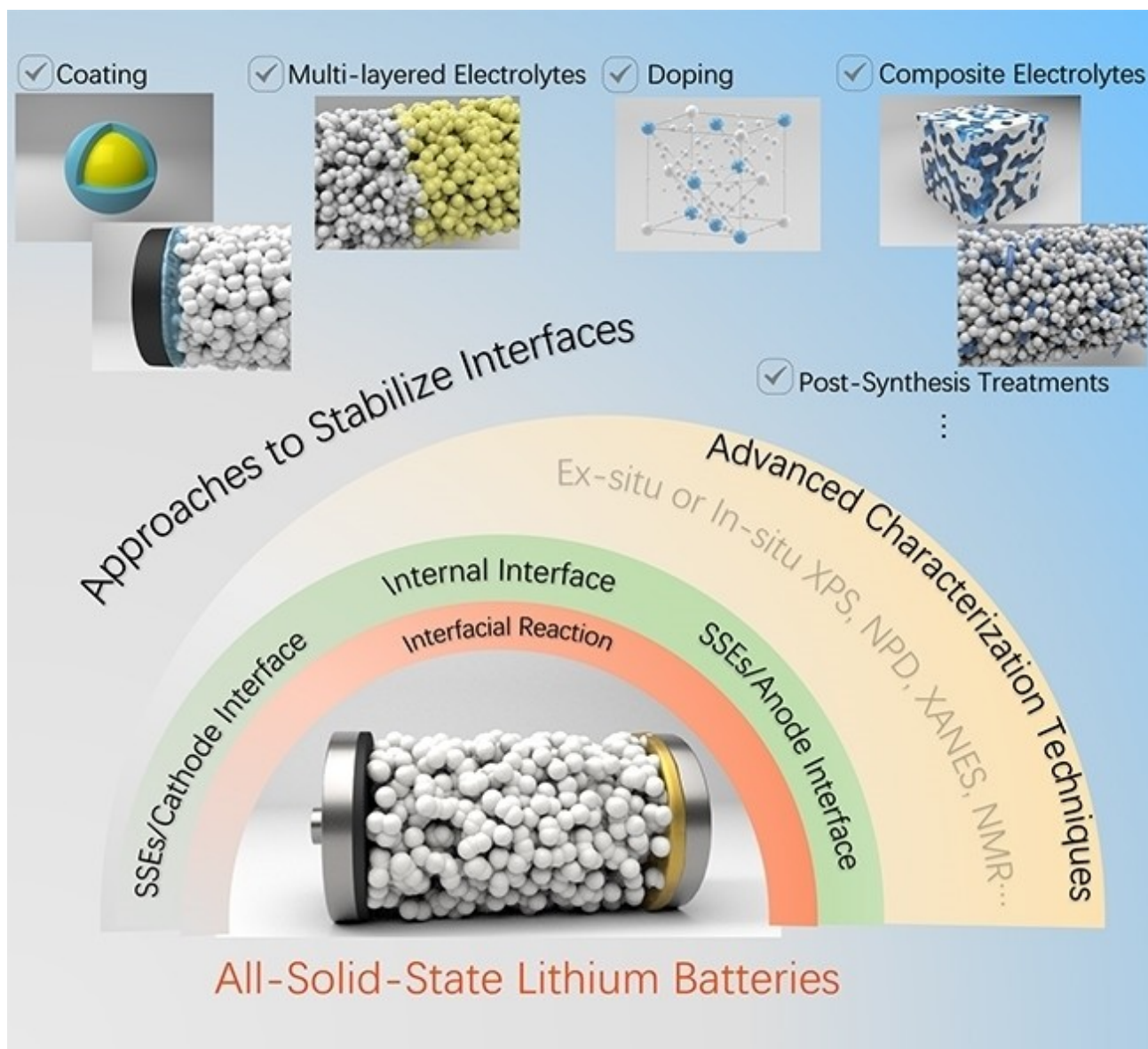


Interfacial Reactions in Inorganic All-Solid-State Lithium Batteries

Chao Zheng⁺^[a], Lujie Li⁺^[a], Kai Wang,^[a] Cheng Wang,^[a] Jun Zhang,^{*[a]} Yang Xia,^[a] Hui Huang,^[a] Chu Liang,^[a] Yongping Gan,^[a] Xinping He,^[a] Xinyong Tao,^[a] and Wenkui Zhang^{*[a]}



Replacing organic liquid electrolytes (LEs) in lithium-ion batteries (LIBs) with solid-state electrolytes (SSEs) to achieve all-solid-state lithium batteries (ASSLBs) with improved safety and potential higher energy density has been attracting growing attention for their wide application in various electronic devices, electric vehicles and renewable energy integration. To achieve high-performance ASSLBs, the design of SSEs with high ionic conductivity, easy processability, and compatible and stable interfaces with the cathode and anode has become a research priority in recent years. Among all the challenges and issues

concerning interfaces, the mechanisms and suppression methods of interfacial reactions are particularly important in the rational design of efficient electrolyte/electrode interfaces. This review mainly focuses on interfacial reactions in various types of inorganic ASSLBs and significant negative effects on battery performance. We also highlight advanced characterization methods and summarize some notable approaches to stabilize interfaces. Finally, we believe the scientific prospect of ASSLBs interface research will be helpful to keep pace with future research trends.

1. Introduction

The development and utilization of sustainable new energy has become an important basis for the sustainable development of human society. Over the past century, various energy storage devices including lead-acid battery,^[1] nickel battery,^[2] lithium ion battery,^[3] liquid flow battery,^[4] sodium sulfur battery^[5] and others^[6] have been developed. Among them, lithium ion batteries (LIBs) have been widely used in various electronic products because of their high working voltage, long cycle life and stable discharge performance.^[3] Lithium ion battery with organic liquid electrolytes (LEs) limits its application field, because liquid-type electrolytes are prone to flame, volatilize, leak and even corrode electrode.^[7] Although the use of gel polymer electrolyte alleviates the safety problem to some extent, it does not solve the problem fundamentally.^[8]

Based on such a background, the researchers focused on the field of solid-state electrolytes (SSEs). As a substitute for LEs, SSEs have the following obvious advantages:^[9] (1) SSEs are nonflammable and nonvolatile, which improve the safety of lithium battery; (2) SSEs have wider electrochemical windows and higher electrochemical stability, allowing for the adaptation of the high-voltage cathode materials; (3) SSEs allow the important possibility of achieving thin-film, miniaturized and flexible lithium battery, which can greatly improve the volumetric energy density; (4) Many researches have shown that solid electrolyte can effectively inhibit the growth of lithium dendrites. Using lithium metal (theoretical specific capacity of 3860 mAh g⁻¹) as anode can greatly improve the energy density of lithium battery; (5) SSEs facilitate the design of power energy system of lithium battery, which assembled with more single cells in series. In other words, all-solid-state lithium batteries (ASSLBs) are in line with the future development direction of chemical energy storage and electric vehicle technology.

SSEs mainly include two types, namely polymer SSEs and inorganic SSEs.^[10] Compared with polymer SSEs, inorganic SSEs have better thermal stability, higher ionic conductivity (0.1–100 mS cm⁻¹), lower activation energy (≤ 0.5 eV) and higher Li transference number ($t \approx 1$).^[11] The representative inorganic SSEs are sulfide-based SSEs,^[12] oxide-based SSEs^[13] and halide-based SSEs.^[14] Although inorganic SSEs have some merits which have been discussed above, ASSLBs based on inorganic SSEs face many difficulties for achieving a comparable electrochemical performance to conventional LIBs. Although SSEs have a comparable ionic conductivity with LEs, the unstable interface is a significant impact on the performance of ASSLBs.^[15] It's hard to experimentally identify the exact composition of interface resistances, however, previous researches suggest that electrochemical instability, chemical stability, mechanical properties and thermal stability may be the main reasons (Figure 1). These aspects can appear as the interfacial reactions inside SSEs or between electrodes and SSEs.^[16] According to the existing theoretical simulation and experimental data, the formation of interphase layers in ASSLBs may be caused by three mechanisms:^[17] (1) The reductions or oxidations of SSEs due to exceeded limited applied potential (electrochemical window) of SSEs materials; (2) The chemical reactions caused by the chemical incompatibility between SSEs and electrode materials; (3) The electrochemical reactions of the SSEs/electrodes interfaces during cycling.

In this review, we present recent advances about all kinds of interfacial reactions in inorganic ASSLBs, covering reaction mechanisms and methods. Beyond that, we also summarize other interface issues caused by interfacial reaction. In-situ and ex-situ characterizations currently used to study the reaction process also are highlighted. Finally, the challenges on interfacial reaction in ASSLBs are suggested as well.

2. A Brief Overview of Inorganic SSEs

This section will briefly review the progress of several types of inorganic SSEs. Table 1 lists a detailed summarization of some representative inorganic SSEs.

[a] C. Zheng,[†] L. Li,[†] K. Wang, C. Wang, J. Zhang, Y. Xia, H. Huang, C. Liang, Y. Gan, X. He, X. Tao, W. Zhang
College of Materials Science and Engineering
Zhejiang University of Technology
Hangzhou 310014 (China)
E-mail: zhangjun@zjut.edu.cn
msechem@zjut.edu.cn

[+] These authors contributed equally to this paper.

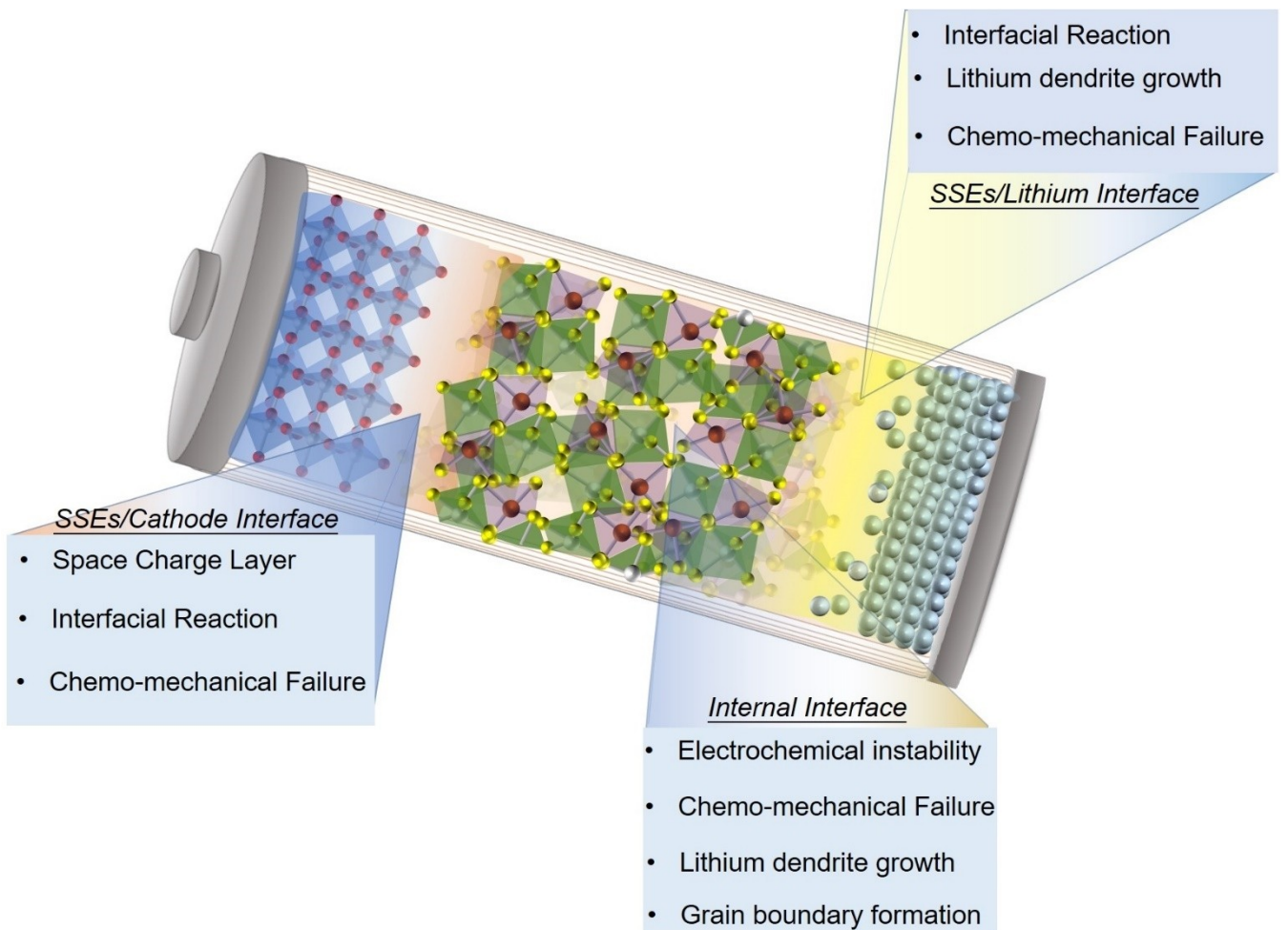
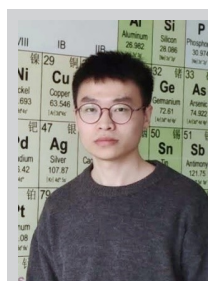


Figure 1. Schematic illustration of the various types of interface issues in ASSLBs with inorganic SSEs.



Chao Zheng received his bachelor's degree in Nanjing Tech University. He is currently a PhD candidate under the supervision of Prof. Wenkui Zhang and Prof. Jun Zhang in Zhejiang University of Technology. He is interested in the basic and applied research of solid-state electrolytes for rechargeable lithium batteries.



Lujie Li received her bachelor's degree in Luoyang Institute of Science and Technology. She is currently pursuing a Master's degree under the supervision of Prof. Jun Zhang in Zhejiang University of Technology. She is interested in high performance cathode materials and solid-state electrolytes for rechargeable lithium batteries.



Jun Zhang is an assistant professor of Materials Science and Engineering at Zhejiang University of Technology. He received his Ph. D. degree in 2012 from Zhejiang University. His research interests are in the area of rechargeable lithium batteries and electrochromic devices, including rational design and synthesis of advanced energy-storage and energy-saving materials.



Wenkui Zhang is a professor in College of Materials Science and Engineering, Zhejiang University of Technology. He received his Ph. D. degree in 1997 from Zhejiang University. His research activities focus mainly on advanced secondary batteries and energy storage/conversion materials such as lithium-ion batteries, lithium-sulfur batteries, fuel cells and supercapacitors.

Table 1. Summary of inorganic SSEs.

Type	Materials	$\sigma_{\text{RT}} [\text{S cm}^{-1}]$	E_a	Ref.	Advantages	Disadvantages
Sulfide	70Li ₂ S·30P ₂ S ₅ glass	3.7×10 ⁻⁵	43.5 kJ mol ⁻¹	[21]	↑ High ionic conductivity	↓ Relatively low electrochemical window
	75Li ₂ S·25P ₂ S ₅ glass	2.8×10 ⁻⁴	38.5 kJ mol ⁻¹	[21]	↑ Good mechanical flexibility	↓ Sensitive to moisture
	80Li ₂ S·20P ₂ S ₅ glass	1.3×10 ⁻⁴	42.3 kJ mol ⁻¹	[21]	↑ Low grain-boundary resistance	↓ Poor compatibility with cathode materials
	40Li ₂ S·28Si ₂ ·30LiI glass	1.8×10 ⁻³	N/A	[196]		↓ Thermodynamically not stable with lithium
	β -Li ₃ P ₂ S ₄	1.60×10 ⁻⁴	0.36	[24]		
	Li ₇ PS ₁₁	3.2×10 ⁻³	12 kJ mol ⁻¹	[20]		
	Li ₇ PS ₈	1.6×10 ⁻⁶	0.16 eV	[197]		
	Li ₆ PS ₅ Cl	1.9×10 ⁻³	0.22 eV	[36a]		
	Li ₆ PS ₅ Br	6.8×10 ⁻³	0.27 eV	[36a]		
	Li ₆ PS ₅ ·Si _{0.35} S _{0.65} Br	2.4×10 ⁻³	0.15 eV	[198]		
Oxide	Li _{3.25} Ge _{0.25} P _{0.75} S ₄	2.2×10 ⁻³	20 kJ mol ⁻¹	[19a]		↓ Brittle nature
	Li ₄ SnS ₄	7.0×10 ⁻⁵	0.41 eV	[31]		↓ Non-flexible
	Li ₁₀ GeP ₂ S ₁₂	1.2×10 ⁻²	24 kJ mol ⁻¹	[29]		↓ Expensive large-scale production
	Li _{1.0} SnP ₂ S ₁₂	4×10 ⁻³	0.60 eV	[33]		
	Li _{1.54} Si _{1.74} P _{0.54} Sn _{1.7} Cl _{0.3}	2.5×10 ⁻²	23 kJ mol ⁻¹	[34]		
	Li ₇ P _{2.9} Mn _{0.1} S _{0.17} O _{0.3}	5.6×10 ⁻³	20.8 kJ mol ⁻¹	[137d]		
	Li ₃ La _{0.51} TiO _{2.94}	1.00×10 ⁻³	0.40 eV	[52]		↑ High chemical and electrochemical stability
	Li _{0.38} La _{0.56} Ti _{0.99} Al _{0.01} O ₃	3.17×10 ⁻⁴	0.36 eV	[148]		↑ High mechanical strength
	Li _{0.25} La _{0.66} Ti _{0.75} Al _{0.25} O ₃	7.66×10 ⁻⁵	0.35 eV	[199]		↑ Stable in air
	Li _{1.2} Al _{0.82} Ti _{1.8} (PO ₄) ₃	5.00×10 ⁻³	0.29 eV	[200]		↑ Thermally stable at high temperatures
Halide	Li _{1.5} Al _{0.5} Ge _{1.5} (PO ₄) ₃	4.0×10 ⁻⁴	0.37 eV	[201]		
	Li ₇ Zr ₃ Zr ₂ O ₁₂	2.44×10 ⁻⁴	0.31 eV	[57]		
	Li ₆ Ba ₂ Ta ₂ O ₁₂	4.00×10 ⁻⁵	0.40 eV	[202]		
	Li ₅ Al ₂ Zr ₁₅ TiO ₉₆	4.4×10 ⁻⁴	0.49 eV	[203]		
	Li ₃ OCl	8.50×10 ⁻⁴	0.26 eV	[64]		↓ Sensitive to moisture
Other	Li ₃ OCl _{0.5} Br _{0.5}	1.94×10 ⁻³	0.18 eV	[64]		↓ Low oxidation voltage
	Li _{2.99} Ba _{0.005} ClO	2.5×10 ⁻²	< 0.6 eV	[204]		↓ Low ionic conductivity
	Li ₃ InCl ₆	1.49×10 ⁻³	N/A	[14b]		
	Li ₃ InB ₃ Cl ₃	1.2×10 ⁻⁴	20 kJ mol ⁻¹	[205]		
	Li ₃ PON	6.40×10 ⁻⁶	0.47 eV	[206]		↑ Stable with lithium
	Li _{3.3} PO _{3.9} N _{0.17}	2.00×10 ⁻⁶	0.65 eV	[70a]		↑ Stable with cathode materials
	LiBH ₄ ·(NH ₃ ·BH ₃)	4.04×10 ⁻⁴	0.12 eV	[74a]		↓ Low grain-boundary resistance
	3LiBH ₄ ·Li	5×10 ⁻⁵	N/A	[73]		↑ Good mechanical strength and mechanical flexibility
	Li(NH ₃) _n BH ₄	1.5×10 ⁻⁶	N/A	[74b]		↓ Thermodynamically not stable with lithium

2.1. Sulfide-Based SSEs

The sulfide-based SSEs are originated from the oxide-based SSEs. The oxygen element in the oxide body is replaced by the sulfur element to form the sulfide-based SSEs.^[18] Since there are no grains and grain boundaries in glass phase, the grain boundary impedance is effectively eliminated, so the ionic conductivity of glass sulfide SSEs is usually 1–2 orders of magnitude higher than their corresponding crystalline electrolytes. Among the binary LiS–GeS₅, Li₂S–B₂S₃ and Li₂S–P₂S₅, the most well-studied glass sulfide SSEs are the binary xLi₂S-(100-x)P₂S₅ system ($x=0.4\text{--}0.8$).^[19] In addition, some crystal and glass-ceramic sulfides have already been found in the Li₂S–P₂S₅ system: Li₇P₃S₁₁(70Li₂S·30P₂S₅),^[20] Li₃PS₄ (75Li₂S·25P₂S₅),^[21] Li₇PS₆ (88Li₂S·12P₂S₅),^[22] and Li₄P₂S₆ (67Li₂S·33P₂S₅).^[23] In the xLi₂S-(100-x)P₂S₅ system ($x \geq 70$), its ionic conductivity is higher than the original glass, due to the super-ionic metastable crystalline phases in the structure. But the ionic conductivity of glass-ceramic sulfides is mainly affected by the different phases and their compositions. “Nano-porous” β -Li₃PS₄ synthesized via wet chemistry have a sharply increased conductivity (1.6×10^{-4} S cm⁻¹ with an activation energy of 0.36 eV).^[24] Orthothiophosphate moieties (PS₄³⁻ tetrahedra) form the majority of the Li₃PS₄ structure.^[21,25] Crystalline Li₇P₃S₁₁ is composed of PS₄³⁻ and P₂S₇⁴⁻ anions, as an important member of LPS system because of its very high ionic conductivity (1.7×10^{-2} S cm⁻¹ at room temperature (RT)).^[26] Doping the LPS system with lithium salts (LiI, Li₃PO₄, Li₄SiO₄, Li₄GeO₄, LiBH₄, etc.) also can significantly enhance ionic conductivity and electrochemical stability.^[27]

Thio-LISICON (Lithium Superlonic CONductor) sulfides stemmed from aliovalent doping or various analogue solid solutions, the structural formula is Li_xM_{1-x}M'_yS₄ (M=Si, Ge; M'=P, Al, Zn, Ga, Sb).^[28] Among them, thio-LISICON Li_{4-x}Ge_{1-x}P_xS_{4-x} for $x=0.75$ show the highest ionic conductivity of 2.2×10^{-3} S cm⁻¹ at RT.^[29] The predicted ionic conductivity of Li₁₁AlP₂S₁₂ is 3.3×10^{-2} S cm⁻¹.^[30] The Li₄SnS₄ was discovered as a stable sulfide in air with an ionic conductivity of 7.1×10^{-5} S cm⁻¹ at 25 °C.^[31]

In recent years, the Li_{11-x}M_{2-x}P_{1+x}S₁₂ (M=Ge, Sn, and Si) family are attracting more attention. The Li₁₀GeP₂S₁₂ (LGPS) was designed and prepared by Kamaya et al.,^[29] which shows an extremely high ionic conductivity of 1.2×10^{-2} S cm⁻¹ at RT. The high ionic conductivity of Li₁₀GeP₂S₁₂ can be attributed to the fast 1D lithium transport tunnel in the c axis combined with the 2D lithium transport tunnel in the ab plane.^[32] As an isostructural alternative to LGPS, Li₁₀SnP₂S₁₂ has the advantages of low price and easy promotion, but it shows a lower ionic conductivity of 4×10^{-3} S cm⁻¹, because of a slightly different lithium ion disorder.^[33] Through series of doping, Li_{9.54}Si_{1.74}P_{1.44}S_{11.7}Cl_{0.3} was found to have an exceptional ionic conductivity of 2.5×10^{-2} S cm⁻¹ at RT, which is the highest reported ionic conductivity in SSEs so far.^[34]

Inspired by the cubic argyrodite Ag₈GeS₆, argyrodite-type Li₆PS₅X (X=Cl, Br, and I) SSEs^[35] with the ionic formula of (Li⁺)₆(PS₄³⁻)₂X⁻ were investigated. The ionic conductivities of argyrodite Li₆PS₅Cl, Li₆PS₅Br and Li₆PS₅I are 1.9×10^{-3} , 6.8×10^{-4} and 4.6×10^{-7} S cm⁻¹ at RT, respectively, the difference of which

three depends on the difference in anion disorder.^[36] To increase ionic conductivity or alleviate the poor Li/argyrodite interface problem, new argyrodite-type SSEs has been proposed by aliovalent substitution, including Li₆PS_{5-x}Se_xI,^[37] Li_{6+x}P_{1-x}Sn_xI,^[38] Li_{6+x}M_xSb_{1-x}S₅I (M=Si, Ge, Sn),^[39] Li_{6-2x}Zn_xPS_{5-x}O_xBr,^[40] Li_{6+x}P_{1-x}Ge_xS₅I,^[41] etc.

2.2. Oxide-Based SSEs

Oxide-based lithium ion conductive SSEs include NASICON-type, LISICON-type, perovskite-type, garnet-type. Their ionic conductivity is between $10^{-5}\text{--}10^{-3}$ S cm⁻¹. The oxide-based SSEs share advantages of high electrochemical and thermal stability, high mechanical strength, etc., while their disadvantages are poor ductility and high production cost.

The general formula of NASICON type solid electrolyte is MA₂(BO₄)₃ (M=Li, Na, K or Ag; A=Ti, Zr, Ge or V; B=P, Si or Mo).^[42] In 1976, Goodenough et al.^[43] obtained NASICON-type Na_{1+x}Zr₂P_{3-x}S_xO₁₂ by a high-temperature solid state reaction method. It is composed of PO₄ tetrahedron and ZrO₆ octahedron by common apex.^[44] Lithium ion solid electrolyte with NASICON structure can be obtained by replacing Na with Li. Compared with other M ions, LiTi₂(PO₄)₃ and LiGe₂(PO₄) have higher ionic conductivity, but they are still very low. In order to further increase the ionic conductivity, Ti is partially substituted. Li_{1+x}Al_xTi_{2-x}(PO₄)₃ (LATP) and Li_{1+x}Al_xGe_{2-x}(PO₄)₃ (LAGP) obtained by partially substituting Ti and Ge with Al doping. It can reach a high conductivity of $10^{-4}\text{--}10^{-3}$ S cm⁻¹ at RT.^[45]

LISICON refers to Li₁₄Zn(GeO₄)₄ and its doped derivatives. In 1978, Hong et al.^[46] synthesized this substance, which conductivity was 1.3×10^{-4} S cm⁻¹ at 300 °C, while the ionic conductivity was only 10^{-7} S cm⁻¹ at RT. It is essentially a solid solution of Li₄GeO₄ and Zn₂GeO₄, which Li₁₁Zn(GeO₄)₄³⁻ constitutes its anionic skeleton. Based on the excess lithium in the γ -Li₂ZnGeO₄ phase occupying the octahedral void position in the framework,^[47] the long distance between lithium ions and framework oxygen ions causes the Li–O bonds to be easily broken at high temperatures. Lithium ions move in the plane layer between the skeletons, so their activation energy is very low, only 0.24 eV.^[48] The solid solution of Li₄SiO₄–Li₃PO₄ containing XO₄³⁻ tetrahedron unit and Li–O polyhedron unit is also a LISICON structure electrolyte. This material has more lithium ions and voids, which in turn can have higher ionic conductivity.^[49]

In 1971, Takahashi et al.^[50] first reported perovskite-type solid electrolytes with the general formula ABO₃ (A=La, Sr, or Ca; B=Al or Ti). Perovskite is a face-centered cubic structure, where A is at the top corner of the cube, B is at the center of the body, and O is at the center of the face.^[51] In 1993, Inaguma et al.^[52] prepared Li_{3x}La_{2/3-x}TiO₃(LLTO) with a conductivity of 10^{-3} S cm⁻¹ at RT. LLTO belongs to the cubic crystal system and the space group is Pm $\bar{3}$ m. Titanium ions and oxygen ions form the TiO₆ octahedron structure, lithium ions and lanthanum ions are located in the gap formed by eight co-apex connected TiO₆ octahedra, and there are 12 O²⁻ around Li⁺.^[53] From the structural point of view, the ionic conductivity mainly depends

on the size of the A-site cation, the lithium ion and the vacancy concentration.^[54] In LLTO, lithium ions migrate through the vacancy transition mechanism in the framework. The concentration of the quadrilateral gap which formed by 4 oxygen directly affects the transition rate of lithium ion during the transition of lithium ion. The experimental results show that when the x is 0.11, the optimal ratio of lithium ion concentration and vacancy concentration in the framework of LLTO is achieved.^[55]

The chemical formula of garnet structure is $A_3B_2(XO_4)_3$ ($A=Ca, Mg, Fe, Mn$; $B=Al, Fe, Cr, Ti, Zr, V$), where A, B, and X have 8, 6, and 4 oxygen coordination. Thangadurai et al.^[56] first produced $Li_5La_3M_2O_{12}$ ($M=Ta$ or Nb) in 2003, with a conductivity of only $10^{-5} \text{ S cm}^{-1}$ and an activation energy of 0.6 eV. In 2007, Weppner's group^[57] obtained the cubic phase $Li_3La_3Zr_2O_{12}$ (LLZO) with a conductivity of $3 \times 10^{-4} \text{ S cm}^{-1}$ by doping substitution of M-site elements. The ZrO_6 octahedron and LaO_8 dodecahedron constitute the main structure of the material by edge-shared. Lithium atoms randomly occupy two kinds of sites in the structure, one is LiO_4 tetrahedron position (24d), and the other is LiO_6 octahedral position (48 g or 96 h).^[58] First-principle calculations reveal that the migration path of lithium ions in LLZO.^[59] Most of lithium ion is located in the octahedral gap, while very few are in the coplanar position of tetrahedron and octahedron. The coulomb force of a large number of lithium ion forces the original stable lithium ion to migrate at the 24d position, and the migration path is $96 \text{ h} \leftrightarrow 24\text{d} \leftrightarrow 96 \text{ h}$. The activation energy of this path is only 0.2–0.3 eV.

2.3. Halide-Based SSEs

The study of halide-based SSEs began in the 1830s.^[60] However, early halide-based SSEs have the low ionic conductivity at RT, so they did not receive widespread attention. Recently, the researches about halide have made a great progress and aroused considerable interest. Li_3MCl_6 , an inorganic fast ionic conductor based on halogens, was first reported in 1992.^[61] Its crystal is a monoclinic system with $C2/m$ space group. In this electrolyte system, the valence of halogen ions is -1 , and the coulomb interaction with lithium ions is weak, so its migration energy barrier is low. Therefore, when the carrier reaches a certain concentration, a higher ionic conductivity can be obtained. Halide-based SSEs can generally be synthesized by solid-phase ball milling using a halide precursor and then annealing. Tetsuya et al.^[62] reported a new type of halogen inorganic electrolyte system Li_3YCl_6/Li_3YBr_6 (LYC/LYB), which successfully combined high ionic conductivity, high chemical/electrochemical stability and plasticity, and preliminary its application in monolithic solid-state lithium batteries is studied. LYC has a hexagonal close-packed anion array, while LYB has a cubic close-packed anion array. Li^+ and Y^+ are both in octahedral voids, occupying two-thirds of the octahedral voids. For LYC with a hexagonal close-packed anion arrangement, lithium ion transport along the ab plane is achieved through tetrahedral sites and along c the transmission path of the axis is directly formed by the connection of adjacent octahedral sites.

For LYB with a cubic close-packed anion array, the lithium ion conduction paths in three directions are formed by the tetrahedral center sites connected. The AC impedance results show that the ionic conductivity of the LYC and LYB at RT are 0.51 mS cm^{-1} and 0.72 mS cm^{-1} , respectively. The Arrhenius relationship was used to fit the ionic conductivity behaviors of LYC and LYB at different temperatures. The activation energies of lithium ion migration in the electrolyte were calculated to be 0.40 eV and 0.37 eV, respectively. Li et al.^[14b] reported Li_3InCl_6 with high ionic conductivity at RT in 2019. Similar to LYB, Li_3InCl_6 has a distorted rock salt structure with an anionic cubic dense packing. The Li_3InCl_6 obtained by ball milling method and the subsequent low-temperature sintering method have the ionic conductivity of 0.84 and $1.49 \times 10^{-3} \text{ S cm}^{-1}$ at RT, respectively.^[63] Based on the theoretical research, the halide-based SSEs are expected to achieve higher ionic conductivity.

In 2012, Zhao et al.^[64] proposed an anti-perovskite family SSEs with a general formula of Li_3OX ($X=F, Cl, Br, I$). The Li_3OCl synthesized by grinding $LiOH$ and $LiCl$ precursors and then annealed has an ionic conductivity of $8.50 \times 10^{-4} \text{ S cm}^{-1}$. Li_3OCl can also be synthesized by high temperature and high pressure,^[65] quaternary ammonium salt method and wet chemical method. Recently, the fabrication of Li_3OCl solid electrolyte membranes by using Li_3OCl compound targets has also been reported.^[66] The Li_3OX unit cell is a simple cubic structure with a $Pm3(-)m$ space group. O atoms occupy the center of the cube, X atoms occupy the top corner of the cube, and lithium atoms occupy the face center of the cube. Doping the Br element at the Cl position can obtain a higher ionic conductivity. According to first-principles calculations, it is found that among different Br doping ratios, the $Li_3OCl_{0.75}Br_{0.25}$ structure has the highest ionic conductivity.^[67] Therefore, Li_3OCl is not a fast ion conductor in an ideal crystal and defects are the main driving force of the superionic conductors.^[68] In addition, Li_3OCl have the advantages of low activation energy, wide electrochemical window, stable contact with lithium, environmental friendliness, and low cost.^[66] In 2018, Shao et al.^[69] systematically modified the A and X positions of the anti-perovskite Li_3AX (introduced the S element at the A position and the I element at the X position), like Li_6SOI_2 and $Li_{25}O_4S_5I$. The diffusion activation energies of two anti-perovskite structures are 0.22 eV and 0.18 eV, respectively. The ionic conductivity at RT is 5 mS cm^{-1} and 12.5 mS cm^{-1} , which are much higher than the ionic conductivity at RT of perovskite Li_3OCl . Their electrochemical performance with lithium metal is stable, and the voltage platform stability window is 0–2.15 V vs. Li/Li^+ . This proposed a new research direction for solid electrolytes.

2.4. Others

Using Li_3PO_4 as a target material, Bates et al.^[70] fabricated an amorphous inorganic thin-film electrolyte $Li_{2.88}PO_{3.73}N_{0.14}$ (Li-PON) by magnetron sputtering under pure N_2 , which is already widely used in thin-film ASSLBs with the $1 \mu\text{m}$ thickness. Its ionic conductivity is $6.4 \times 10^{-6} \text{ S cm}^{-1}$ at RT and the electro-

chemical window can be up to 5.5 V (vs. Li/Li⁺). The thin-film ASSLBs show excellent cycle performance and can effectively inhibit the formation of lithium dendrite. Like other SSEs, LiPON also has good mechanical stability and compactness. In order to improve the ionic conductivity of LiPON, thin-film electrolyte LiSiPON was fabricated from a $(1-x)\text{Li}_3\text{PO}_4 \cdot x\text{Li}_2\text{SiO}_3$ target in a nitrogen reactive plasma.^[71] As the Si content increases, the ionic conductivity increases to $1.24 \times 10^{-5} \text{ S cm}^{-1}$, which shows broad applications and is worthy of development.

With the development of a series of research work about SSEs, new LiBH₄-based SSEs have attracted extensive attention due to its light weight, low grain boundary impedance, good ion selectivity, good stability against lithium and excellent mechanical property.^[72] The ionic conductivity of LiBH₄ at RT is only $10^{-8} \text{ S cm}^{-1}$,^[73] some promising strategies toward fast ion conductivity are to partially replace the BH₄⁻ anions by other anions (I⁻, Br⁻, Cl⁻, NH₂⁻, etc.), which stabilizes the high-temperature phase of LiBH₄ at lower temperatures.^[73-74] The ionic conductivity of 0.75LiBH₄·0.25LiI was almost three orders of magnitude than pristine LiBH₄.^[73,75] By introducing NH₃·BH₃ (AB) molecule into the lattice of LiBH₄, the fast ion conductor (LiBH₄)₂·AB ($1.47 \times 10^{-5} \text{ S cm}^{-1}$ at RT) and LiBH₄·AB ($4.04 \times 10^{-4} \text{ S cm}^{-1}$ at RT) hydrides were synthesized.^[75]

3. Stabilities and Interfaces of Inorganic SSEs

As shown in Figure 1, the formation of interphase layers occurs in three areas in ASSLBs with inorganic SSEs. In this section, we survey the issues associated with interfacial reactions and then introduce corresponding theories and characterization methods.

3.1. Electrochemical Window

The interfacial reactions in ASSLBs are often associated with the electrochemical windows of SSEs. The influence of the poor electrochemical windows on the high energy density (high-voltage cathode materials and lithium anode) of ASSLBs is directly limited. For the electrochemical stability of sulfide-based SSEs, there are different experimental and theoretical results. The first-principles calculation based on density functional theory (DFT) is performed to evaluate the electrochemical window.^[16a,17,76] As shown in Figure 2a, the stable electrochemical window of oxide-based SSEs shows a lot of variation. Most oxides have an oxidation voltage over 3 V vs. Li/Li⁺, while NASICON-type LATP and LAGP reach 4.2 V, and the LLZO shows the lowest reduction voltage of 0.05 V. The LLTO will be oxidized to O₂, La₂Ti₂O₇ and TiO₂ above 3.71 V, and reduced to La₂Ti₂O₇, Li_{7/6}Ti_{11/6}O₄ and Li₄Ti₅O₁₂ below 1.752 V. The titanium valence has a similar change beyond the stable voltage range in LATP. Most halide-based SSEs show a moderate theoretical electrochemical window. But the electrochemical window of most sulfide-based SSEs is narrow. The oxidation decomposition voltage of all sulfide is about 2.0–2.5 V, and the reduction decomposition voltage is about 1.7 V.

Although the theoretical calculation accurately predicts the electrochemical window of inorganic SSEs, it shows different results in actual experiment. Apart from the DFT, cyclic voltammetry (CV) and linear cyclic voltammetry (LSV) are a widely used method to investigate the electrochemical window of SSEs,^[16a,29,77] applying a linear polarization on the Li/SSEs/inert blocking electrode (i.e., stainless steel). Based on such CV measurement, there is a wide measured electrochemical window (>5 V) of sulfide-based SSEs.^[77c,78] The CV curve (Figure 2b, black line, stainless steel as working electrode) shows that in the voltage range of -0.5–5.0 V, except for the reduction and oxidation currents corresponding to Li depositing (Li⁺+e⁻→Li) and Li stripping (Li→Li⁺+e⁻) near 0 V, there is no current peak appears corresponding to electrolyte decomposition. This CV measurement (with inert blocking electrode) include Li depositing/stripping peaks near 0 V, whose current is larger than the electrolyte decomposition current, which makes the latter difficult to distinguish in the range of -0.5–5.0 V. But most of the electrochemical window calculated by the DFT is narrower, compared with experimental results. The above results are not enough to truly indicate the electrochemical stability of SSEs. In order to better reflect the thermodynamic properties of SSEs, Zeier et al.^[79] mixed a large amount of conductive agent in the sulfide-based SSEs (the mass ratio of sulfide and C is 90:10) to prepare a composite electrode. That allows the SSEs to be in full contact with the conductive agent and prevents the kinetic barrier from hindering the electrolyte decomposition reaction. As illustrated in Figure 2b, the cell leads to higher currents (orange), this design can significantly increase the active area of the charge transfer reaction, promote electron transport, and reflect the practical electrochemical stability of electrolyte. However, the measured electrochemical window of SSEs by modified CV still deviates from the theoretical calculation. With the continuous improvement of the experimental detection measurements and the substantial supplement of theoretical results, it has been widely recognized that the measured electrochemical window is the sum of the intrinsic electrochemical windows of SSEs and interphases. The thermodynamic calculation results prove that a wide voltage window detected by some experiments is triggered by dynamic factors, not inherent thermodynamic stability factors in sulfide.^[76] In terms of kinetics, the decomposition reaction is sluggish, which leads to a higher overpotential. If the reaction time is long enough under a certain voltage, the decomposition reaction will proceed spontaneously. And the electric insulating decomposition products can form a passivation layer on the electrolyte surface, which prevent electrolyte from further decomposing. Such a passivation layer in ASSLBs has the same effect as solid electrolyte interface (SEI) layer that commonly observed in liquid batteries. In addition, due to the electric insulating passivation layer, the chemical potential difference between the electrode materials and the sulfide-based SSEs becomes smaller, which is equivalent to reduce the voltage window by artificial regulation. So that is why the experimental results ostensibly show a wider electrochemical window of sulfide-based SSEs.

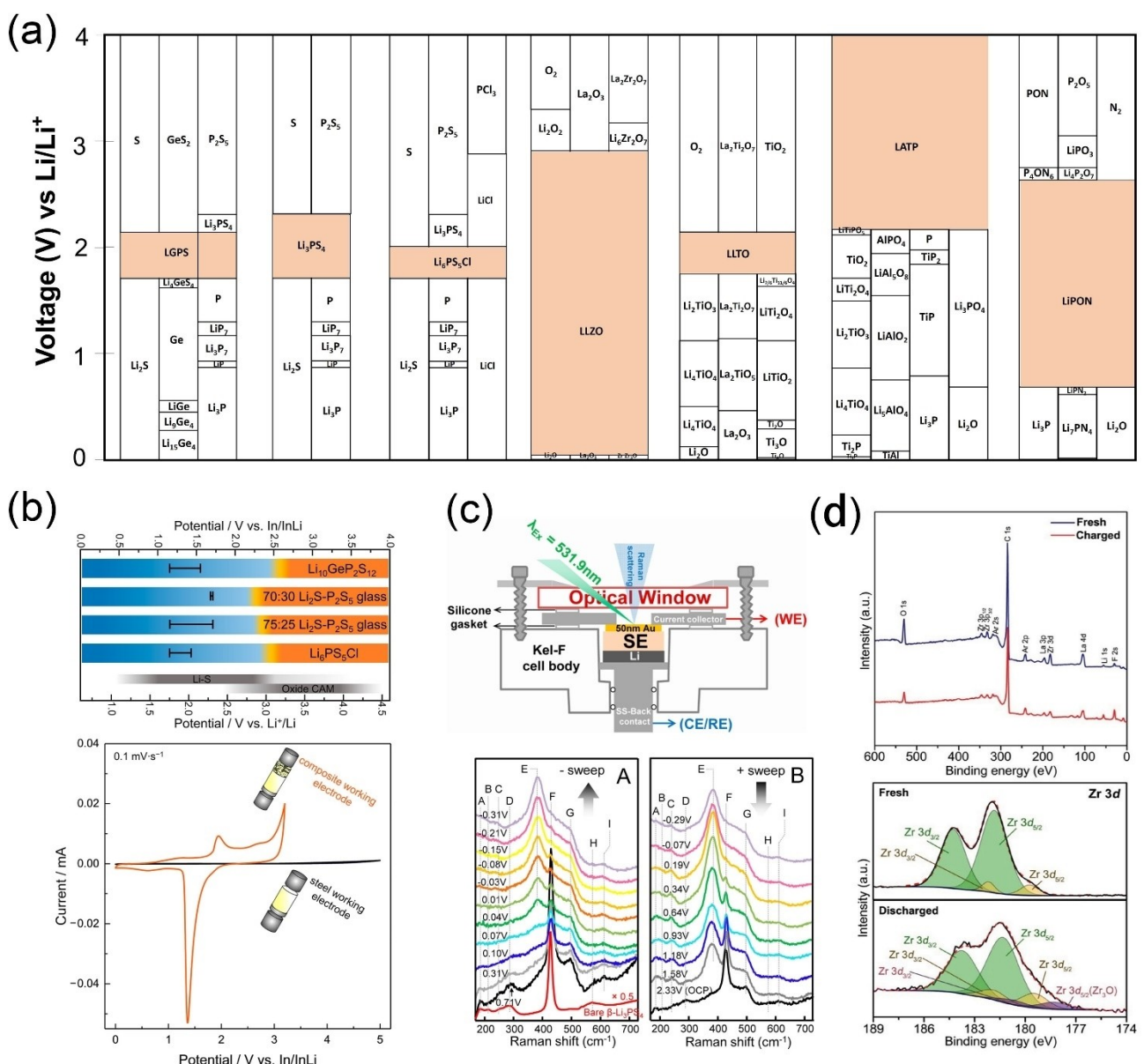


Figure 2. a) The first principles calculation results of the voltage profile and phase equilibria of some representative inorganic SSEs upon lithiation and delithiation. b) Practical oxidative stability limit of LGPS, Li₂S·P₂S₅ glasses and Li₆PS₅Cl against a carbon composite working electrode (indium metal counter electrode). Visual comparison of two types of electrode morphology in CV experiments with the thiophosphate solid electrolyte LGPS. By employing In/InLi as both reference/counter electrode and planar stainless steel as working electrode, only small currents are detected (black). Adding a carbon-solid electrolyte composite electrode to the cell (orange) leads to higher currents, and significant oxidative decomposition reactions are visible.^[79] (b) Reproduced with permission from Ref. [79]. copyright 2019, American Chemical Society. c) Spectro-electrochemistry cell designed for operando Raman spectroscopic measurement at solid electrolyte and thin film metal electrode interface. Operando Raman spectra at β-Li₃PS₄ solid electrolyte and 50 nm Au interface during negative and positive potential sweeps.^[80] Reproduced with permission from Ref. [80], copyright 2017, American Chemical Society. d) The XPS spectra of the fresh and charged LLZO. The atomic percentage of O and Zr in the sample is obtained from the area of O 1s and Zr 3d peak, respectively. High resolution Zr 3d core XPS spectra of fresh and discharged LLZO.^[82] Reproduced with permission from Ref. [82], copyright 2016, Wiley-VCH.

Sang et al.^[80] used the in-situ Raman spectroscopy of Li/SSEs/Au cell to investigate the potential-dependent decomposition of β-Li₃PS₄ and LGPS, the experimental equipment and the Raman spectra are shown in Figure 2c. At β-Li₃PS₄/Au interface, the PS₄³⁻ units (peak F) degrade during negative potential sweep and the P₂S₆⁴⁻ units (peak E) appear with the Li₂S. Then P₂S₆⁴⁻ can change back to PS₄³⁻ during positive potential sweep. Wagemaker et al.^[81] used the X-ray diffraction (XRD) measurements to observe the lithiated argyrodite

Li₆PS₅Cl phases during cycling. A growing peak at around 27° reflects the formation of the Li₂S, which provides a direct evidence of the predicted decomposition reaction (Li₁PS₅Cl→P+5Li₂S+LiCl). Using SSEs+C/stainless steel cells, the LSV results revealed the oxidative stability limit of 2.45 V for (LiBH₄)₂·AB and 2.04 V for LiBH₄·AB.^[74b]

The XPS (Figure 2d) was used to identify the reduction and oxidation products of LLZO beyond its stability window.^[82] The atomic ratio of O to Zr decreases from 7.6:1 to 4.9:1 after LLZO

was charged to 4.5 V. This result confirms that LLZO releases O₂ during charging. The increase in the relative intensity of the side peak at 179.7 eV and the appearance of a new peak at a lower binding energy (178.2 eV, ascribed to Zr₃O herein) confirmed the reduction of Zr in LLZO during discharging. The main peak at 181.8 eV of Zr still remained after discharging to 0 V, indicating that the surface of LLZO was reduced. The results demonstrated that the electrochemical window of garnet is not as wide as reported, and the reduction of Zr and the oxidation of O in LLZO occur beyond the stability window of LLZO.

As investigated by theoretical calculations, the electrochemical window of the halide-based SSEs is related to the composition.^[83] In theory, the fluoride-base solid SSEs has a wider electrochemical window than other halide SSEs, even over 6 V vs. Li/Li⁺.^[16a] Nevertheless, the ionic conductivity of the fluoride-base SSEs is too low to meet practical applications. To date, no reported fluoride-based SSEs with acceptable RT ionic conductivity have been reported. The chloride-base SSEs also has a wide electrochemical window with oxidation potentials over 4 V vs. Li/Li⁺. The upper limit of the stability window of Li₃YCl₆ and Li₃YBr₆ evaluated by Tetsuya Asano et al. was found to be about 4.5 V vs. Li/Li⁺ using a cell configuration of SUS/SSE/LPS/Li. Comparatively, bromides and iodides exhibit narrower stability windows.^[84] The anti-perovskite solid electrolyte Li₃OX appears to have a wider electrochemical window compared with the halide-base SSEs. Through experimental and theoretical calculations,^[68,85] Li₃OCl is predicted to have an electrochemical window over 5 V. This indicates that Li-rich anti-perovskite has good electrochemical stability.

3.2. Interfaces within SSEs and Single-Material ASSLBs

3.2.1. Interfaces within SSEs

The oxide-based SSEs are usually prepared by solid phase method and sol-gel method. Once the temperature is too high during sintering, LLZO will produce abnormal grain growth,^[86] as shown in Figure 3a. Li loss at high temperatures become common practice in the solid-state process of LLZO.^[87] And the

larger grain diameter is several hundred microns. The grain boundaries are very loose, so the mechanical strength of the electrolyte is very low. The crystal grains are uniform as shown in Figure 3b by controlling the temperature or using atmosphere sintering.^[88] The grain size is about 1 μm and the density is very high. In general, decrease of grain size and increase of bulk density lead to higher ionic conductivity of materials.^[89] However, the grain resistance and grain boundary resistance together determine the conductive characteristics of the electrolyte. The diffusion rate of lithium ions at the LLZO grain boundary is 1/2–1/3 of the bulk diffusion rate. So, the size of the grain boundary resistance determines the overall ionic conductivity of the electrolyte compared to the grain resistance. As the grain size decreases, the ionic conductivity of LLZO shows a trend of first increase and then decrease. When there are few grain boundaries, the increase of the interfacial area causes the impurities to segregate to the grain boundaries while the degree of impurity segregation in the grains decreases. Therefore, the obstacles set up by impurities in the lithium ion diffusion path in the crystal grains are reduced which also increases the ionic conductivity of LLZO. On the other hand, the diffusion of lithium ions in the grain boundaries is more difficult if there are more grain boundaries in LLZO, so the increase of grain boundaries decreases the ionic conductivity of LLZO.^[90] Moreover, LLZO pellets with less grain boundaries, larger grain size and higher relative density are more stable in air.^[91] It also suggests that grain boundaries are more sensitive to air than grains, which is consistent with the other observation.^[92] It was initially thought that the higher mechanical strength of solid electrolytes could prevent lithium dendrites and short circuits. However, a short-circuit phenomenon appeared after cycling for 5 hours in the Li/Li_{6.6}La₂Zr_{1.6}Ta_{0.4}O₁₂(LLZTO)/Li cell.^[93] This is because lithium dendrites grow along the grain boundaries during the cycle,^[94] as shown in Figure 3c. LLTO has a higher bulk ionic conductivity, but its grain boundary conductivity is lower than 10⁻⁵ S cm⁻¹. So the problem of grain boundary resistance larger than the propagation of grains^[95] (Figure 3d) and lithium dendrites can grow through LLTO defects (which can be macro defects such as voids, cracks, etc., or micro defects such as grain boundaries, non-stoichiometric defects, etc.).^[96] Anti-

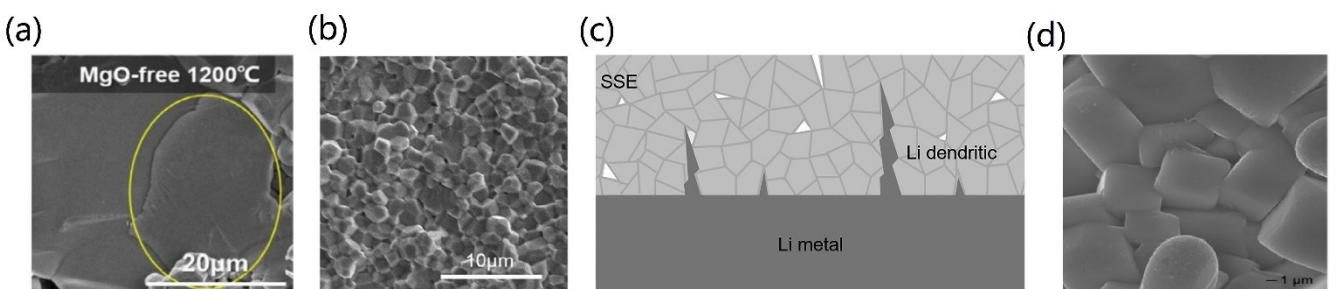


Figure 3. a) Cross-sectional microstructures of Ta-LLZO ceramic bars sintered at 1200 °C for 5 h on the Pt support.^[86] Reproduced with permission from Ref. [86], copyright 2019, Elsevier. b) Cross-sectional SEM images of the Ga-LLZO pellets prepared using 1150 °C × 1 min 950 °C × 3 h.^[88] Reproduced with permission from Ref. [88], copyright 2019, Elsevier. c) Schematic illustration of the growth of lithium dendrites at the voids and grain boundaries of SSEs.^[94] copyright 2018, Elsevier. d) FESEM images of LLTO + 1 wt.% Li₂O–B₂O₃ composite electrolytes sintered at 1250 °C.^[95] Reproduced with permission from Ref. [95], copyright 2017, Elsevier.

perovskite Li_3OX can be synthesized at a lower temperature and has a lower melting point than other SSEs. This lower melting point can reduce grain boundaries during synthesis.^[14b] Grain boundaries can severely hinder the conduction of ions in the electrolyte, which has a great effect on the ionic conductivity.^[97]

3.2.2. Single-Material ASSLBs

Wang's group^[98] proposed the concept of using the single-material ASSLBs with LGPS, which acts as both anode and cathode after mixing with carbon additives. The schematic diagram and scanning electron microscope (SEM) of the single-LGPS battery are depicted in Figure 4a. The XPS and CV measurements indicated that the Li–S and Ge–S components can act as cathode and anode, respectively, which come from the reduction and oxidation of LGPS. Composing the battery in this way is beneficial to the interface in closer contact, and the

interfacial reaction between the electrode and the electrolyte is alleviated. And the transition region at the interface becomes smoother in chemical composition and potential variance. The same battery structure can also be found in other sulfide-based SSEs. The ASSLBs using the Li_3PS_4 glass, $80\text{Li}_2\text{S}\cdot20\text{P}_2\text{S}_5$ glass, $78\text{Li}_2\text{S}\cdot22\text{P}_2\text{S}_5$ glass-ceramic and $\text{Li}_6\text{PS}_5\text{Cl}$ as an active material were successfully charged and then discharged.^[99] Zhang et al.^[99c] used $78\text{Li}_2\text{S}\cdot22\text{P}_2\text{S}_5$ glass-ceramic as both the cathode material and the solid electrolyte to investigate the reaction inside electrodes. The XRD (Figure 4b) showed the $78\text{Li}_2\text{S}\cdot22\text{P}_2\text{S}_5$ glass-ceramic generated the Li_2S crystal phase during the discharge process. Similar oxidation and reduction behaviors are also found in the argyrodite SSEs as the active material.^[81,99d,100] To induce the oxidation and reduction of SSEs, Wagemaker et al.^[81] mixed carbon black and carbon nanofibers into $\text{Li}_6\text{PS}_5\text{Cl}$. Complementary to the other measurements, solid-state ^{31}P magic angle spinning (MAS) NMR measurements were performed to investigate the decomposition products formed during cycling. And they proposed the indirect

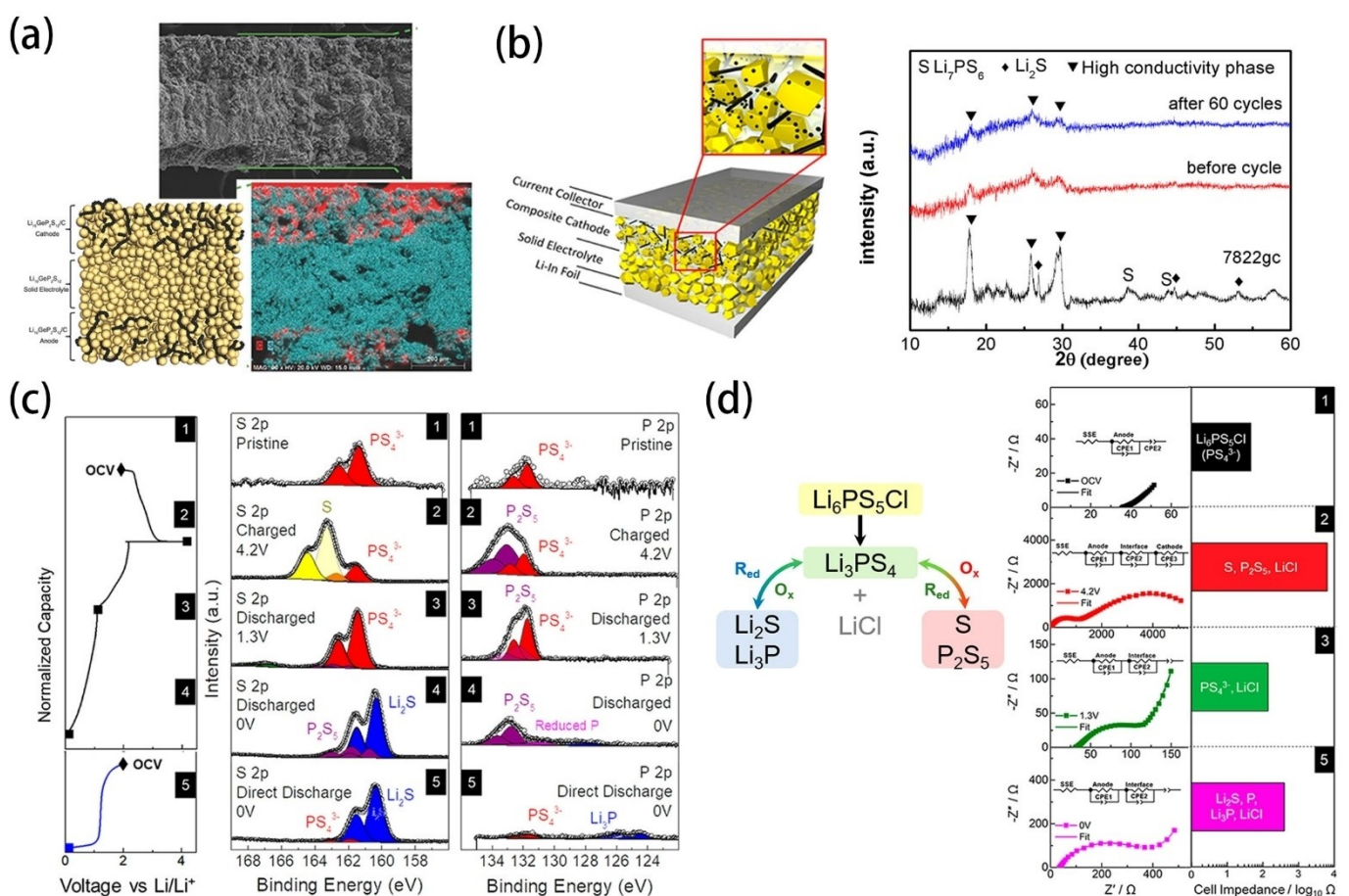


Figure 4. a) Schematic diagram of a single-LGPS ASSLBs. Cross-section SEM images of the single-LGPS battery and elemental mappings of C (red) and S (blue).^[98] Reproduced with permission from Ref. [98], copyright 2015, Wiley-VCH. b) Schematic configuration of the monolithic $78\text{Li}_2\text{S}\cdot22\text{P}_2\text{S}_5/78\text{Li}_2\text{S}\cdot22\text{P}_2\text{S}_5$ /Li–In cell. The XRD pattern of the $78\text{Li}_2\text{S}\cdot22\text{P}_2\text{S}_5$ (7822gc) electrolyte material and the composite cathodes before and after 60 cycles.^[99c] Reproduced with permission from Ref. [99c], copyright 2018, American Chemical Society. c) The deconvoluted S 2p and P 2p XPS spectra XPS spectra showing the binding energies of $\text{Li}_6\text{PS}_5\text{Cl}$ at different cycling potentials. The cycling voltage profile at 0.25 mA cm^{-2} for reference. d) Redox reaction pathway of $\text{Li}_6\text{PS}_5\text{Cl}$. Nyquist plots at different cycling potentials showing the impedance changes of the Li–In/ $\text{Li}_6\text{PS}_5\text{Cl}/\text{Li}_6\text{PS}_5\text{Cl}$ –C half-cell (left). The bar graph shows relative differences in battery impedance at different oxidation or reduction states of $\text{Li}_6\text{PS}_5\text{Cl}$ –C (right).^[99d] (c) and (d) are reproduced with permission from Ref. [99d], copyright 2019, American Chemical Society.

oxidation and reduction decomposition mechanisms of $\text{Li}_6\text{PS}_5\text{Cl}$ solid electrolyte (unstable $\text{Li}_4\text{PS}_5\text{Cl}$ (S/S^{2-} redox) and unstable $\text{Li}_{11}\text{PS}_5\text{Cl}$ (P/P^{5+} redox). Meng et al.^[99d] combined various methods to characterize the products and intermediate products of $\text{Li}-\text{In}/\text{Li}_6\text{PS}_5\text{Cl}/\text{Li}_6\text{PS}_5\text{Cl}+\text{C}$ half-cell under different charge and discharge states. The XRD was conducted for the $\text{Li}_6\text{PS}_5\text{Cl}-\text{C}$ cathode at corresponding cycling potentials, which amorphous oxidized S and P_2S_5 and nanocrystalline Li_2S products begin to form during cycling. As the XPS spectra (Figure 4c) shown, when charged to 4.2 V, the pristine $\text{Li}_6\text{PS}_5\text{Cl}$ (contained PS_4^{3-}) was decomposed into S and P_2S_5 products. When discharged to 1.3 V, the S and P_2S_5 peaks weakened, and the PS_4^{3-} unit reappeared, but Li_2S had not yet formed at this time. When it was further discharged to 0 V, the Li_2S signal gradually appeared, and weak signals of phosphorus compounds and Li_3P were detected, as well as unreacted residual P_2S_5 . By comparing the impedance changes (Figure 4d) of $\text{Li}-\text{In}/\text{Li}_6\text{PS}_5\text{Cl}/\text{Li}_6\text{PS}_5\text{Cl}+\text{C}$ cell at different voltages, it showed that the impedance increase during cycling is mostly attributed to the oxidative decomposition of $\text{Li}_6\text{PS}_5\text{Cl}$ (cathode side) under high voltage. In contrast, the reductive decomposition contribution (anode side) is relatively small, which may be related to the formation of Li_3P . The above results demonstrate the reversibility of the electrochemical decomposition reaction of some sulfide-based SSEs (e.g. $\text{Li}_6\text{PS}_5\text{Cl}$). When P is reduced at a lower voltage, the S and P_2S_5 will undergo a process of forming an intermediate redox product PS_4^{3-} before finally forming Li_2S .

3.3. SSEs/Cathode Interfaces

In addition to the decomposition reaction of the sulfide-based SSEs in ASSLBs, the interfacial reaction between the inorganic

SSEs and cathode materials is also an important factor limiting the battery capacity, as summarized in Table 2. In most cases, the working voltage of the cathode material is not very wide, so interfacial reactions often occur in ASSLBs. The formation of interphases is generally driven by chemical and electrochemical processes simultaneously. The chemically driven interphase requires no external voltage, regarded as a static process. The electrochemical process accelerates degradation of the interphase with lithium depositing and stripping.

Richards et al.^[16a] theoretically calculated the reaction energy to predict the stability between the sulfides and oxide cathode materials. Sulfide-based SSEs are unstable (have a large reaction energy) when paired with many layered oxide cathode materials (e.g. LiCoO_2 (LCO)), due to high voltage and oxygen chemical potential. The strong reaction between PS_4 groups of sulfides and cathode oxides can form PO_4 groups and metal sulfides. In contrast, the oxide-based SSEs are relatively stable. Sumita et al.^[101] validated the instability at LiFePO_4 (LFP)/ Li_3PS_4 interface with the hybrid theoretical calculations. As Contour maps (Figure 5a) of layered density of states (LDOSs) shown, the valence band top (VBM) of Li_3PS_4 is slightly higher than that of LFP. The redox reaction at LFP/ Li_3PS_4 interface is a probable phenomenon and the S–S bond also has been predicted found after the Li_3PS_4 oxidation by the FePO_4 phase. Many experimental tests have also confirmed the theoretically calculated interfacial reactions. Using cross-sectional high-angle annular dark field (HAADF) scanning TEM (STEM) with energy dispersive X-ray spectroscopy (EDX), in Figure 5b, the Co, P, and S elements mutually diffused near the $80\text{Li}_2\text{S}\cdot20\text{P}_2\text{S}_5/\text{LCO}$ interface, which means that the side reactions occurred.^[102] By scanning Auger microscopy (SAM) and XPS analysis, Auvergniot et al.^[103] found that sulfur-containing species (S, Li_2S_n , and P_2S_x) and LiCl generate at the interface

Table 2. Interfacial reactions between cathodes and inorganic SSEs.

Inorganic SSEs	Cathode	Reaction products	Method	Ref.
Li_3PS_4	LiCoO_2	$\text{S}, \text{CoS}_2, \text{Co}(\text{PO}_3)_2$	DFT	[16a]
Li_3PS_4	LiFePO_4	$\text{P}_2\text{S}_7, \text{S}$	DFT	[16a]
Li_3PS_4	LiMnO_2	$\text{S}, \text{Mn}_2\text{S}_3, \text{Mn}_2\text{P}_2\text{O}_7$	DFT	[16a]
$80\text{Li}_2\text{S}\cdot20\text{P}_2\text{S}_5$	LiCoO_2	CoS_2 (The reaction product layer continuously consumes the Co ion in LiCoO_2)	XANES	[207]
$75\text{Li}_2\text{S}\cdot25\text{P}_2\text{S}_5$	FePS_3	$\text{Li}_{1.5}\text{FePS}_3, \text{P}_2\text{S}_6^{4-}$ unit	XRD + XANES + Raman + DFT	[208]
$\text{Li}_{10}\text{GeP}_2\text{S}_{12}$	LiFePO_4	$\text{P}_2\text{S}_7, \text{S}, \text{GeS}_2$	DFT	[16a]
$\text{Li}_{10}\text{GeP}_2\text{S}_{12}$	LiMnO_2	$\text{GeS}_2, \text{S}, \text{Mn}_2\text{P}_2\text{O}_7, \text{Mn}_2\text{S}_3$	DFT	[16a]
$\text{Li}_{10}\text{GeP}_2\text{S}_{12}$	LiCoO_2	$\text{S}, \text{CoS}_x, \text{P}_2\text{S}_6^{2-}$ unit, $\text{SO}_4^{2-}, \text{SO}_3^{2-}, \text{GeS}_x$ and/or GeO_2	XANES + XPS	[104]
Li_4SnS_4	LiCoO_2	SnS_2, S	DFT	[16a]
$\text{Li}_6\text{PS}_5\text{Cl}$	LiCoO_2	$\text{CoCl}, \text{S}, \text{CoP}_4\text{O}_{11}, \text{CoS}_2$	DFT	[16a]
$\text{Li}_6\text{PS}_5\text{Cl}$	LiFePO_4	$\text{S}, \text{LiCl}, \text{P}_2\text{S}_7$	DFT	[16a]
$\text{Li}_6\text{PS}_5\text{Cl}$	LiMnO_2	$\text{Mn}_2\text{PClO}_4, \text{S}$	DFT	[16a]
$\text{Li}_6\text{PS}_5\text{Cl}$	LiCoO_2	$\text{S}, \text{Li}_2\text{S}, \text{Li}_2\text{S}_n, \text{P}_2\text{S}_x, \text{LiCl}, \text{SO}_3^{2-}$	XPS + SAM	[103]
$\text{Li}_6\text{PS}_5\text{Cl}$	$\text{LiNi}_{0.8}\text{Co}_{0.1}\text{Mn}_{0.1}\text{O}_2$	$\text{S}, \text{Li}_2\text{S}_n, \text{P}_2\text{S}_x, \text{LiCl}, \text{SO}_3^{2-}$	XPS	[105a]
LLZO	LiCoO_2	$\text{O}_2, \text{La}_2\text{O}_3, \text{La}_2\text{Zr}_2\text{O}_7$	DFT	[16a]
LLZO	LiFePO_4	$\text{Li}_3\text{PO}_4, \text{LaPO}_4, \text{Fe}_2\text{O}_3, \text{La}_2\text{Zr}_2\text{O}_7$	DFT	[16a]
LLZO	LiMnO_2	$\text{La}_2\text{O}_3, \text{Li}_2\text{MnO}_3, \text{La}_2\text{Zr}_2\text{O}_7$	DFT	[16a]
LLZO	LiCoO_2	La_2CoO_4	TEM	[110]
LLZO	LiMn2O_4	Lithiated manganese-deficient oxides, $\text{La}_x\text{Zr}_y\text{O}_z$ compounds, LaMn_2O_5	XPS	[113]
LAGP	LiFePO_4	$\text{AlPO}_4, \text{LiGe}_2(\text{PO}_4)_3$	XPS	[209]
LAGP	LiCoPO_4	$\text{Co}_2\text{P}_2\text{O}_7, \text{GeO}_2$	XRD	[210]
LiPON	LiCoO_2	Li_2O or $\text{Li}_2\text{O}_2, \text{CoO}, \text{Co}_3\text{O}_4$	STEM + EELS	[115]
$\text{Li}_{3.2}\text{PO}_{3.8}\text{N}_{0.2}$	LiFePO_4	$\text{Li}_3\text{PO}_4, \text{N}_2, \text{Li}_4\text{P}_2\text{O}_7$	DFT	[16a]
$\text{Li}_{3.2}\text{PO}_{3.8}\text{N}_{0.2}$	LiCoO_2	$\text{LiCoPO}_4, \text{LiNO}_3, \text{Li}_4\text{P}_2\text{O}_7$	DFT	[16a]
$\text{Li}_{3.2}\text{PO}_{3.8}\text{N}_{0.2}$	LiFePO_4	$\text{Li}_3\text{PO}_4, \text{N}_2, \text{Li}_4\text{P}_2\text{O}_7$	DFT	[16a]

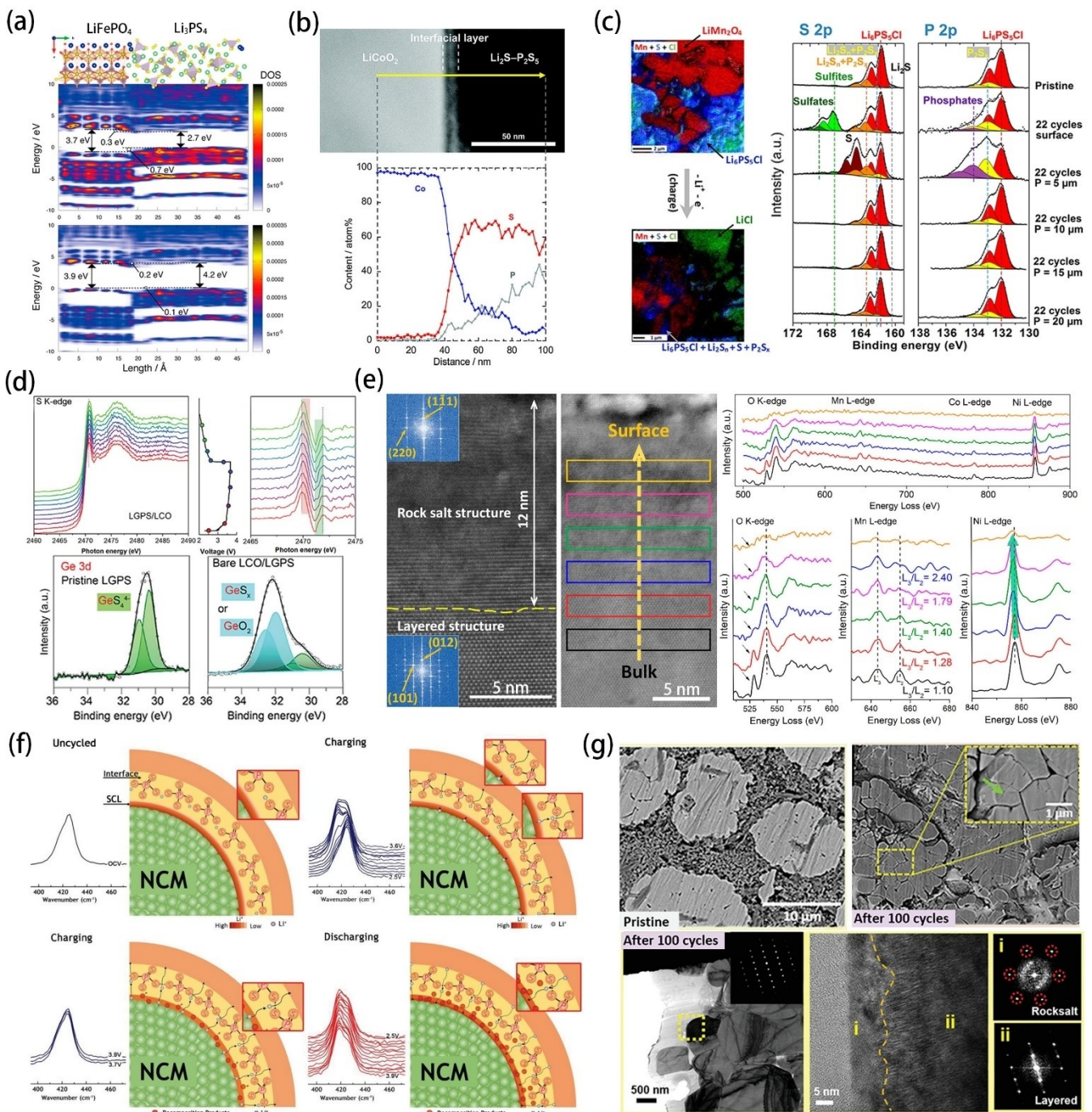


Figure 5. a) Contour maps of LDOSs for beta electrons in the system of $\text{Li}_3\text{PS}_4/\text{LiFePO}_4$ systems along the b axis. Fermi level of each system is set to zero. Upper LDOSs are calculated on the structures at the + U level. Bottom ones are calculated at the HSE06 hybrid functional level on the same equilibrium structures obtained at the + U level.^[101] Reproduced with permission from Ref. [101], copyright 2017, American Chemical Society. b) Cross-sectional HAADF-STEM image of $\text{LiCoO}_2/80\text{Li}_2\text{S}\cdot20\text{P}_2\text{S}_5$ interface after initial charging and cross-sectional EDX line profiles for Co, P, and S elements.^[102] Reproduced with permission from Ref. [102], copyright 2010, American Chemical Society. c) The SAM mappings of Mn, S, and Cl elements from a cross section of the composite LMO electrode of the LMO/ $\text{Li}_6\text{PS}_5\text{Cl}/\text{Li}-\text{In}$ half-cell before cycling and after 22 cycles (bar = 2 μm). S 2p and P 2p XPS spectra of the composite LMO electrode of LMO/ $\text{Li}_6\text{PS}_5\text{Cl}/\text{Li}-\text{In}$ half-cells: before cycling (pristine), after 22 cycles, and after 22 cycles with increasing etching depths of the electrode from 5 to 20 μm .^[103] Reproduced with permission from Ref. [103], copyright 2017, American Chemical Society. d) In-situ XANES of ASSLBs during the initial charge-discharge process. (S K - edge of the bare LCO/LGPS cathode) And the Ge 3d XPS spectra on the pristine LGPS, LCO/LGPS electrodes after 100 cycles.^[104] Reproduced with permission from Ref. [104], copyright 2019, Wiley-VCH. e) Microstructure evolution of NMC811 cathodes after cycling in SSLBs identified by STEM-HAADF images and corresponding EELS spectra. Atomic-level STEM-HAADF image of a bare NMC811 cathode after cycling with corresponding FFT patterns and corresponding EELS spectra acquired from the regions.^[106] Reproduced with permission from Ref. [106], copyright 2019, American Chemical Society. f) Schematic illustrations of interface evolutions during the charge-discharge processes based on different vibration states of P-S bond in PS_4^{3-} at NCM/ $\text{Li}_6\text{PS}_5\text{Cl}$ interface.^[105a] Reproduced with permission from Ref. [105a], copyright 2019, Wiley-VCH. g) Cross-sectional SEM images of NCA80 electrodes before cycling and after 100 cycles. Ex-situ TEM images for surface of the secondary particle for NCA80 and their corresponding SAED patterns.^[105c] Reproduced with permission from Ref. [105c], copyright 2019, Wiley-VCH.

between $\text{Li}_6\text{PS}_5\text{Cl}$ and oxide cathode such as LCO, $\text{LiNi}_{1/3}\text{Co}_{1/3}\text{Mn}_{1/3}\text{O}_2$ (NMC111) and LiMn_2O_4 (LMO). The SAM images and XPS results (Figure 5c) showed us the spatial separation about LiCl and sulfur-containing particles LMO/ $\text{Li}_6\text{PS}_5\text{Cl}$. To unveil the interfacial reactions between LCO and LGPS, Wang et al.^[104] performed in-situ sulfur K-edge X-ray absorption near edge spectroscopy (XANES) (Figure 5d). It presents a lot of shoulder peaks at 2470 eV (red bar) and 2472 eV (green bar) during the charge-discharge process, which is a sign of interfacial reaction. The ex-situ XPS spectra of Ge 3d demonstrated that GeS_x or GeO_2 is reduced LCO/LGPS after 100 cycles. The Ni-rich layered $\text{LiNi}_{0.8}\text{Mn}_{0.1}\text{Co}_{0.1}\text{O}_2$ (NMC811) is the most commercially available oxide cathode material. Some characterizations have investigated the reaction mechanism of the $\text{Li}(\text{Ni}_x\text{Mn}_y\text{Co}_z)\text{O}_2$ (NMC) NMC/SSEs interface.^[105] The HAADF-STEM with electron energy loss spectroscopy (EELS) (Figure 5e) was carried out to investigate the interface evolution between NMC811 and LGPS during the charge-discharge process. Confirmed by the fast Fourier transformation (FFT), the atomic-level structural TEM images present obvious differences in the lattice patterns between the LGPS and bulk region after cycling.^[106] The lattice pattern at inner region is still the layered structure phase, but it can be indexed as the rock-salt phase at interface. The O K-edge, Mn and Ni L-edge EELS spectra indicate that the significant reduction of transition metals, Mn in the rock-salt region, and Ni in the interface region, respectively. In Figure 5f, the in-situ Raman spectroscopy measurements to monitor the detailed interface evolutions in NMC811/ $\text{Li}_6\text{PS}_5\text{Cl}/\text{Li}$ cell. While the interface reaction occurs, the Li^+ migration can also cause a slight change of PS_4^{3-} structure at interface.^[105a] In addition to these interface evolutions, interfacial reactions also cause the chemo-mechanical failure at interface.^[105c,107] Koerver et al.^[107a] demonstrated the contact loss caused by chemo-mechanical contraction between NMC811 and $\beta\text{-Li}_3\text{PS}_4$ after charging, which further increases the interfacial resistance and capacity loss. By Ar-ion beam milling using a cooling cross-sectional polisher at -90°C , the $\text{Li}(\text{Ni}_{0.80}\text{Co}_{0.16}\text{Al}_{0.04})\text{O}_2$ (NCA80)/ $\text{Li}_6\text{PS}_5\text{Cl}$ interface is clearly observed in cross-sectional SEM and TEM images^[105c] (Figure 5g). For NCA80 particles, the intergranular cracks and void spaces cause the randomly oriented and ionically loosened/isolated secondary particles at the initial cycle. After 100 cycles, the volume changes bring severe particle disintegration. Apart from that, the similar volume change was also observed in Li-S ASSLBs with S/C mixture, leading to contact loss and irreversible Li_2S formation.^[107b]

The oxide-based SSEs have a high elastic modulus, resulting in a small contact area between SSEs and cathodes.^[108] In addition, the formation of the third phase in the interface region causes a certain structural stress during the charge-discharge process. The accumulated stress causes the interface to fracture and separate, eventually leading to the broken of the ASSLBs. Miara et al.^[109] used DFT calculations to study the thermodynamic stability of the interface formed between LLZO and cathode materials. The calculation results are shown in Figure 6a. The most thermodynamically stable interface can be formed between LLZO and LCO. But the LMO and LFP cathodes can react violently with LLZO. However, Kim et al.^[110] deposit

the LCO electrode layer on LLZO by pulsed laser deposition at 937 K for 1 h. TEM images found that a 50 nm thick interface layer was formed at the interface (Figure 6b). Elements such as Co, La, and Zr diffused along the interface and formed La_2CoO_4 at high temperatures, which would increase the charge transfer resistance and hinder the transfer rate of lithium ions at interface. This shows that even the most stable LCO and LLZO interfaces do not fit well. In addition, Goodenough et al.^[111] found that the atoms at the LLZO-LCO interface diffuse at high temperatures (Figure 6c), which causes the LLZO in the interface region to change from a cubic phase to a tetragonal phase. Ceder et al.^[112] found that LLZTO reacted with the $\text{Li}_2\text{NiMn}_3\text{O}_8$, $\text{Li}_2\text{FeMn}_3\text{O}_8$, and LiCoMnO_4 at 600°C to form new phases at high temperatures. The presence of these new phases increases the interfacial impedance of the composite anode in ASSLBs. XPS provided evidence of a limited interfacial reaction between LMO and LLZO.^[113] LiFePO_4 reacts severely with LATP at low temperature ($T < 500^\circ\text{C}$) and produces NASICON $\text{Li}_3\text{M}_2(\text{PO}_4)_3$ ($\text{M} = \text{Fe}$ and others).^[114]

In summary, there are two main sources of interface resistance between the oxide-based SSEs and the cathode materials. One is the reaction between the electrolyte and the cathode material to generate an interface phase. Second, atomic diffusion occurs at the interface to form an interface phase.

Compared with other inorganic solid electrolytes, halide-based SSEs seem to have good interfacial stability towards oxide cathode materials. Recently, the interfacial stability of Li_3YCl_6 and Li_3YBr_6 solid electrolytes with LCO cathode has been predicted by first-principles calculations.^[83] The ASSLBs assembled with Li_3YCl_6 and Li_3YBr_6 as electrolytes and LCO as cathode have also been reported to have good performance.^[62] In addition, Li_3InCl_6 is also stable to oxide cathode materials without any interface treatment.^[14b] As shown in Figure 6d, no obvious change of Li_3InCl_6 was observed on the XPS spectra upon mixing with LCO, confirming the excellent chemical stability of Li_3InCl_6 with LCO. Furthermore, no significant change was observed on the In L₃-edge and Cl K-edge XANES spectra for LCO– Li_3InCl_6 cathode composites at different charge/discharge state. This further confirms that Li_3InCl_6 has excellent electrochemical stability after contacting with LCO.

Wang et al.^[115] used in-situ STEM-EELS technology to reveal the LiPON/LCO interface in thin-film ASSLBs (Figure 6e). There is a disordered and unstable interfacial layer, which accumulates lithium and evolves to rock-salt CoO after cycling. Meanwhile, they believe that the interfacial reaction is main reason about increasing interface resistance and capacity loss, not the effect of space charge layer (SCL).

3.4. SSEs/Anode Interfaces

The interfacial reactions between anodes and inorganic SSEs are summarized in Table 3. Lithium metal is an ideal anode material because of its low electrode potential (-3.04 V vs. NHE) and high specific capacity (3862 mAh g^{-1}).^[116] If the conventional LIBs directly use lithium metal as anode material,

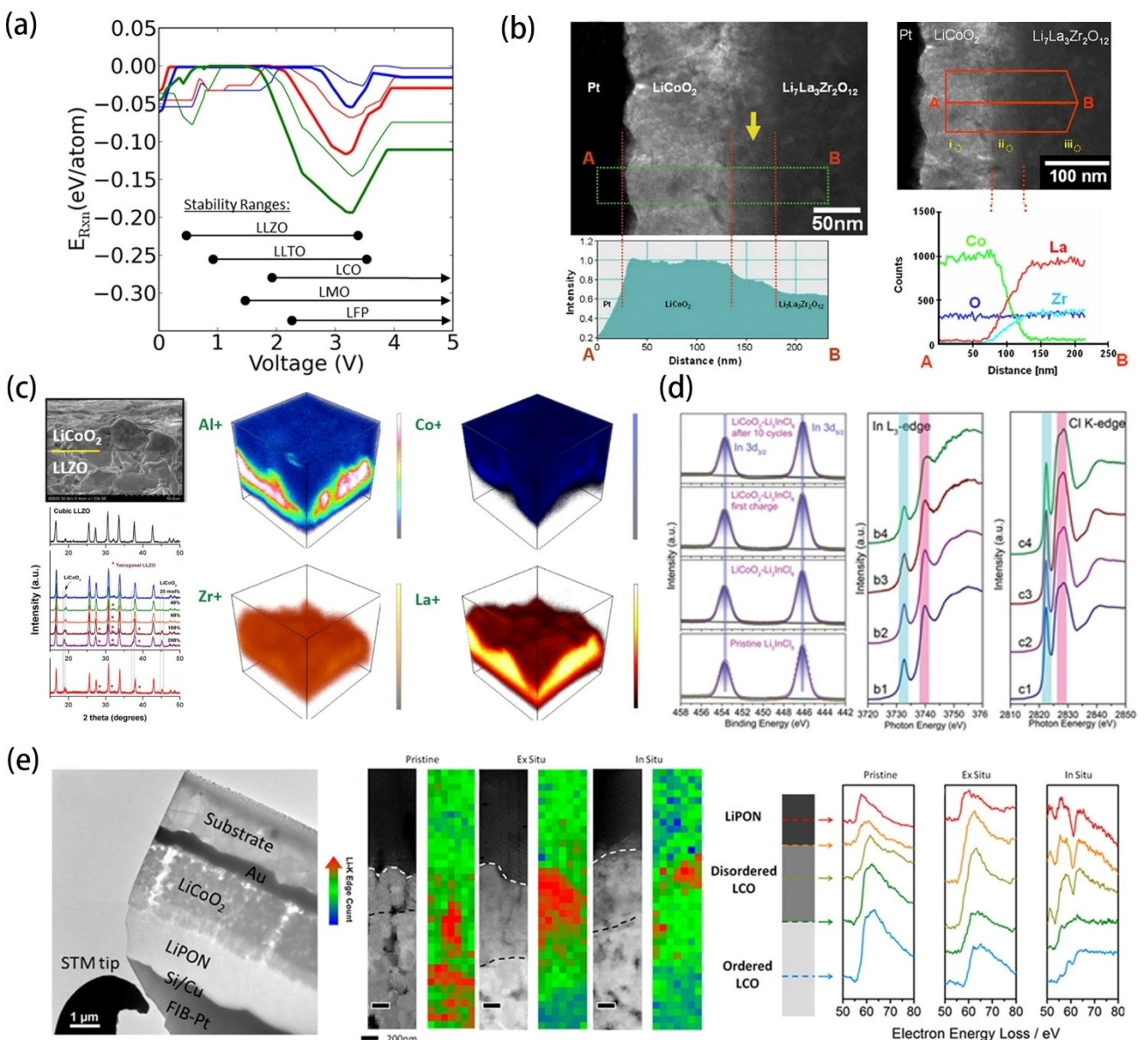


Figure 6. a) Driving force for interphase formation between electrolyte, and cathode, with varying voltage from 0 to 5 V vs lithium. (Legend: blue = LCO; red = LMO; green = LFP; thick line = LLZP; thin line = LLTO.) The calculated intrinsic stability windows are marked along the bottom for reference.^[109] Reproduced with permission from Ref. [109], copyright 2015, American Chemical Society. b) Cross-sectional TEM image, intensity profile EDS, line profile of the LLZO/LCO thin film.^[110] Reproduced with permission from Ref. [110], copyright 2010, Elsevier. c) XRD patterns of pristine LLZO powder, thermally formed LCO on LLZO by a solid state reaction method at 700 °C for 6 h with ratios of 20–200 mol % LCO to LLZO, and powder mixture of LCO and LLZO (1:4 wt%) annealed at 700 °C for 1 h. TOF-SIMS-enabled three-dimensional elemental maps of the LCO/LLZO interface that is displayed in the inset SEM image.^[111] Reproduced with permission from Ref. [111], copyright 2016, American Chemical Society. d) XPS spectra of the pristine annealed-Li₃InCl₆, LCO-Li₃InCl₆ cathode composites, LCO-Li₃InCl₆ cathode after the first charge, and LCO-Li₃InCl₆ cathode after 10 cycles. In L-edge and Cl K-edge XANES spectra of (b1, c1) pristine annealed-Li₃InCl₆, (b2, c2) LCO-Li₃InCl₆ cathode composite, and LCO-Li₃InCl₆ cathode composites collected (b3, c3) after the first charge and (b4, c4) after the first discharge.^[14b] Reproduced with permission from Ref. [14b], copyright 2019, Royal Society of Chemistry. e) TEM bright field image of STM tip connecting a nanobattery. HAADF-STEM images with EELS of the nanobattery stack along with Li K-edge concentration mapping and spectra of pristine, ex-situ and in-situ samples.^[115] Reproduced with permission from Ref. [115], copyright 2016, American Chemical Society.

it will react with LEs to generate a SEI during cycling. At the same time, lithium dendrites will generate due to the uneven distribution of current density. However, the SSEs are solid lithium ion conductors with excellent mechanical property, which can effectively avoid the occurrence of short circuit and improve the safety of ASSLBs. Nevertheless, due to the strong reducibility of lithium metal, some high-valence metal cations can be easily reduced to form an interface layer with high

resistance, resulting in poor chemical stability.^[29] The interface between lithium metal and SSEs can be classified into three types, which is schematically shown in Figure 7a:^[16c] (1) Non-reactive and thermodynamically stable interface. SSEs do not react with lithium metal, which can form a sharp two-dimensional interface; (2) Reactive and mixed conducting interface (MCI). The interface has both electronic and ionic conductivity, and may continue to grow towards the electrolyte side, thereby

Table 3. Interfacial reactions between anodes and inorganic SSEs.

Inorganic SSEs	Anode	Reaction products	Method	Ref.
Li_3PS_4	Lithium	Li_2S Or S, $\text{Li}_4\text{P}_2\text{S}_6$	DFT	[16a, 211]
Li_3PS_4	Lithium	Li_2S , Li_3P	XPS	[212]
Li_3PS_4	Acetylene Carbon	S, P_2S_5 Or S, $\text{Li}_4\text{P}_2\text{S}_6$	XPS + XANES	[123]
77.5Li ₂ S·22.5P ₂ S ₅	Lithium	Li_2S , Li_3P , Li_2O	XPS	[123]
$\text{Li}_3\text{P}_2\text{S}_{11}$	Lithium	Li_2S , Li_3P	XPS	[16c]
$\text{Li}_{10}\text{GeP}_2\text{S}_{12}$	Lithium	Li_2S , Li_3P , $\text{Ge}_4\text{Li}_{15}$ Or Li_2S , Li_3P , Ge	XPS	[119a, 119b]
$\text{Li}_6\text{PS}_5\text{X}$ ($\text{X} = \text{Cl}, \text{Br}, \text{I}$)	Lithium	Li_2S , Li_3P , LiX	XPS	[119c]
$\text{Li}_6\text{PS}_5\text{Cl}$	Lithium	S, Li_2S , Li_2S_n , P_2S_x , LiCl , SO_3^{2-}	XPS	[105a]
LLZO	Lithium	LiOH , Li_2CO_3	XRD	[124]
LATP	Lithium	LiF Or AlF_3	XPS	[127]
LATP	Lithium	$\text{Li}_{0.3}\text{Al}_{1.7}(\text{PO}_4)_3$	XRD	[129]
LATP	Lithium	Li_2O , Li_3P , Li_5AlO_4	XRD	[213]
LAGP	Lithium	Li–Ge alloy, AlPO_4	XPS	[214]
LiPON	Lithium	Li_3PO_4 , Li_3P , Li_3N , Li_2O	XPS	[215]

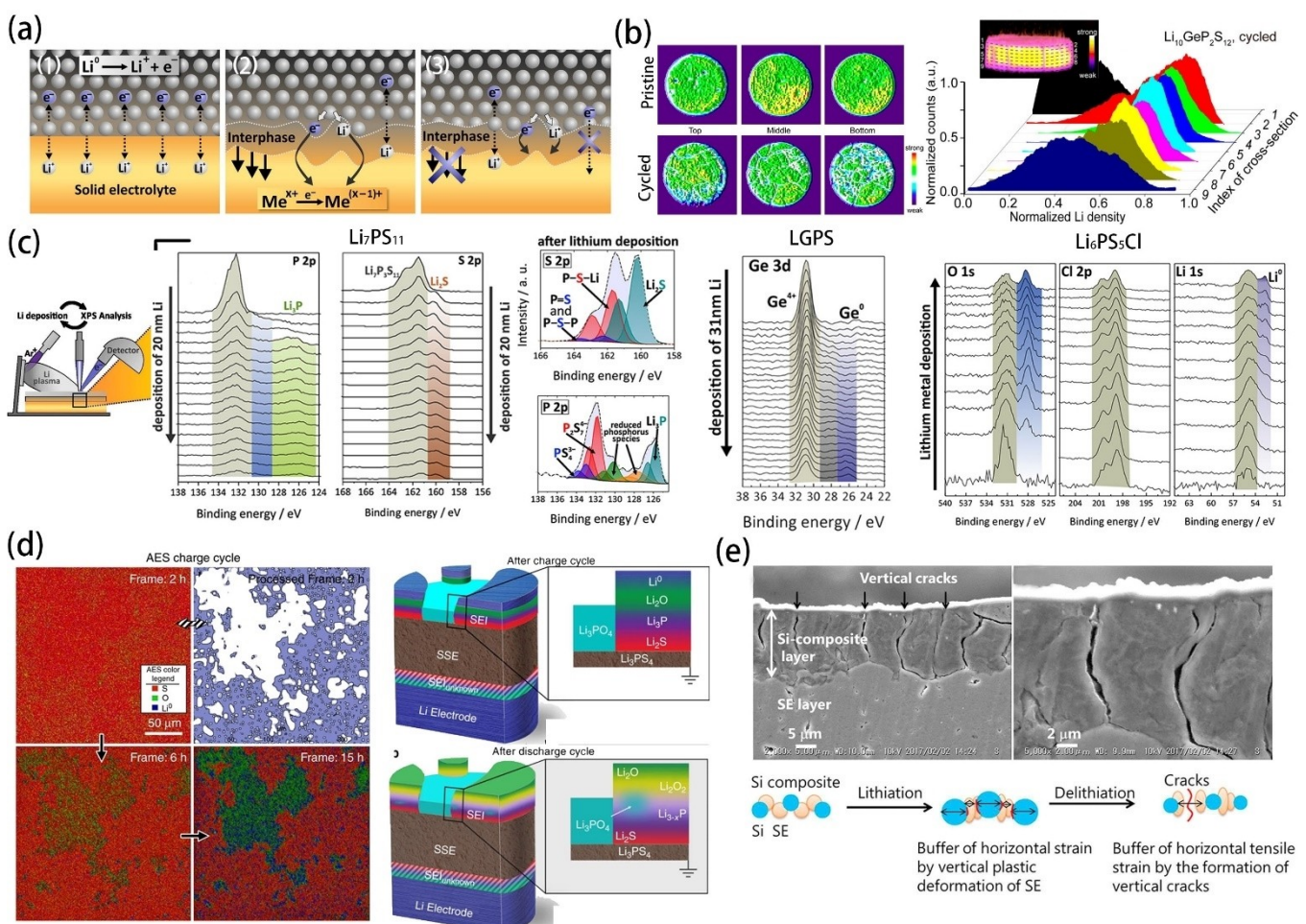


Figure 7. a) Types of interfaces between lithium and a solid lithium ion conductor. Non-reactive and thermodynamically stable interface; reactive and MCI; reactive and metastable SEI.^[16c] Reproduced with permission from Ref. [16c], copyright 2015, Elsevier. b) 2D cross sections taken from 3D ${}^7\text{Li}$ MRI images of pristine and cycled LGPS electrolytes in a symmetric Li/LGPS/Li cell. Lithium density profile at different depths of electrochemically cycled LGPS pellets.^[118] Reproduced with permission from Ref. [118], copyright 2018, American Chemical Society. c) Experimental setup of the in-situ XPS experiment to monitor the reaction between sulfide and lithium. The S 2p, P 2p, O 1s, Ge 3d and Cl 2p XPS spectra of $\text{Li}_3\text{PS}_{11}$, LGPS and $\text{Li}_6\text{PS}_5\text{Cl}$ samples as a function of increasing amount of lithium metal being deposited.^[119] Reproduced with permission. Copyright 2015, Elsevier. Copyright 2016, American Chemical Society. Copyright 2017, Elsevier. d) In-situ AES mapping of Li_3PS_4 SEI heterogeneity after 2 h, 6 h and 15 h of charging and summary of SEI composition and morphology.^[123] Reproduced with permission from Ref. [123], copyright 2011, The Authors. e) Cross-sectional SEM image and corresponding magnified image of bulk-type Si composite anode pelletized on Li_3PS_4 SE layer. Schematic diagram of half-cell during charge and discharge. (The blue and orange regions represent Si and SE, respectively.)^[132] Reproduced with permission from Ref. [132], copyright 2018, Elsevier.

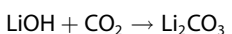
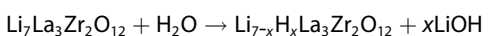
changing the overall properties of material and causing severe self-discharge. Since many SSEs contain multivalent cations, it is easy to form MCI when contacting with lithium metal. Thermodynamically driven MCI formation can only be avoided by introducing a protective film (artificial SEI film); (3) Reactive and metastable SEI. The interface has electronic insulating and ionic conductivity. If the electronic conductivity is low enough, the interface is thin enough. Moreover, the SEI is stable during cycling, and its ionic conductivity determines the battery performance.

The theoretical calculation results^[17,76,82] show that LGPS begins to be lithiated and reduced at 1.7 V, which is consistent with the cyclic voltammetry curves. The phase equilibrium components of LGPS at 0 V consist of Li₃P, Li₂S and Li₁₅G₄, which are also observed in experiments. The above reduction products by lithium have a favorable reaction energy, -1.25 eV atom⁻¹ (-3014 kJ mol⁻¹). Other sulfide-based SSEs, such as Li_{3.25}Ge_{0.25}P_{0.75}S₄, Li₃PS₄, Li₄GeS₄, Li₆PS₅Cl and Li₇PS₈I are also reduced at similar potentials (about 1.6–1.7 V). At 0 V, their phase equilibrium components correspond to the lithiation reaction products, which is favorable thermodynamically.

Shin et al.^[117] have comparatively studied the performance of TiS₂/Li–In ASSLBs employing Li₃PS₄ and LGPS. Although the ionic conductivity of LGPS is higher than Li₃PS₄, the CV and XRD results suggested that LGPS is unstable below 1 V, and the interfacial impedance will increase significantly during cycling, resulting in capacity fading. Li–In/Li₃PS₄ interface is more stable, but its capacity fade faster at high-rate because of lower ionic conductivity. In Li₂S–P₂S₅ binary SSEs system, Li₃PS₄ has the most stable structure, which brings the relatively stable interphase with lithium. A good cyclic performance is attributed to the formation of thin and stable SEI. Employing the three-dimensional ⁷Li magnetic resonance imaging (MRI) and the derived histograms, Chien et al.^[118] revealed Li depletion and deficiency at Li/LGPS interfaces within symmetric Li/LGPS/Li cell after electrochemical cycling (Figure 7b). With the top showing 40% Li deficiency and 20% for the bottom, Li deficiency at interface is the major cause for continuous increase in the interfacial resistance. And it also has tremendous impact on Li microstructure formation and associated safety issues. Using a self-developed in-situ XPS method, Wenzel et al.^[119] have studied the interfacial stability of Li₇P₃S₁₁, LGPS and Li₆PS₅Cl against lithium (Figure 7c). All are unstable in contact with lithium and the increased interfacial resistance can be observed on EIS results. Meanwhile, the interfacial reaction can be clearly observed by XPS and the interfacial decomposition products consist of Li₂S and Li₃P. For LGPS, the Li–Ge alloy and Ge metal also have been found at interface, which can increase electronic conductivity. Because of Li–Ge alloy and Ge metal, the interfaces of Li₇P₃S₁₁ and LGPS against lithium have different properties. Li₇P₃S₁₁ can form a stable SEI, which of the thickness and interfacial resistance become stable after a certain time and no longer increase over time. Compared with Li₇P₃S₁₁, the interphase has a higher growth rate between LGPS and lithium, which cannot bring a stable interface. So, the presence of cations in SSEs such as Ge, Sn, Ti is detrimental to the formation of stable SEI. Sakuma et al.^[120] found that in

Li_{4-x}Ge_{1-x}P_xS₄ SSEs, the more Ge content was, the greater the interfacial reaction became. When Li–M (M=Sn, Si) alloy anode was adopted, the higher redox potential of alloy was, the lower interfacial resistance was. The interfacial reaction also causes the chemo-mechanical failure, accompanied by lithium dendrite. A real-time Neutron depth profiling (NDP) also was measured to determine the dynamic evolution of the lithium concentration profiles in Li/Li₃PS₄/Pt cell during Li plating. The increased peaks in surface region indicates the continuous Li plating on the anode, which is an evidence that lithium dendrite nucleates and grows directly inside Li₃PS₄.^[121] A bevel-shaped cross-section SEM at Li/Li₃PS₄ interface showed the presence of lithium and void-filled structure after cycling confirmed the existence of crack-expansion.^[122] Wood et al.^[123] illustrated the most likely structure of SEI at Li/Li₃PS₄ after both charging and discharging. Combined with real-time in-situ auger electron spectroscopy (AES) (Figure 7d), the oxygen-containing components exhibit that Li₃PO₄ initially forms directly on the Li₃PS₄ and can inhibit lithium ion migration.

The interface between the oxide-based SSEs and lithium can be divided into two types. One is electrochemically stable with lithium, which typical representative is LLZO. The interfacial reaction between LLZO and lithium is mainly due to Li₂CO₃ and LiOH impurities formed at interface (Figure 8a). The reaction equation is as follows:



The products LiOH and Li₂CO₃ are both poor Li⁺ conductors, which can hinder the transmission of Li⁺ at interface.^[124]

The other type is unstable with lithium, which can form a MCI. The high electronic conductivity will further encourage the side reaction between SSEs (LAGP, LLTO and LATP) and lithium, while promoting the rapid growth of Li dendrites^[125] and the in-situ deposition^[126] of lithium metal in SSEs. When LAGP ceramics are in direct contact with lithium, the reaction area is limited due to point contact. Lithium will continuously react with LAGP due to MCI. The degree of reaction also increases with increasing contact time. The reacted particles of LAGP will turn black and swell after reaction (Figure 8b). The enlarged particles inside the LAGP can cause the ceramic to crack.^[127] The LLTO also contains Ti⁴⁺, which will be reduced to Ti³⁺ by lithium,^[128] as shown in the Figure 8c. Cheng et al.^[129] found that the contact of LATP with lithium will observe the formation of Li₃Al_{0.3}Ti_{1.7}(PO₄)₃. This illustrates the insertion of lithium ions and the reduction of Ti⁴⁺. It will be observed that the diffraction pattern of LATP particles gradually weakens as the reduction reaction progresses until it finally disappears (Figure 8d). This shows that LATP eventually becomes amorphous.

As so far, the researches about the interfaces between lithium and halide-based SSEs or anti-perovskite SSEs are still scarce. But it is worth pointing out that the interface of Li₃OCl solid electrolyte with lithium metal has self-stability during

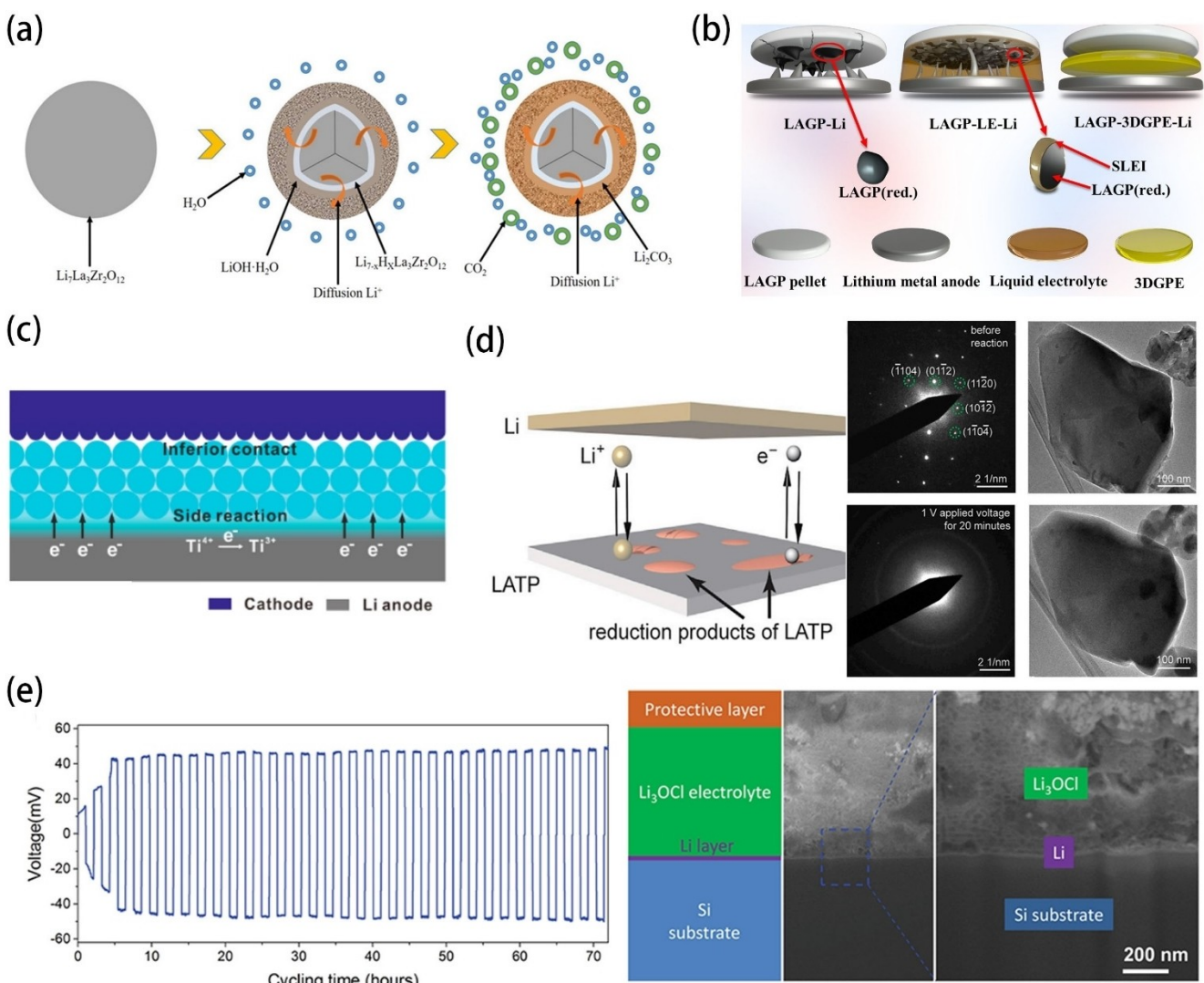


Figure 8. a) A schematic model illustrating the LCO formation process on the surface of lithium garnets.^[124] Reproduced with permission from Ref. [124], copyright 2017, American Ceramic Society. b) Schematic diagram illustrating the interactions between different electrolyte systems and lithium anodes. LAGP pellet directly contacted with the lithium anode; LE was added at the interface between the LAGP pellet and lithium anode; LAGP pellet was separated from the lithium anode by 3D gel polymer electrolyte (3DGPE).^[127] Reproduced with permission from Ref. [127], copyright 2019, American Chemical Society. c) A schematic illustration of the battery with pristine LATP.^[128] Reproduced with permission from Ref. [128], copyright 2019, American Chemical Society. d) The scenario at LATP/Li interface composed of the reduction products of LATP. The diffraction pattern and the bright-field images of bare LATP particles before and after a 20 min reaction. (LATP particles reacted with lithium under a potential of 1 V.)^[129] Reproduced with permission from Ref. [129], copyright 2019, Elsevier. e) The cyclability of the Li/Li₃OCl/Li symmetric cell at a constant current of 1.0 mA. A schematic illustration of the multilayer structure, the overall cross-sectional SEM image and the magnified SEM image of local interfacial structure.^[85] Reproduced with permission from Ref. [85], copyright 2016, The Authors.

cycling has been reported.^[66,85] Figure 8e shows the voltage profile of the Li/Li₃OCl/Li symmetric cell. The voltage gradually increases in the first few cycles and then remain essentially unchanged. It can be seen from SEM images that the interface contact between Li and Li₃OCl is relatively smooth. These evidences show that Li₃OCl solid electrolyte has good compatibility with lithium.^[85]

Apart from metallic lithium anode, other anode materials such as Li₄Ti₅O₁₂ (LTO),^[41,130] graphite and Si,^[131] have also been utilized in ASSLBs. The interfacial reactions also occur between SSEs and these anodes materials. During cycling, the lattice parameters of LTO hardly change and the crystal structure can maintain a high degree of stability. Compared with other oxide

active materials, the interfacial reactions between LTO and sulfide-based SSEs have similar decomposition products. Considering the large volume change of Si anode, the crack generation originated from volume change is the most problematic interface issue, not interfacial reaction in ASSLBs with Si anode.^[132]

4. Approaches to Stabilize Interfaces of Inorganic SSEs

For practical applications presently, although electrochemical windows of sulfide-based SSEs are narrow and air stabilities are poor, the favorable mechanical properties enable the sulfide-based SSEs to be used with roll-to-roll industrial fabrication. There's a lot of potential for large-scale applications in the near future. Regarding costs, the Li₂S and metal sulfides are expensive. The Li₂S can be synthesized using cheap LiH and S powders.^[35b] Some works also focus on cheap and earth-abundant Sn or Si substitution for Ge in LGPS.^[78c,133] For oxide-based SSEs, LLZO has some advantages such as high ionic conductivity, good chemical and electrochemical stability with lithium metal, and good air stability, etc. However, LLZO needs to be sintered at a high temperature of 1200 °C for a long time to reach densification via conventional method, and at the same time, there will be serious "Li-loss" and abnormal grain growth phenomenon. Expensive equipment and low productivity enable LLZO not easy to achieve large-scale preparation and industrialization. Wang et.al proposed a none-mother-powder method to achieve the small grain size, tight grain boundary, dense microstructure and high conductivity. This rapid sintering method can greatly shorten the sintering time, and even the sintering can be completed in only 10 minutes.^[134] Therefore, there is still a long way to go for the commercialization of ASSLBs.

The compatibility issues between electrode and SSEs also plague the large-scale practical application of SSEs in ASSLBs. To be more specific, the cathode/SSE interface is suffering from undesirable element diffusion and side reactions due to the narrow electrochemical window of SSEs,^[16a] the interface instability result in increasing interfacial impedance and deteriorating battery performance. For the lithium/SE interface, since the strong reductive lithium, almost all the typically SSEs (such as Li₂P₃S₁₁,^[16a] Li₃PS₄,^[135] argyrodite^[105a]) are suffering from chemically unstable issues after contact with lithium metal, thus giving rise to the growth of Li dendrites along the SSEs, and the resulting decomposition products have low ionic conductivity and high electronic conductivity.^[136] To alleviate these serious interface problems of SSEs, many efforts have been carried out.

4.1. Modification of Electrolyte Composition

4.1.1. Doping

Doping in the SSEs system has been studied a lot so far to improve ionic conductivity of SSEs, which reduces the interfacial resistance and expands working potential window.^[40,137] As the mobile ions in the ionic conductor govern the ion diffusion and the occupancy of lithium ion, doping aliovalent cations (such as P⁵⁺, Si⁴⁺, Sn⁴⁺, Sb⁵⁺...) or anions (such as O²⁻, Se²⁻, halogen elements Cl⁻, Br⁻, I⁻...) into the crystal structure is applicable to increasing the ionic

conductivity.^[138] As early as in 2002, Li_{4-x}Si_xP₂S₄ with high ionic conductivity, negligible electronic conductivity and high electrochemical stability was created by partially substituted of P in the typical Li₂S-P₂S₅ binary by Si.^[139] Afterwards, Ge, Sn or Sb cation were also certified to be a positive effect on ionic conductivity and electrochemical performance.^[30,39,41,140] Consequently, Ge-substituted SSE usually exhibited the highest ionic conductivities (Figure 9a) since the impact of its large radius on the Li sublattice. Moreover, O was incorporated into the well-studied Li₁₀MP₂S₁₂ (M=Si, Ge, Sn) SSEs system, the obtained Li₁₀(MS₄)(PO₄)₂ oxy sulfide SEs exhibit higher lithium ion diffusion and wider electrochemical stability window (Figure 9b).^[141] Besides, with the addition of moisture-resistant O element, higher moisture stability was founded in the Li₁₀GeP₂S₄O₈. Such air-stable capacity could also be realized by Sn substitution of P in argyrodite SSEs since strong Sn-S bonding energy than P-S.^[38] Similar to the O doped strategy, Wu et al.^[142] reported a Se doped Li₂S-P₂S₅ SSE with higher ionic conductivity and electrochemical stability. Meanwhile, for the halogen contained Li₆PS₅Br, halogen element Cl could also be doped in the Br site to obtain high conductive SSEs due to the optimal distribution of the halogen dopants over the crystal lattice.^[143] Furthermore, cation and anion dual-doping was proved to be a more effective strategy to realize dual-effect. The superionic conductor Li₇P_{2.9}Mn_{0.1}S_{10.7}I_{0.3} with exceptionally high ionic conductivity of 5.6 mS cm⁻¹ and a wide stable electrochemical window up to 5 V vs. Li/Li⁺ was synthesized via Mn and I co-doping.^[137d] And ZnO co-doping was adopted to optimize Li₆PS₅Br SSE since the ability of Zn to inhibit the growth of lithium dendrite and the compatibility of O with oxide cathode (Figure 9c).^[40] The symmetric cell with Li_{6.7}Zn_{0.15}PS_{4.85}O_{0.15}Br electrolyte could sustain a current density over 0.78 mA cm⁻² for 140 cycles, which was ascribed to the formed LiZn and Li₃OB₃ in the Li₆PS₅Br/Li interface.

LLZO has cubic and tetragonal phases, but the ionic conductivity of the former is 1 to 2 orders of magnitude higher than that of the latter. Researchers use elemental doping to increase ionic conductivity and stabilize the crystal structure. Lincoln et al.^[109] used density functional theory to calculate all possible elements that can be incorporated into LLZO. The results are shown in Figure 9d. Most common elements in the periodic table can be incorporated into LLZO, and most of them have been confirmed by experimental results. LLZO has Li-site doping, La-site doping and Zr-site doping. Dermenci et al.^[144] stabilized the cubic phase structure by replacing Li in LLZO with Al. Al-Li_{1-x}Zr₂O₁₂ was prepared by solid-phase method using Li₂CO₃, La₂O₃, ZrO₂, and Al₂O₃ as raw materials. Finally, it was found that 30 mol% Al containing samples sintered at 1150 °C for 12 h showed tightly connected grains and stable cubic phase structure. In Deviannapoorni et al.'s work,^[145] an investigation has been carried out on the microstructure, lithium ion conduction behavior and structural stability of Li₇La_{3-x}Y_xZr₂O₁₂ (x=0.125, 0.25 and 0.50) prepared by conventional solid-state reaction technique. Among the garnets, Li₇La_{2.75}Y_{0.25}Zr₂O₁₂ sintered at 1200 °C exhibits a maximized total (bulk+grain boundary) ionic conductivity of 3.21 × 10⁻⁴ Scm⁻¹ at RT along with improved relative density of 96%.

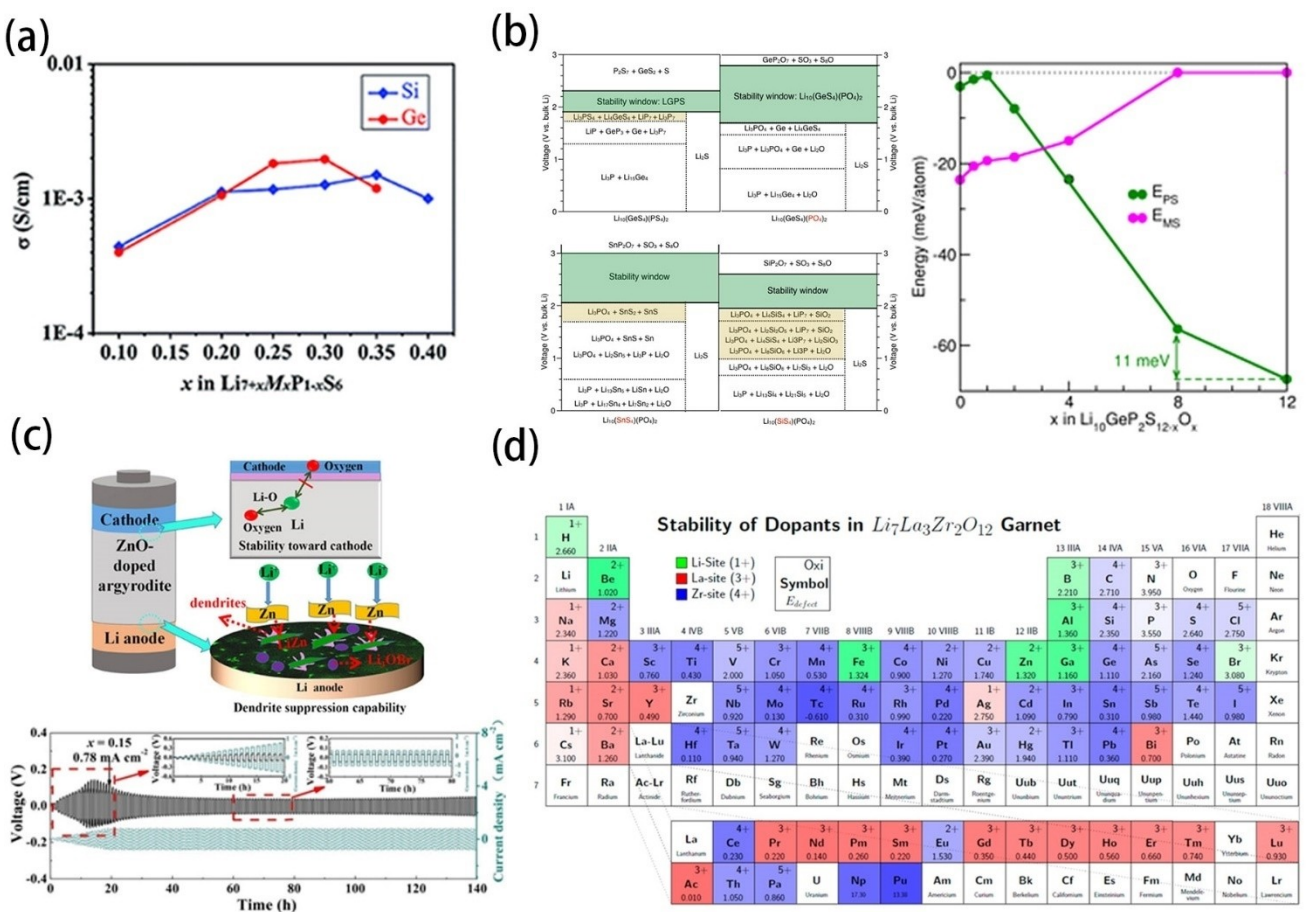


Figure 9. a) Ionic conductivities at RT of pressed $\text{Li}_{7+x}\text{M}_x\text{P}_{1-x}\text{S}_6$ ($\text{M}=\text{Si, Ge}$).^[140b] Reproduced with permission from Ref. [140b], copyright 2019, Royal Society of Chemistry. b) Electrochemical stability windows of $\text{Li}_{10}\text{MP}_2\text{S}_4\text{O}_8$ ($\text{M}=\text{Si, Ge, Sn}$) oxysulfides and corresponding sulfide analogue LGPS as reference. Phase stability (E_{ps}) and moisture stability (E_{ms}) with a gradual increase in O content in LGPS.^[141] Reproduced with permission from Ref. [141], copyright 2019, American Chemical Society. c) Schematic diagram for the advantages of the ZnO-doped argyrodite $\text{Li}_6\text{PS}_5\text{Br}$; SEM image of the $\text{Li}/\text{Li}_{6.7}\text{Zn}_{0.15}\text{PS}_{4.85}\text{O}_{0.15}\text{Br}$ interface after cycling the symmetric cell. Galvanostatic intermittent cycling of the $\text{Li}/\text{Li}_{6.7}\text{Zn}_{0.15}\text{PS}_{4.85}\text{O}_{0.15}\text{Br}/\text{Li}$ symmetric cell at 0.78 mA cm^{-2} .^[40] Reproduced with permission from Ref. [40], copyright 2019, American Chemical Society. d) Site and oxidation state preference for the dopant elements studied. The color shows the most stable cation site (green for Li-site, red for La-site, and blue for Zr-site). The darker colors signify lower defect energy, such that Al^{3+} (Li) is darker than B^{3+} (Li). The box also shows the preferred oxidation state and the defect energy (in eV).^[109] Reproduced with permission from Ref. [109], copyright 2015, American Chemical Society.

Du et al.^[146] prepared Ta-LLZO with a conductivity of $1.6 \times 10^{-3} \text{ S cm}^{-1}$. The good battery performance can be attributed to the highly conducting ceramic electrolytes, the optimum electronic and ionic conducting networks in the composite cathodes.

Although LLTO has higher grain conductivity, it is difficult to control the final product composition during the synthesis process which result difficult to obtain higher conductivity. Researchers have improved the ionic conductivity of LLTO by doping two sites. Teranishi et al.^[147] studied the effect of partially substituted Nd on the conductivity of LLTO. The experimental results show that the grain conductivity of LLTO doped with 0.5% Nd has increased by 1.33 times. The increase in ionic conductivity may be caused by the increase of the disordered cubic phase. Le et al.^[148] added 1 wt.% Al and an excess of different proportions of Li_2O to the LLTO by the sol-gel method. The experimental results show that the sample has a tetragonal structure and no impurity phase.

4.1.2. Polymer-Inorganic Composite Electrolytes

Recently, polymer-sulfide composite solid electrolytes (CSEs) which combines the advantages of both have been made to achieve high flexible solid electrolytes. The polymer component could improve the mechanical properties of SSEs and suppress serious interfacial reaction.^[149] Firstly, one of the SSEs, LGPS, was incorporated into poly(ethylene oxide) (PEO) matrix.^[150] A flexible polymer-sulfide membrane (Figure 10a) with high ionic conductivity ($1.2 \times 10^{-3} \text{ S cm}^{-1}$) and a broad electrochemical window (5.7 V) was obtained. All-solid-state LFP/Li cell employing PEO-LGPS membrane demonstrated fascinating electrochemical performance. And the underlying chemistry mechanism of lithium ion conduction through hybrid LGPS-PEO interface was identified via solid-state NMR.^[151] In addition, not only with the well-known PEO polymer, but also poly(vinylidenefluoride-hexafluoro propylene) (PVDF-HFP) was also employed in LGPS.^[152] The XPS results revealed that an in-situ LiF -rich SEI layer was formed by infiltration of perfluoropolyethers

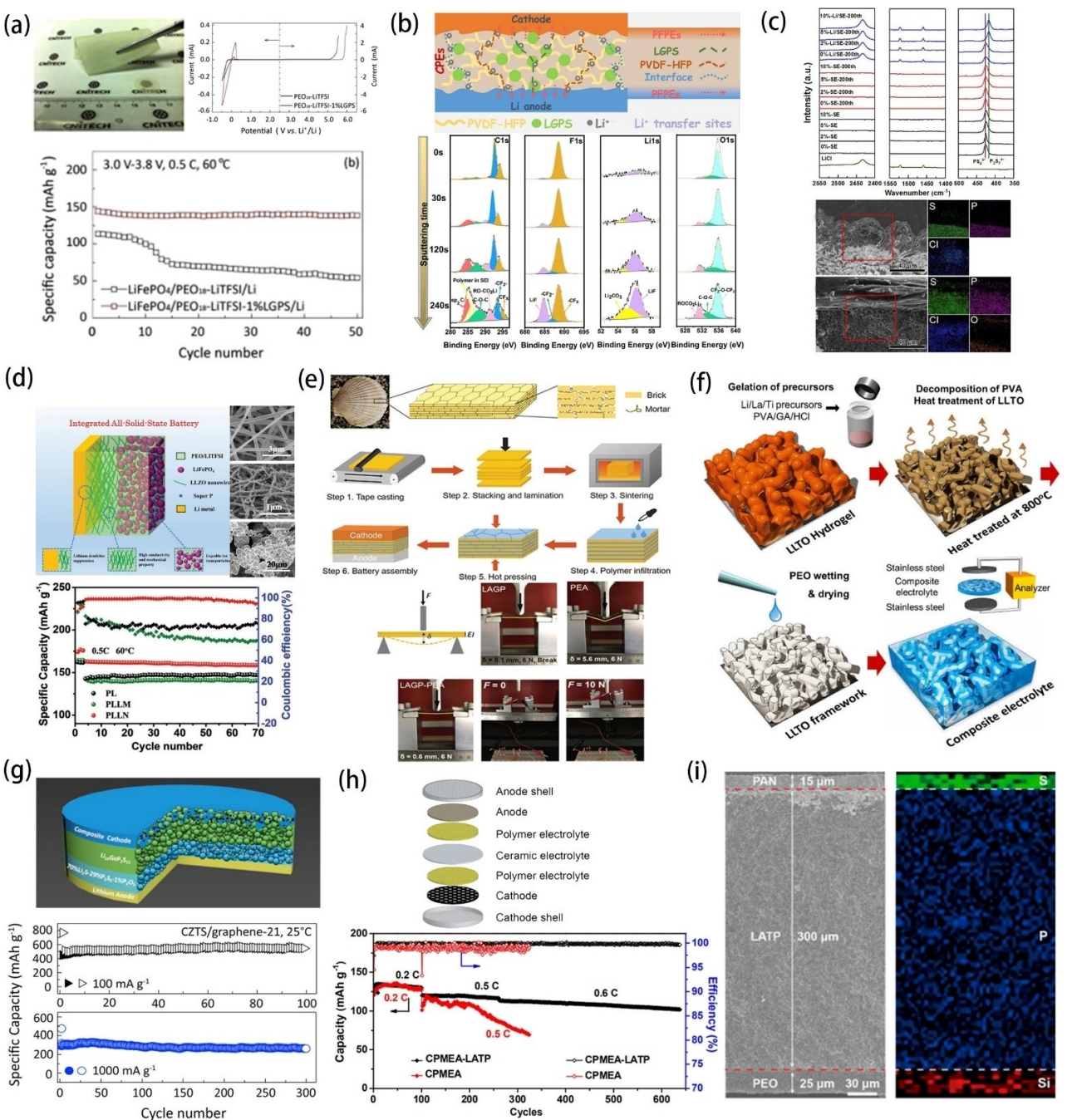


Figure 10. a) A photo of the LGPS-PEO membrane; LSV and CV curves of polymer electrolytes at 80°C and 0.5 mV s⁻¹. Cycle performance of all-solid-state LFP/PEO-LiTFSI-1%LGPS/Li cell and LFP/PEO-LiTFSI/Li cell.^[150] Reproduced with permission from Ref. [150], copyright 2015, Elsevier. b) Schematic illustration for multiple lithium ion transfer sites in PVDF-HFP and LGPS CSE; XPS spectra of C1s, F1s, Li1s, and O1s regions collected of the SEI layer formed in Li/PVDF-HFP/PFPEs/20 wt.% LGPS/Li cell at sputtering time of 0 s, 30 s, 120 s and 240 s, respectively.^[152] Reproduced with permission from Ref. [152], copyright 2019, Elsevier. c) Raman spectra of LiCl, synthesized Li_xPS₃Cl-x%PEO, bulk electrolytes and interfacial electrolytes in contact with lithium after 200 cycles at 0.05 C. The cross-sectional SEM images and the corresponding elemental mappings of the interface between Li_xPS₃Cl-x%PEO electrolytes and lithium: 0 wt.% and 5 wt.% after 200 cycles at 0.05 C.^[35a] Reproduced with permission from Ref. [35a], copyright 2019, Elsevier. d) Schematic illustration of an integrated all-solid-state LFP/LLZO nanowires/Li cell. SEM images of electrospun fibers of LLZO precursor, LLZO nanowires calcined at 700 °C, LLZO microparticles. Cycling performances of LiFePO₄/Li cells with three type LLZO at 0.5 C and 60 °C.^[158] Reproduced with permission from Ref. [158], copyright 2018, Wiley-VCH. e) The design and fabrication of nacre-like ceramic/polymer composite electrolyte. Schematic of staggered “brick-and-mortar” microstructure in nacre and the bottom-up fabrication process of NCPEs and battery assembly. Schematic of indenting a suspended pouch cell under point force: pure LAGP under 0.1 mm displacement, pure PEA film under 6 N load, and LAGP–PEA NCPE under 0.6 mm displacement and 6 N load. A structural LFP/LAGP–PEA NCPE/Li pouch cell lighting a series of LEDs under no load and 10 N load.^[159] Reproduced with permission from Ref. [159], copyright 2019, Wiley-VCH. f) Schematic of synthetic steps of LLTO framework composite electrolytes: LLTO hydrogel, decomposition and heat treatment, PEO wetting and drying.^[160] Reproduced with permission from Ref. [160], copyright 2018, Wiley-VCH. g) Protection of LGPS by a 70Li₂S·29P₂S₅·P₂O₅ interface. Cycling performance of all-solid-state Cu₂ZnSnS₄/LGPS/70Li₂S·29P₂S₅·P₂O₅/graphene cell between 0.5 V–3 V.^[164] Reproduced with permission from Ref. [164], copyright 2016, Elsevier. h) Illustration of all-solid-state battery design with the PCPSE electrolyte. Cycling and C-rate performance of the LFP/Li cells with CPMEA and CPMEA-LATP-based PCPSE.^[165] Reproduced with permission from Ref. [165], copyright 2016, American Chemical Society. i) SEM image and EDX of PAN–PEO double-layer polymer electrolyte.^[128] Reproduced with permission from Ref. [128], copyright 2019, American Chemical Society.

(PFPEs). Such SEI layer could avoid direct contact of LGPS with lithium thus suppressing Li dendrite growth (Figure 10b). PFPE polymer was also used to covalently bond with 75Li₂S·25P₂S₅ sulfide glass particles, the obtained non-flammable hybrid SSEs with 23 wt.% PFPE polymer indicated a wide electrochemical window and a capacity of limit the dissolution of lithium polysulfides, which is suitable for all-solid-state Li–S battery.^[153] And for the LGPS analogue, Li₁₀SnP₂S₁₂, PEO/Li₁₀SnPS₁₂ membrane was prepared for all-solid-state Li–S battery with a superior electrochemical performance.^[154] Meanwhile, poly(vinylchloride-acetate) (PVCA)–Li₁₀SnP₂S₁₂ CSEs were fabricated by Cui et al.^[155] via in-situ polymerization, the in-situ process was beneficial for building an integrated interface between electrodes and the CPE, thus decreasing interfacial impedance. Furthermore, argyrodite Li₆PS₅Cl and PEO matrix were also prepared in our works to inhibit the reaction between Li₆PS₅Cl and lithium.^[35a] And the mechanical property of the CSEs with different PEO content were also investigated by compression tests, the proportional limit reaches a value of 60 MPa for the optimal 5 wt.% PEO content, which was attribute to the addition of PEO with soft mechanical property. Moreover, as shown in Figure 10c, the reduced product Li₂S at Li/SE interface were suppressed with 5 wt.% and 10 wt.% PEO, and no Cl diffusion were observed at interface, which indicated that the added PEO could facilitate the formation of a stable interface. Lately, PEO–LiTFSI–Li₆PS₅Cl CSEs were prepared via slurry-based tape casting, the formed SEI layer between lithium and CPE40 (40 wt.% Li₆PS₅Cl) was proved to be a LiF and Li₂S-rich SEI layer.^[156] Besides, PEO–Li₃PS₄ hybrid polymer also exhibited a positive effect on the transference of lithium ion.^[157]

It is difficult for oxide-based SSEs to form good physical contact with electrode materials due to point contact at the solid-solid interface. Wan et al.^[158] prepared LLZO nanowires by electrospinning (Figure 10d). The ionic conductivity at RT with 10 wt.% LLZO nanowires and microparticles are 2.39×10^{-4} S cm⁻¹ and 7.34×10^{-5} S cm⁻¹, respectively. The all-solid-state LFP/LLZO nanowires/Li cell exhibits favorable electrochemical performance. Yang et al.^[159] prepared LAGP tables which draw inspiration from the structure of natural nacre (Figure 10e). The nacre-like ceramic/polymer electrolyte (poly(etheracrylate), NCPE) simultaneously possesses a much higher fracture strain than pure ceramic electrolytes, and a much larger ultimate flexural modulus (7.8 GPa) than pure polymer electrolytes (20 MPa). The electrochemical performance of NCPE is also much better than pure ceramic or polymer electrolytes, especially under mechanical load. The LAGP/NCPE exhibits stable cycling with a capacity retention of 95.6% over 100 cycles at RT, even undergoes a large point load of 10 N. Yu et al.^[160] designed a three-dimensional LLTO derived from hydrogel (Figure 10f). The ionic conductivity of the prepared PEO–LiTFSI–LLTO composite electrolyte reached 8.8×10^{-5} S cm⁻¹ at RT. The researchers used TiO₂ and La₂Ti₂O₇ to prepare a framework structure like the LLTO three-dimensional framework. The ionic conductivity of the CSEs is about one order of magnitude lower than that of the composite electrolyte with the LLTO framework.

4.1.3. Multi-layered Electrolytes

Another method to realize lithium compatible interfaces for ASSLBs is building multi-layered electrolytes. The ASSLBs employing bilayer electrolytes could achieve enhanced ionic conductivity and stability to lithium anode at the same time. Among all the SSEs, Li₃PS₄ has a relatively good stability with lithium anode.^[78a] In 2014, Shin et al.^[78b] fabricated all-solid-state TiS₂/Li–In cell employing Li₃PS₄ and LGPS bilayer due to LGPS suffer from poor stability with lithium in the low voltage range. And a stable interface formed between Li₃PS₄ and Li–In anode was proved through ex-situ XRD, which result in better battery performance. Besides, an oxysulfide originated from Li₃PS₄·75Li₂S·(25-x)P₂S₅·xP₂O₅ exhibits excellent electrochemical stability and compatibility with lithium electrode, which is attributed to its wide electrochemical window up to 10 V and a Li₂S buffer layer could be formed during the process of its reaction with lithium.^[161] Therefore, all-solid-state Li–S cell adopted an rGO@S–LGPS–AB cathode, LGPS/75Li₂S·24P₂S₅·P₂O₅ bilayer electrolyte, and lithium metal as anode showed high capacity, good cycling stability, and excellent rate capability.^[162] Meanwhile, Zhang et al.^[163] reported that Li/75Li₂S·24P₂S₅·P₂O₅/LGPS/10%RGO–VS₄@Li₇P₃S₁₁ ASSLBs also delivered high reversible capacity. Besides, 70Li₂S·29P₂S₅·P₂O₅ could also be inserted as a stable layer for ASSLBs to protect LGPS from react with lithium anode (Figure 10g).^[164] Accordingly, developing a relatively stable interface layer against lithium by insert a relative stable electrolyte layer is an efficient way to realize compatibility between the high conductive SSEs such as LGPS with Lithium.

In fact, Ti⁴⁺ is not compatible with lithium. The polymer/ceramic membrane/polymer sandwich electrolyte (PCPSE) proposed by Zhou et al.^[165] solves this problem well (Figure 10h). All-solid-state Li/LFP cell with the PCPSE showed a notably high Coulombic efficiency of 99.8–100% over 640 cycles. Guo et al.^[128] coated polyacrylonitrile (PAN) and PEO polymers on both sides of LATP to obtain a composite solid electrolyte (Figure 10i). PAN is in contact with the cathode NMC to withstand high voltage. PEO prevents LATP from being reduced between lithium and LATP. In addition, LATP with a high lithium ion migration number can induce a uniform distribution of lithium ion flux, which can effectively suppress the space charge layer at the interface and prevent the generation of lithium dendrites. The full battery assembled with this composite solid electrolyte can achieve 120 cycles of stable cycling and a capacity retention rate of 89%.

4.2. Building Interphase at Interfaces

4.2.1. Coating on the Surface of Cathode Materials

To suppress the diffusion phenomenon and realize intimate contact between SSEs and cathode, many researches have focus on introducing a buffer layer by coating on cathode materials. As early as 2006, Ohta et al.^[166] reported a LTO film with a thickness ranging from 1.1 to 38.9 nm coated LCO

particles by a spray-coating method. Compared with the uncoated LCO, as shown in Figure 11a, the interfacial resistance of the LCO/ $\text{Li}_{3.25}\text{Ge}_{0.25}\text{P}_{0.75}\text{S}_4$ is smaller due to the inhibition ability of the LTO coating layer, which also enhanced electrochemical performance of ASSLBs. However, the ionic conductivity of LTO is low. Inspired by this, the LiNbO_3 (LNO) layer with a relatively high ionic conductivity was used to replace LTO to achieve smaller interfacial resistance and uniform coating (Figure 11b).^[167] Further, as summarized in Table 4, oxide coating materials such as Li_2SiO_3 , Li_3PO_4 and $\text{Li}_2\text{O}\cdot\text{ZrO}_2$ were also coated on the cathode materials such as NMC, NCA and LFP.^[117,168] Recently, Cao et al.^[105b] prepared a thin amorphous $\text{Li}_{0.35}\text{La}_{0.5}\text{Sr}_{0.05}\text{TiO}_3$ (LLSTO) layer which was in-situ coated on the NMC surface via wet chemical method to stabilize the NMC-thiophosphate SEs interface. Such a high ionic conductive but electronic insulating LLSTO film was introduced at NMC/ $\text{Li}_6\text{PS}_5\text{Cl}$ interface, which can avoid the degradation of $\text{Li}_6\text{PS}_5\text{Cl}$ at higher

voltage and enhancing electrochemical kinetics. Therefore, all-solid-state NMC–LLSTO/ $\text{Li}_6\text{PS}_5\text{Cl}/\text{Li}$ –In cell exhibited a capacity retention of 91.5% after 850 cycles (Figure 11c). Except for oxides coating, LCO cathode was coated with $80\text{Li}_{2}\text{S}\cdot20\text{P}_{2}\text{S}_5$ SSE via PLD method, as the dense composite layer shown in Figure 11d, intimate contact between them was achieved, thus ASSLBs exhibited high cycle performance.^[169] And The Li_4SnS_4 exhibited higher thermal stability than Li_3PS_4 , which suppressed the decomposition reactions at the interfaces with NMC.^[170]

4.2.2. Coating on the Surface of Anode Materials

Another obstacle to the large-scale application of SSEs is the unstable interface between lithium and SSE due to the formation of a solid interphase layer. And almost all SSEs are unstable against lithium, such as LGPS, which will generate

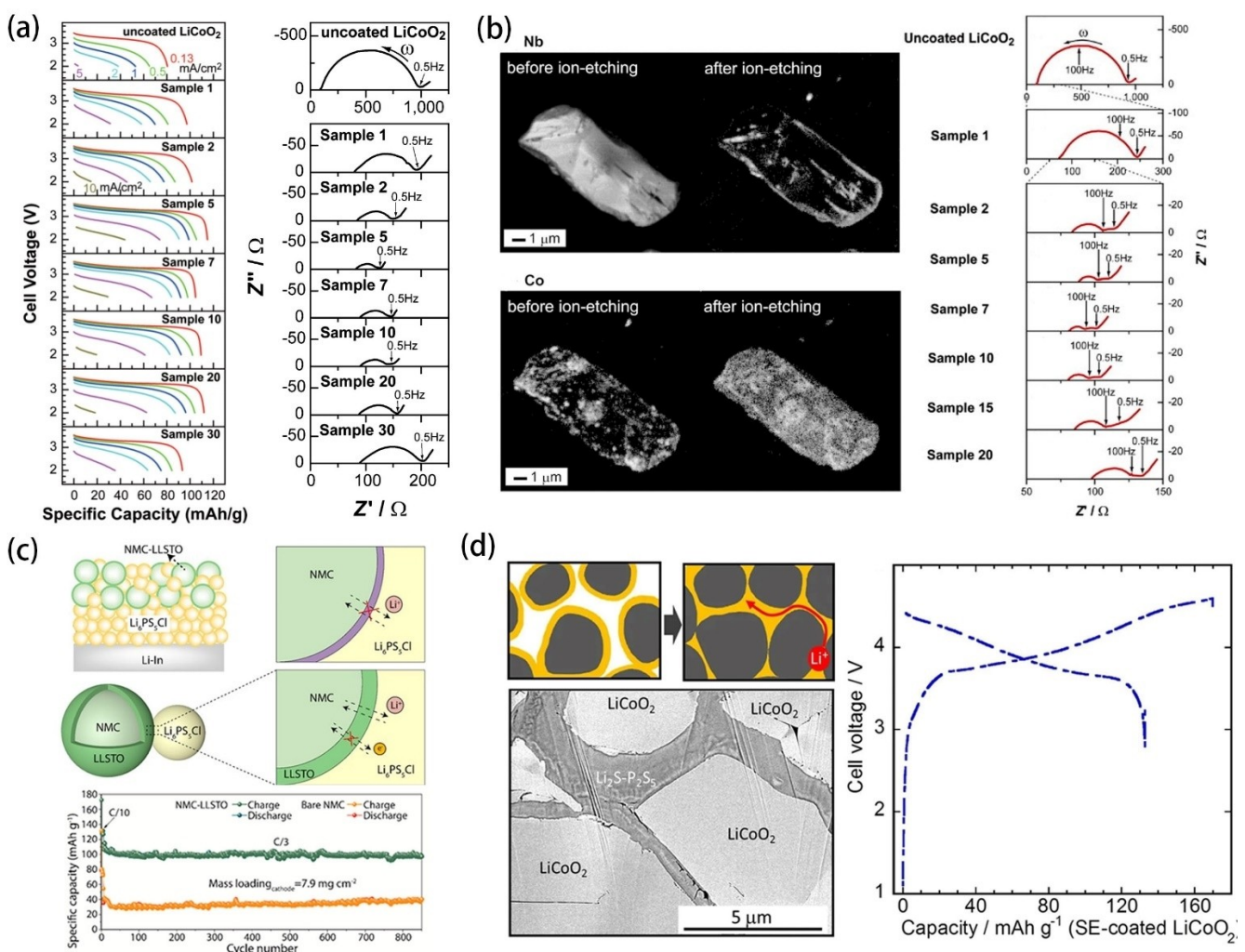


Figure 11. a) Discharge curves and Nyquist plots of the Li–In/LCO cells: uncoated and LTO-coated LCO.^[166] Reproduced with permission from Ref. [166], copyright 2006, Wiley-VCH. b) SEM images of the LNO-coated LCO particle of sample 7 for Nb and Co. The left and right images were taken before and after the ion-etching, respectively. Nyquist plots of the Li–In/LCO cells: uncoated and LNO-coated LCO.^[167] Reproduced with permission from Ref. [167], copyright 2007, Elsevier. c) Failure mechanism at the interface in bare NMC-based ASSLBs and interface stabilization effect with LLSTO layer. Long-term cycling performance of bare NMC and NMC–LLSTO.^[105b] Reproduced with permission from Ref. [105b], copyright 2020, American Chemical Society. d) Schematic diagram of 80Li₂S·20P₂S₅–LCO composite electrode, cross-sectional SEM images of 80Li₂S·20P₂S₅–LCO composite electrode. Charge–discharge curves of the coated LCO/80Li₂S·20P₂S₅/graphite cell at a current density of 11 mA g^{−1}.^[169] Reproduced with permission from Ref. [169], copyright 2013, The Authors.

Table 4. Approaches to stabilize interface between cathodes and inorganic SSE by building interphase at interface.

Electrode	Inorganic SSEs	Modification Layer	Method	Ref.
LiCoO ₂	Li ₂ S-P ₂ S ₅	Li ₂ CO ₃	Wet chemical method (LiOH solution)	[216]
LiCoO ₂	Li ₂ S-P ₂ S ₅	Li ₂ SiO ₃	Sol-gel method	[168c]
LiCoO ₂	Li ₁₀ GeP ₂ S ₁₂	LiNbO ₃	ALD	[104]
LiCoO ₂	Li _{3.25} Ge _{0.25} P _{0.75} S ₄	Li ₄ Ti ₅ O ₁₂	Spray-coating	[166]
NMC	Li ₃ PS ₄	LiAlO ₂	Sol-gel method	[217]
NMC	Li ₆ PS ₅ Cl	LiNbO ₃	Wet chemical method (Ethanol)	[35b]
NMC	Li ₆ PS ₅ Br	LiNbO ₃	Spray-coating	[218]
NMC	Li ₆ PS ₅ Cl	Li _{0.35} La _{0.5} Sr _{0.05} TiO ₃	Wet chemical method (LLSTO solution)	[105b]
NMC	Li ₆ PS ₅ Cl	Li _{0.5} La _{0.5} TiO ₃	Sol-gel method	[219]
NCM	Li ₁₀ GeP ₂ S ₁₂	LiCoO ₂ +LiNbO ₃	Wet chemical method (Ethanol)	[220]
NCA	Li ₂ S-P ₂ S ₅	Li ₄ Ti ₅ O ₁₂	Spray-coating	[221]
NCA	Li ₁₀ GeP ₂ S ₁₂	LiNbO ₃	Wet chemical method (Nb(C ₂ H ₅ O) ₅ and C ₂ H ₅ OH solution)	[222]
NCA	Li ₁₀ GeP ₂ S ₁₂	Li ₂ O-ZrO ₂	Sol-gel method	[117]
LiNi _{0.5} Mn _{1.5} O ₄	Li ₁₀ GeP ₂ S ₁₂	LiNbO ₃	Sol-gel method	[168b]
LiNi _{0.5} Mn _{1.5} O ₄	Li ₂ S-P ₂ S ₅	Li ₃ PO ₄	PLD	[223]
LiCoO ₂	LLZO	Nb	PLD	[224]
NMC	LLZO	Li-Ti-O	Wet chemical method (precursor Li(4)-Ti(5)-O(12) solution)	[225]

poor conducting interphase (Li₂S, Li₃P, Li₁₅Ge₄) when contacting with lithium.^[119b] Consistent with the improvements implemented on the cathode/SSEs interface to address interface problems, similar protective layer was also built on the surface of lithium, as summarized in Table 5. In 2012, a thin silicon layer was inserted in the SSEs/Li anode interface by pulsed laser decomposition (PLD), improved cycling performance was achieved because Si layer reduced the reduction power of lithium anode kinetically.^[171] Lately, Zhang et al.^[172] put forward a more effective interface engineering strategy that a LiH₂PO₄ layer was in-situ formed in lithium anode (Figure 12a) via a manipulated reaction between H₃PO₄ contained THF solvent with Li to prevent LGPS/Li interface from intrinsic interfacial issues. The LiH₂PO₄ layer was also provided an intimate contact with lithium, which was confirmed through SEM results. And LCO/LGPS/LiH₂PO₄-Li ASSLBs delivered high reversible discharge capacity (118.7 mAh g⁻¹) after 500 cycles, which also proved the stabilization effect of LiH₂PO₄ layer on the LGPS/Li interface. Xu et al.^[173] coated uniform LiF/LiI layer on lithium via exposing lithium metal to methoxyperfluorobutane (HFE)/I₂ on the surface. Such interphase layer significantly suppressed Li dendrite due to the effects that HFE/I₂ could react with lithium metal forming LiF/LiI and further consuming Li dendrite when Li dendrite breaks the LiF/LiI coated layer. Introducing a thin

lithium ion conducting interlayer is also a promising approach to address the problems associated with SSEs/Li interface. In 2012, Nagao et al.^[174] inserted an In layer with a thickness of 500 nm onto the surface of Li₂S-P₂S₅ via vacuum evaporation, which promoted the alloy reaction between lithium and In to develop an intimate contact. The alloy layer also brought a fast lithium ion transport and a good cyclability for excellent battery performance. Later, Li-Al alloys, Li-Au alloys, Li-Si alloys and Li-Sn alloys with higher redox potentials were also developed to act as anode directly to improve the interface stability of anode/SSEs and enhance the reversibility of lithium utilization.^[120,175] Despite using alloy could decrease the side reaction, the generated interphases are electronic conductive. Sang et al.^[176] prepared Al₂O₃ interlayer and Si interlayer by atomic layer deposition (ALD) on Li₇P₃S₁₁. The XPS and in-situ Raman (Figure 12b) results proved that Li₄P₂S₆ and Li₂S was formed at the interface at lithium ion reducing potentials. Compared with the Si interlayer, the LiAlO interlayer was proved to be an effective strategy which could drop the potential after cycling between sulfide and lithium hence suppressing sulfide decomposition. Besides, PEO-SSEs composite interlayer was also studied, Sang et al.^[177] adopted PEO and LiTFSI in argyrodite Li₆PS₅Cl to form a stable CPE interlayer with a low resistance and activation, which was attributed to the

Table 5. Approaches to stabilize interface between anodes and inorganic SSE by building interphase at interface.

Electrode	Inorganic SSEs	Modification Layer	Method	Ref.
Lithium	Li ₇ P ₃ S ₁₁	LiF or LiI	Wet chemical method (HFE or I ₂ solution)	[173]
Lithium	Li ₁₀ GeP ₂ S ₁₂	LiH ₂ PO ₄	Wet chemical method (THF solution)	[172]
Lithium	Li ₃ PS ₄	Au	Vacuum evaporation	[226]
Lithium	Li ₂ S-P ₂ S ₅	Si	PLD	[171]
Lithium	LLZO	Al ₂ O ₃	ALD	[183]
Lithium	LLZO	MoS ₂	Polishing method	[185]
Lithium	LLZO	PDMS	50 μm PDMS film was added to 500 μm lithium foil	[186]
Lithium	LLZO	g-C ₃ N ₄	The g-C ₃ N ₄ powder was added into the molten lithium	[227]
Lithium	LLZO	Cu ₆ Sn ₅	Magnetron sputtering	[228]
Lithium	LATP	Ge	Magnetron sputtering	[229]
Lithium	LATP	Cr	Magnetron sputtering	[230]
Lithium	LATP	AN	Wet chemical method (AN solution)	[231]
Lithium	LATP	ZnO	Magnetron sputtering	[182]

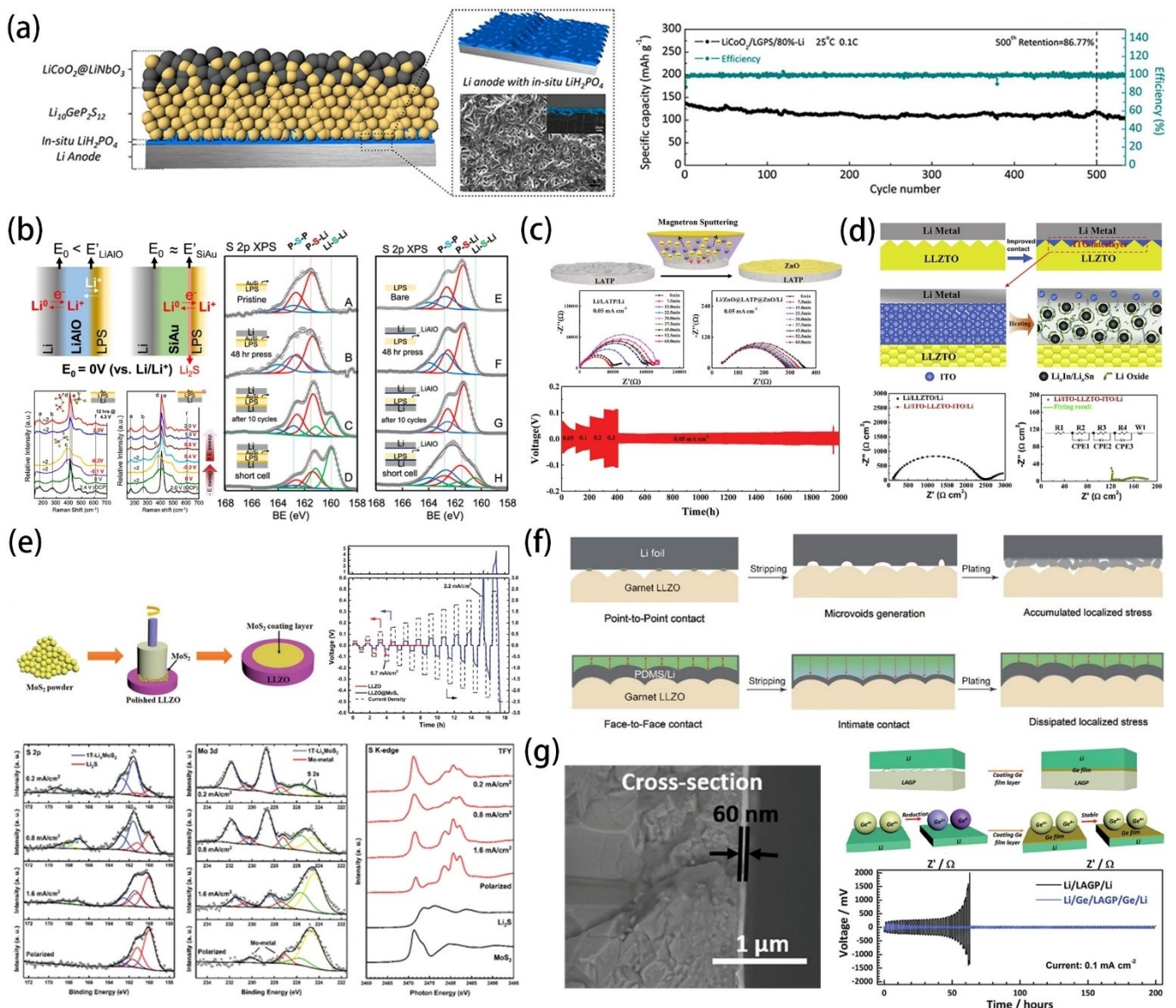


Figure 12. a) Schematic of the LCO/LGPS/LiH₂PO₄-Li cell with optimized structure. And long cycle of LCO/LGPS/80%-Li cell.^[172] Reproduced with permission from Ref. [172], copyright 2018, American Chemical Society. b) Electrochemical potential variation of the Au/Li₃P₃S₁₁ interface with LiAlO and Si interlayer after cycling. In-situ Raman spectra obtained in Li/Li₃S₁₁/Au cell and Li/Li₃P₃S₁₁/Au-Si cell. The S 2p XPS spectra obtained at Li₃P₃S₁₁ surface before and after assembled/cycled in Li/Li₃P₃S₁₁/Li symmetric cell in the presence of Au-Si (A-D) and LiAlO (E-H) interlayers.^[176] Reproduced with permission from Ref. [176], copyright 2018, American Chemical Society. c) Schematic of the preparation of ultrathin ZnO layer coated LATP pellet by magnetron sputtering. Nyquist plots of Li/LATP/Li and Li/ZnO@LATP@ZnO/Li symmetric cells during the first cycle at 0.05 mA cm⁻². Long cycling performance of Li/ZnO@LATP@ZnO/Li symmetric cells at various current densities (0.1, 0.2, 0.3 mA cm⁻²).^[182] Reproduced with permission. copyright 2019, Wiley-VCH. d) Schematic of preparing an indium tin oxide (ITO) coating layer on a LLZTO pellet. Comparison of EIS profiles of the symmetric cells using LLZTO with and without ITO modification.^[184] Reproduced with permission from Ref. [184], copyright 2019, Elsevier. e) Schematic of preparing a MoS₂ coating layer on a LLZO pellet. Galvanostatic cycling of the symmetric cell with and without MoS₂ at step-increased current densities. The S 2p, Mo 3d XPS spectra of the cycled samples (cycled at 0.2, 0.8, and 1.6 mA cm⁻², respectively, for 15 hours) and the polarized sample (held at the polarized state for more than half an hour). S K-edge XAS spectra detected in TFY mode of the same four samples.^[185] Reproduced with permission from Ref. [185], copyright 2019, Royal Society of Chemistry. f) Schematic illustration of the stress self-adapted interface by using compressible PDMS/Li.^[186] Reproduced with permission from Ref. [186], copyright 2020, American Chemical Society. g) Schematic diagrams of the amorphous Ge film coating between Li and LAGP. Cross-sectional SEM image of Ge-coated LAGP pellet. Cycling performance of the Li/Ge/LAGP/Ge/Li and Li/LAGP/Li symmetric cells at 0.1 mA cm⁻².^[187] Reproduced with permission from Ref. [187], copyright 2017, Wiley-VCH.

formation of polysulfides and LiF. Lately, 0.75Li₂S·0.25P₂S₅ glass was introduced in the Li₆PS₅Cl/In interface to fabricate ASSLBs. Compared to a battery without elastic interface layer, the battery demonstrated decreased electrolyte resistance and suppressed interfacial deterioration.^[178] Moreover, organic materials were also employed to stabilize the interface between

SSEs and anode. Wang et al.^[179] reported that an organic-inorganic hybrid interlayer (alucone) was used at the Li/Li₁₀SnP₂S₁₂ surface via molecular layer deposition, the alucone layer could act as an artificial SEI to suppress the growth of lithium dendrites, and ASSLBs with alucone on lithium anode exhibited high cycling performance. The thin Ag-C layer on

lithium side can effectively regulate Li deposition, which leads to a superior cycle life ($>1,000$ times) for NMC/Li₆PS₅Cl/Li battery.^[180]

Liu et al.^[181] soaked the polished metallic lithium foil into the solution (0.4 wt.% polyphosphoric acid (PPA) in DMSO solution) for 2 minutes to form an artificial Li₃PO₄ SEI layer with a thickness of about 200 nm. They found that the impedance of the assembled symmetrical battery with LEs did not increase by more than ten times after special treatment of lithium. The results of galvanostatic charge-discharge measurement show that the as-assembled battery delivers an excellent capacity retention ratio of 95.2% at 0.1 C rate after 50 cycles, which is much higher than untreated samples. He et al.^[182] constructed an ultrathin and uniform ZnO layer on the surface of LATP via magnetron sputtering (Figure 12c). It was found that the ultrathin ZnO layer and Li metal formed a multifunctional interface layer (Zn + Li₂O) through in-situ reaction. The interface layer significantly increased the compatibility of LATP and lithium metal, which can reduce the interfacial resistance. And the Li/ZnO@LATP@ZnO/Li symmetric cells showed excellent cycle stability for 2000 h at 0.05 mA cm⁻². Hu et al.^[183] used ultrathin Al₂O₃ by ALD to address the large interfacial impedance between lithium and garnet, which can significantly improve the interface contact. And by modifying the surface of the Li_{6.4}La₃Zr_{1.4}Ta_{0.6}O₁₂ (LLZTO) pellets with indium tin oxide (ITO), lithium was tightly soldered on the garnet pellets through rapid reaction with the ITO interlayer.^[184] In Figure 12d, the interfacial resistance of Li/LLZTO dramatically decreased from 1192 Ω cm² to 32 Ω cm². Fu et al.^[185] proposed a method of coating MoS₂ on LLZO and forming an intermediate layer in-situ to reduce the Li/LLZO interfacial impedance and inhibit the growth of lithium dendrites (Figure 12e). The interface resistance was significantly reduced to only 14 Ω cm² after modification, and the critical current density was increased from 0.7 mA cm⁻² to 2.2 mA cm⁻². In addition, batteries can undergo significant polarization rather than short circuits when the current density is higher than the critical current density. X-ray photoelectron spectroscopy and absorption spectroscopy show that the nanoscale MoS₂ thin layer in contact with lithium can be transformed into an intermediate layer composed of Mo and Li₂S, which is dynamically stable at low current density. However, it will continue to thicken when the current density is too large, which effectively hinders the further reaction between Li and MoS₂. Luo et al.^[186] demonstrated a stress self-adapted Li/garnet interface by integrating lithium foil with the polydimethylsiloxane (PDMS). Owing to the inherent super elasticity of PDMS, stresses generated during the lithium depositing/stripping process can be stored and automatically released when needed. The Li/garnet interface can achieve continuous conformal face-to-face contact under continuous and uniform compressive stress, which further eliminates local residual stress generated during the lithium deposition process and mitigates the Li dendrite growth and electrolyte cracks (Figure 12f). The cycle life of a PDMS/Li/garnet/PDMS/Li cell can reach more than 1800 h at 0.2 mA cm⁻². In contrast, Li/garnet/Li cell has a cycle life of only 35 h at 0.1 mA cm⁻². In view of the instability of LAGP to metal Li, Liu et al.^[187] used a method of

sputtering a Ge amorphous film on the surface of LAGP to successfully suppress the reduction of Ge⁴⁺ to Ge⁰ and Ge²⁺, and made the metal Li and LAGP solid electrolyte tightly connected (Figure 12g). The symmetrical cell with the Ge-coated LAGP shows superior stability and cycling performance for 100 cycles of 0.1 mA cm⁻².

4.3. Post-Synthesis Treatments

Co-sintering is also an interface treatment method in order to obtain a closer interface contact, while preventing interfacial reactions. About sulfide-based SSEs, the wet mixing and sintering method is usually used to prepare composite electrodes. Han et al.^[188] proposed a bottom-up approach to prepare the Li₂S composite cathode. By dissolving Li₂S, poly(vinylpyrrolidone) (PVP) and Li₆PS₅Cl in ethanol solution, the mixed conducting electrode went through coprecipitation and high-temperature carbonization. The uniform distribution of carbon, sulfur, and chlorine from Figure 13a implies the nanoscale distribution of Li₂S, Li₆PS₅Cl, and carbon. The high magnification TEM is also used to reveal the distribution of these components, which enables the facile transport of both lithium ions and electrons at interface. Xu et al.^[189] reported that a uniform coating (Figure 13b) of Li₂P₃S₁₁ on MoS₂ was heated at 250 °C to form a MoS₂/Li₂P₃S₁₁ composite electrode. The interfacial architecture on MoS₂ particles can guarantee the intimate contact during cycling, which can offer more active sites and restrain interfacial reaction. In Figure 13c, the XRD patterns confirm that the solidification of Li₆PS₅Cl is not affected by other components.^[190] To get the intimate ionic contacts and favorable ionic percolation, the liquefied SSEs are infiltrated into the tortuous porous structures of electrodes and solidified. Similarly, LCO coated by solidified Li₄SnS₄ (at 320 °C) from aqueous solutions significantly outperformed the conventional mixed electrodes.^[191] The Nyquist plots and galvanostatic intermittent titration technique (GITT) (Figure 13d) with uncoated and coated electrodes show a big difference in interfacial resistance and polarization, which indirectly proves the inhibition of interfacial reactions by co-sintering. For NMC, the well-dispersed in the Li₃PS₄ matrix also proves this conclusion.^[192] Employing LCO electrodes tailored by the infiltration of Li_{6.5}P_{0.5}Ge_{0.5}S₁-ethanol solutions achieved the promising electrochemical performances of ASSLBs.^[193]

Liu et al.^[194] coated V₂O₅ onto Li-La_{2.75}Ca_{0.25}Zr_{1.75}Nb_{0.25}O₁₂ electrolyte and then rapid annealing (Figure 13e). After rapid thermal annealing, the resistance at RT dramatically decreased from 2.5×10^4 to 71 Ω cm². The battery with rapid thermal annealing was cycled at 100 °C at 50, 100, 150, and 200 mA g⁻¹ and recovered to 50 mA g⁻¹. After applying a high current density, the capacity returned to 150 mA h g⁻¹ at 50 mA g⁻¹, indicated that the cathode/garnet interface remains stable and reversible at current densities up to 200 mA g⁻¹. The $>97\%$ Coulombic efficiency during cycling indicates the good electrochemical stability of garnet SSE with lithium anode. Ohta et al.^[195] found that the sintering temperature of Li_{6.8}La_{2.95}Ca_{0.05}Zr_{1.75}Nb_{0.25}O₁₂ was significantly reduced to 790 °C

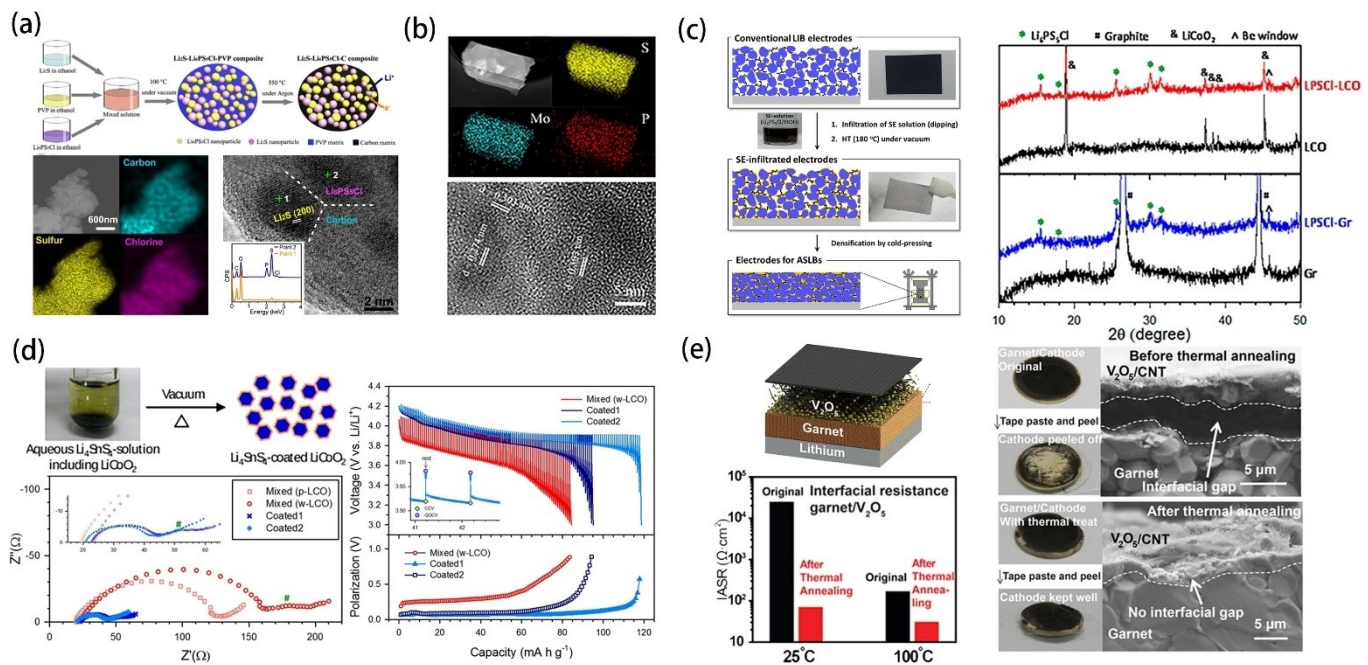


Figure 13. a) Schematic illustration of the bottom-up synthesis of the mixed conducting Li_2S nanocomposite. The elemental mappings of carbon, sulfur and chlorine in the composite. The high-resolution TEM image of the as-obtained $\text{Li}_2\text{S}-\text{LiPS}_2\text{Cl}-\text{C}$ nanocomposite, and the inset shows the EDS results at point 1 and point 2, respectively.^[188] Reproduced with permission from Ref. [188], copyright 2016, American Chemical Society. b) Elemental mapping images and HRTEM image of sulfur, phosphorus and molybdenum of the $\text{MoS}_2/\text{Li}_2\text{P}_3\text{S}_{11}$ composite.^[189] Reproduced with permission from Ref. [189], copyright 2017, Elsevier. c) Schematic diagram illustrating the infiltration of conventional LIBs composite electrodes with solution-processable SEs. The XRD patterns of LCO and Gr electrodes before and after the infiltration of solution-processed LiPS_2Cl .^[190] Reproduced with permission from Ref. [190], copyright 2017, American Chemical Society. d) Schematic illustration of the aqueous-solution process for Li_4SnS_4 -coated LCO for ASLBs. Nyquist plots and discharge-voltage profiles of the mixed electrodes and Li_4SnS_4 -coated LCO electrodes, and their corresponding polarization plots obtained by GITT.^[191] Reproduced with permission from Ref. [191], copyright 2017, Wiley-VCH. e) Schematic of the ASLBs and properties of garnet SSE. Comparison of interfacial charge transfer resistance originally and after rapid thermal annealing at 25 and 100 °C.^[194] Reproduced with permission from Ref. [194], copyright 2017, American Chemical Society.

by adding Li_3BO_3 and Al_2O_3 . The sintered electrolyte still showed a high ionic conductivity of 0.36 mS cm^{-1} at 25 °C. The ASLBs were successfully prepared by co-sintering the electrolyte and LCO, followed by coating of lithium, which the first discharge specific capacity was 78 mA h g^{-1} .

5. Conclusions and Outlook

The research of ASLBs based on inorganic SSEs provides a wide development for further improving energy density and safety. It also affords a feasible research path for developing the battery systems with high energy density. However, from an electrochemistry perspective, the understanding of the solid electrodes/SSEs (solid/solid) interface mechanism is still immature, which is far from reaching the recognition level of solid electrodes/LEs (solid/liquid) interface mechanism. It can even be said that solid/solid interface is still at a "preliminary" stage of understanding. Here, we provide our perspectives (Figure 14) about interfacial reaction, as follows:

- (1) Electrochemical windows and interfaces within inorganic SSEs. Different theoretical and experimental results have shown the different intrinsic thermodynamic electrochemical windows of inorganic SSEs. The thermodynamic calculation results prove that a wide voltage window detected by some experiments is triggered by dynamic

factors, not inherent thermodynamic stability factors. In terms of kinetics, the decomposition reaction is sluggish. However, whether the chemical reaction is slow or not, it still affects the electrochemical stability to different degrees. The unstable SSEs bring different interfacial issues within SSEs or interface at electrode, which can adversely affect the battery performance.

- (2) The interfacial reaction between inorganic SSEs and electrode materials. In most cases, the working voltage of the cathode material is not very wide, interlayers are formed as a result of the chemical reactions between SSEs and electrode materials. The electrochemical process can accelerate degradation of the interphase with lithium depositing and stripping. For cathode materials, the interfacial reaction can cause the elemental interdiffusion (especially oxides) and the decomposition of SSEs at interface. As the interfacial reaction occurs, lithium concentration at interface and interfacial microstructure also change, resulting in the lithium-depleted layer (SCL) and the chemo-mechanical failure, respectively. For anode material, lithium metal is widely used in ASLBs as an ideal anode material. The properties of reaction products (ionic and/or electronic conductors) at Li/SSEs interface determine whether a stable interface can be formed. Meanwhile, the lithium dendrite also exists along with the interfacial reaction occurs.

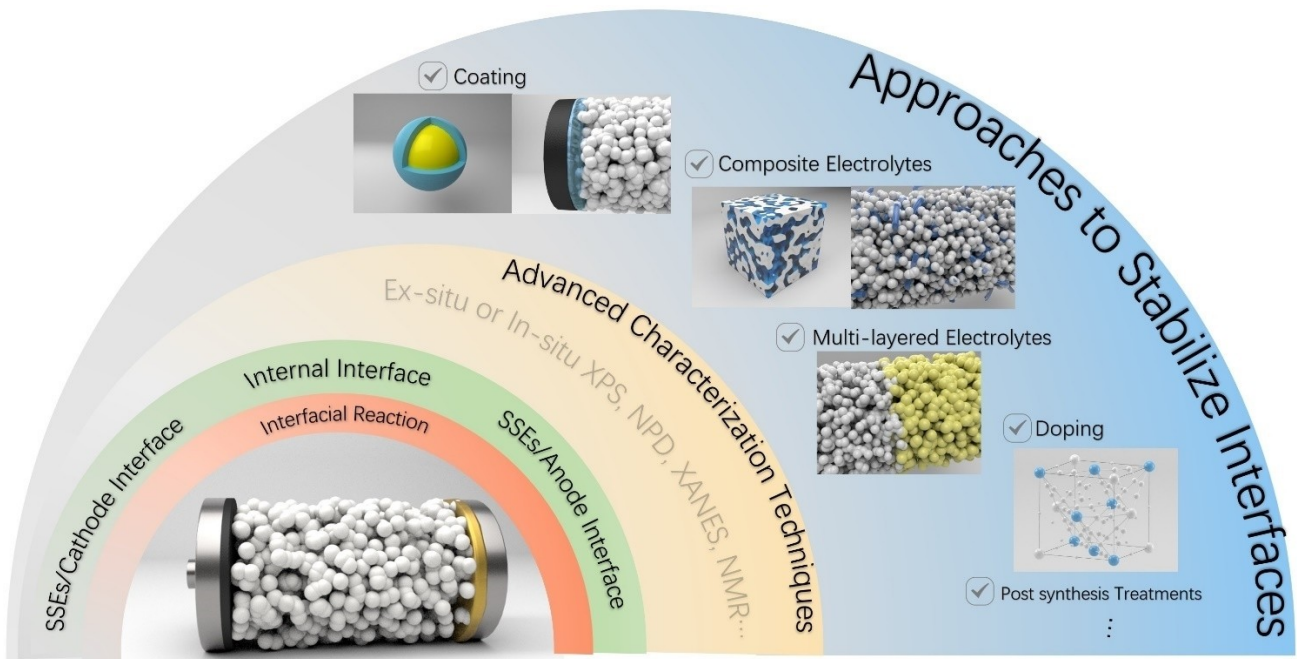


Figure 14. Perspectives for interfacial reaction in ASSLBs with inorganic SSEs.

- (3) Approaches to stabilize interfaces of inorganic SSEs. A stable interface is ion-conductive and electron-insulative, and without further degradation of SSEs or electrode material. Forming a desirable interface and controlling the chemical reaction between electrolyte and electrode is a critical step for the design of an ASSLB. The intrinsic stability windows of SSEs are very important to form a stable interface, many modifications of electrolyte composition have been applied to extend the electrochemical window of SSEs, like doping equivalent or aliovalent ions, compositing with polymers, building multi-layered electrolytes. The modifications of cathode/SSEs and anode/SSEs interfaces via coating or introducing interlayer (via wet or dry chemical methods) also have been proven to be effective. For anode/SSEs interface, a protective layer (*in-situ* formation) usually provides various ion transport channels and prevents lithium dendrite growth.
- (4) Characterization techniques. Solid materials are far less permeable to light than gas and liquid materials, which is very difficult to study the solid/solid interface directly by spectroscopic method. So, many advanced ex-situ and *in-situ* techniques, such as synchrotron X-ray techniques, solid-state NMR techniques, neutron scattering techniques, etc., can be used to investigate mechanisms of ASSLBs. Synchrotron radiation can obtain structural and chemical information with different levels of spatial and temporal length scales at interface. NMR can explore the ionic movements and local structure of SSEs at the atomic level. Neutron scattering techniques (included Neutron powder diffraction, Neutron total scattering, Neutron depth profiling, Neutron imaging, etc.) has some unique merits, which can provide more information about structure and dynam-

ics of SSEs in a wide range of time and length scales. The interfacial reaction during cycling are complicated, which involves chemical, physical and mechanical issues. In order to clearly understand the interfacial reaction, the combination of these advanced technologies is very important.

This review focuses more on the chemical composition variations at solid/solid interface. At solid/solid interface, the decomposition products are difficult to diffuse, which will continuously accumulate and increase. Therefore, it is required that the interface layer should be as thin as possible, the interfacial reactions should be as mild as possible (or Coulomb efficiency as high as possible). Furthermore, the stable interface needs a higher requirement on modification of electrolyte composition and the third phase interface in ASSLBs. The change of mechanical properties of inorganic SSEs caused by interfacial reactions, meanwhile, is a new field for further research. The interfacial evolution between electrode and inorganic SSEs and the growth of lithium dendrites are closely related to the mechanical properties of electrolyte, which are crucial with regards to the fabrication and performance of ASSLBs. Considering the tremendous achievements and progress of the solid-state electronics (such as the new-energy vehicles), we believe that in the future, the solid/solid interfacial reaction can be deeply understood, precisely controlled and utilized through rational interface design. And a great amount of attention needs to be given to the combination and comparative analysis of theoretical calculations and experimental data. Finally, there is a long way to go to achieve large-scale application.

Acknowledgements

The authors acknowledge the support by Zhejiang Provincial Natural Science Foundation of China under grant No. LR20E020002, and the National Natural Science Foundation of China (NSFC) under grant No. 21972127, 51677170, 51777194, and 51722210.

Conflict of Interest

The authors declare no conflict of interest.

Keywords: all-solid-state lithium batteries • inorganic solid-state electrolytes • interface • lithium batteries • interfacial reactions

- [1] J. Valenciano, M. Fernández, F. Trinidad, L. Sanz, *J. Power Sources* **2009**, 187, 599–604.
- [2] A. K. Shukla, M. K. Ravikumar, T. S. Balasubramanian, *J. Power Sources* **1994**, 51, 29–36.
- [3] J. B. Goodenough, Y. Kim, *Chem. Mater.* **2010**, 22, 587–603.
- [4] R. Yan, Q. Wang, *Adv. Mater.* **2018**, 30, 1802406.
- [5] Q. Ni, Y. Bai, F. Wu, C. Wu, *Adv. Sci.* **2017**, 4, 1600275.
- [6] M. A. Hannan, M. M. Hoque, A. Mohamed, A. Ayob, *Renewable Sustainable Energy Rev.* **2017**, 69, 771–789.
- [7] a) E. Quararone, P. Mustarelli, *Chem. Soc. Rev.* **2011**, 40, 2525–2540; b) J. B. Goodenough, K.-S. Park, *J. Am. Chem. Soc.* **2013**, 135, 1167–1176.
- [8] Z. Xue, D. He, X. Xie, *J. Mater. Chem. A* **2015**, 3, 19218–19253.
- [9] a) G. Zhou, F. Li, H.-M. Cheng, *Energy Environ. Sci.* **2014**, 7, 1307–1338; b) X.-X. Zeng, Y.-X. Yin, N.-W. Li, W.-C. Du, Y.-G. Guo, L.-J. Wan, *J. Am. Chem. Soc.* **2016**, 138, 15825–15828; c) N.-W. Li, Y. Shi, Y.-X. Yin, X.-X. Zeng, J.-Y. Li, C.-J. Li, L.-J. Wan, R. Wen, Y.-G. Guo, *Angew. Chem. Int. Ed.* **2018**, 57, 1505–1509; *Angew. Chem.* **2018**, 130, 1521–1525.
- [10] R. Chen, W. Qu, X. Guo, L. Li, F. Wu, *Mater. Horiz.* **2016**, 3, 487–516.
- [11] J. C. Bachman, S. Muy, A. Grimaud, H.-H. Chang, N. Pour, S. F. Lux, O. Paschos, F. Maglia, S. Lupart, P. Lamp, L. Giordano, Y. Shao-Horn, *Chem. Rev.* **2016**, 116, 140162.
- [12] Q. Zhang, D. Cao, Y. Ma, A. Natan, P. Aurora, H. Zhu, *Adv. Mater.* **2019**, 31, 1901131.
- [13] a) W. Xiao, J. Wang, L. Fan, J. Zhang, X. Li, *Energy Storage Mater.* **2019**, 19, 379–400; b) N. Zhao, W. Khokhar, Z. Bi, C. Shi, X. Guo, L.-Z. Fan, C.-W. Nan, *Joule* **2019**, 3, 1190–1199.
- [14] a) O. Reckeweg, B. Blaschkowski, T. Schleid, Z. Anorg. Allg. Chem. **2012**, 638, 2081–2086; b) X. Li, J. Liang, J. Luo, M. Norouzi Banis, C. Wang, W. Li, S. Deng, C. Yu, F. Zhao, Y. Hu, T.-K. Sham, L. Zhang, S. Zhao, S. Lu, H. Huang, R. Li, K. R. Adair, X. Sun, *Energy Environ. Sci.* **2019**, 12, 2665–2671.
- [15] Y. Xiao, Y. Wang, S.-H. Bo, J. C. Kim, L. J. Miara, G. Ceder, *Nat. Rev. Mater.* **2020**, 5, 105–126.
- [16] a) W. D. Richards, L. J. Miara, Y. Wang, J. C. Kim, G. Ceder, *Chem. Mater.* **2016**, 28, 266–273; b) H.-D. Lim, J.-H. Park, H.-J. Shin, J. Jeong, J. T. Kim, K.-W. Nam, H.-G. Jung, K. Y. Chung, *Energy Storage Mater.* **2020**, 25, 224–250; c) S. Wenzel, T. Leichtweiss, D. Krüger, J. Sann, J. Janek, *Solid State Ionics* **2015**, 278, 98–105.
- [17] Y. Zhu, X. He, Y. Mo, *J. Mater. Chem. A* **2016**, 4, 3253–3266.
- [18] T. Minami, A. Hayashi, M. Tatsumisago, *Solid State Ionics* **2000**, 136–137, 1015–1023.
- [19] a) R. Kanno, M. Murayama, *J. Electrochem. Soc.* **2001**, 148, A742–A746; b) T. Ohtomo, A. Hayashi, M. Tatsumisago, Y. Tsuchida, S. Hama, K. Kawamoto, *J. Power Sources* **2013**, 233, 231–235; c) Z. Zhang, J. H. Kennedy, *Solid State Ionics* **1990**, 38, 217–224.
- [20] H. Yamane, M. Shibata, Y. Shimane, T. Junke, Y. Seino, S. Adams, K. Minami, A. Hayashi, M. Tatsumisago, *Solid State Ionics* **2007**, 178, 1163–1167.
- [21] C. Dietrich, D. A. Weber, S. J. Sedlmaier, S. Idris, S. P. Culver, D. Walter, J. Janek, W. G. Zeier, *J. Mater. Chem. A* **2017**, 5, 18111–18119.
- [22] S. T. Kong, Ö. Gün, B. Koch, H. J. Deisereth, H. Eckert, C. Reiner, *Chem. Eur. J.* **2010**, 16, 5138–5147.
- [23] R. Mercier, J. P. Malugani, B. Fahys, J. Douglade, G. Robert, *J. Solid State Chem.* **1982**, 43, 151–162.
- [24] Z. Liu, W. Fu, E. A. Payzant, X. Yu, Z. Wu, N. J. Dudney, J. Kiggans, K. Hong, A. J. Rondinone, C. Liang, *J. Am. Chem. Soc.* **2013**, 135, 975–978.
- [25] a) Ö. U. Kudu, T. Famprakis, B. Fleutot, M.-D. Braida, T. Le Mercier, M. S. Islam, C. Masquelier, *J. Power Sources* **2018**, 407, 31–43; b) F. Mizuno, A. Hayashi, K. Tadanaga, M. Tatsumisago, *Solid State Ionics* **2006**, 177, 2721–2725.
- [26] Y. Seino, T. Ota, K. Takada, A. Hayashi, M. Tatsumisago, *Energy Environ. Sci.* **2014**, 7, 627–631.
- [27] K. Takada, T. Inada, A. Kajiyama, H. Sasaki, S. Kondo, M. Watanabe, M. Murayama, R. Kanno, *Solid State Ionics* **2003**, 158, 269–274.
- [28] a) R. Kanno, T. Hata, Y. Kawamoto, M. Irie, *Solid State Ionics* **2000**, 130, 97–104; b) Z. Liu, F. Huang, J. Yang, B. Wang, J. Sun, *Solid State Ionics* **2008**, 179, 1714–1716; c) K. Homma, M. Yonemura, T. Kobayashi, M. Nagao, M. Hirayama, R. Kanno, *Solid State Ionics* **2011**, 182, 53–58.
- [29] N. Kamaya, K. Homma, Y. Yamakawa, M. Hirayama, R. Kanno, M. Yonemura, T. Kamiyama, Y. Kato, S. Hama, K. Kawamoto, A. Mitsui, *Nat. Mater.* **2011**, 10, 682–686.
- [30] S. P. Ong, Y. Mo, W. D. Richards, L. Miara, H. S. Lee, G. Ceder, *Energy Environ. Sci.* **2013**, 6, 148–156.
- [31] T. Kaib, S. Haddadpour, M. Kapitein, P. Bron, C. Schröder, H. Eckert, B. Roling, S. Dehnen, *Chem. Mater.* **2012**, 24, 2211–2219.
- [32] Y. Mo, S. P. Ong, G. Ceder, *Chem. Mater.* **2012**, 24, 15–17.
- [33] P. Bron, S. Johansson, K. Zick, J. Schmedt auf der Günne, S. Dehnen, B. Roling, *J. Am. Chem. Soc.* **2013**, 135, 15694–15697.
- [34] Y. Kato, S. Hori, T. Saito, K. Suzuki, M. Hirayama, A. Mitsui, M. Yonemura, H. Iba, R. Kanno, *Nat. Energy* **2016**, 1, 16030.
- [35] a) J. Zhang, C. Zheng, J. Lou, Y. Xia, C. Liang, H. Huang, Y. Gan, X. Tao, W. Zhang, *J. Power Sources* **2019**, 412, 78–85; b) J. Zhang, H. Zhong, C. Zheng, Y. Xia, C. Liang, H. Huang, Y. Gan, X. Tao, W. Zhang, *J. Power Sources* **2018**, 391, 73–79; c) H.-J. Deisereth, S.-T. Kong, H. Eckert, J. Vannahme, C. Reiner, T. Zaiß, M. Schlosser, *Angew. Chem. Int. Ed.* **2008**, 47, 755–758; *Angew. Chem.* **2008**, 120, 767–770.
- [36] a) R. P. Rao, S. Adams, *Phys. Status Solidi A* **2011**, 208, 1804–1807; b) N. J. J. de Klerk, I. Rosoñ, M. Wagemaker, *Chem. Mater.* **2016**, 28, 7955–7963; c) H. M. Chen, C. Maohua, S. Adams, *Phys. Chem. Chem. Phys.* **2015**, 17, 16494–16506; d) P. R. Rayavarapu, N. Sharma, V. K. Peterson, S. Adams, *J. Solid State Electrochem.* **2012**, 16, 1807–1813.
- [37] R. Schlem, M. Ghidiu, S. P. Culver, A.-L. Hansen, W. G. Zeier, *ACS Appl. Energy Mater.* **2020**, 3, 9–18.
- [38] F. Zhao, J. Liang, C. Yu, Q. Sun, X. Li, K. Adair, C. Wang, Y. Zhao, S. Zhang, W. Li, S. Deng, R. Li, Y. Huang, H. Huang, L. Zhang, S. Zhao, S. Lu, X. Sun, *Adv. Energy Mater.* **2020**, 10, 1903422.
- [39] L. Zhou, A. Assoud, Q. Zhang, X. Wu, L. F. Nazar, *J. Am. Chem. Soc.* **2019**, 141, 19002.
- [40] T. Chen, L. Zhang, Z. Zhang, P. Li, H. Wang, C. Yu, X. Yan, L. Wang, B. Xu, *ACS Appl. Mater. Interfaces* **2019**, 11, 40808–40816.
- [41] M. A. Kraft, S. Ohno, T. Zinkevich, R. Koever, S. P. Culver, T. Fuchs, A. Senyshyn, S. Indris, B. J. Morgan, W. G. Zeier, *J. Am. Chem. Soc.* **2018**, 140, 16330–16339.
- [42] S. Chen, K. Wen, J. Fan, Y. Bando, D. Golberg, *J. Mater. Chem. A* **2018**, 6, 11631–11663.
- [43] J. B. Goodenough, H. Y. P. Hong, J. A. Kafalas, *Mater. Res. Bull.* **1976**, 11, 203–220.
- [44] C. R. Mariappan, C. Yada, F. Rosciano, B. Roling, *J. Power Sources* **2011**, 196, 6456–6464.
- [45] V. Thangadurai, W. Weppner, *Ionics* **2006**, 12, 81–92.
- [46] H. Y. P. Hong, *Mater. Res. Bull.* **1978**, 13, 117–124.
- [47] I. Abrahams, P. G. Bruce, A. R. West, W. I. F. David, *J. Solid State Chem.* **1988**, 75, 390–396.
- [48] P. G. Bruce, *J. Electrochem. Soc.* **1983**, 130, 662–669.
- [49] K. C. Santosh, R. C. Longo, K. Xiong, K. Cho, *J. Electrochem. Soc.* **2014**, 161, F3104–F3110.
- [50] T. Takahashi, H. Iwahara, *Energy Convers.* **1971**, 11, 105–111.
- [51] B. A. Boukamp, R. A. Huggins, *Mater. Res. Bull.* **1978**, 13, 23–32.
- [52] Y. Inaguma, C. Liquan, M. Itoh, T. Nakamura, T. Uchida, H. Ikuta, M. Wakihara, *Solid State Commun.* **1993**, 86, 689–693.
- [53] O. Bohnke, J. Emery, A. Veron, J. L. Fourquet, J. Y. Buzare, P. Florian, D. Massiot, *Solid State Ionics* **1998**, 109, 25–34.
- [54] S. Stramare, V. Thangadurai, W. Weppner, *Chem. Mater.* **2003**, 15, 3974–3990.

- [55] M. Yashima, M. Itoh, Y. Inaguma, Y. Morii, *J. Am. Chem. Soc.* **2005**, *127*, 3491–3495.
- [56] V. Thangadurai, H. Kaack, W. J. F. Weppner, *J. Am. Ceram. Soc.* **2003**, *86*, 437–440.
- [57] R. Murugan, V. Thangadurai, W. Weppner, *Angew. Chem. Int. Ed.* **2007**, *46*, 7778–7781; *Angew. Chem.* **2007**, *119*, 7925–7928.
- [58] A. J. Samson, K. Hofstetter, S. Bag, V. Thangadurai, *Energy Environ. Sci.* **2019**, *12*, 2957–2975.
- [59] M. Xu, M. S. Park, J. M. Lee, T. Y. Kim, Y. S. Park, E. Ma, *Phys. Rev. B* **2012**, *85*, 052301.
- [60] X. Li, J. Liang, X. Yang, K. R. Adair, C. Wang, F. Zhao, X. Sun, *Energy Environ. Sci.* **2020**, *13*, 1429–1461.
- [61] H. J. Steiner, H. D. Lutz, *Z. Anorg. Allg. Chem.* **1992**, *613*, 26–30.
- [62] T. Asano, A. Sakai, S. Ouchi, M. Sakaida, A. Miyazaki, S. Hasegawa, *Adv. Mater.* **2018**, *30*, 1803075.
- [63] X. Li, J. Liang, N. Chen, J. Luo, K. R. Adair, C. Wang, M. N. Banis, T.-K. Sham, L. Zhang, S. Zhao, S. Lu, H. Huang, R. Li, X. Sun, *Angew. Chem. Int. Ed.* **2019**, *58*, 16427–16432.
- [64] Y. Zhao, L. L. Daemen, *J. Am. Chem. Soc.* **2012**, *134*, 15042–15047.
- [65] J. Zhang, C. He, C. Duan, *Inorg. Chem. Commun.* **2014**, *49*, 140–142.
- [66] X. Lü, G. Wu, J. W. Howard, A. Chen, Y. Zhao, L. L. Daemen, Q. Jia, *Chem. Commun.* **2014**, *50*, 11520–11522.
- [67] Z. Deng, B. Radhakrishnan, S. P. Ong, *Chem. Mater.* **2015**, *27*, 3749–3755.
- [68] Y. Zhang, Y. Zhao, C. Chen, *Phys. Rev. B* **2013**, *87*, 134303.
- [69] Z. Wang, H. Xu, M. Xuan, G. Shao, *J. Mater. Chem. A* **2018**, *6*, 73–83.
- [70] a) J. B. Bates, N. J. Dudney, B. Neudecker, A. Ueda, C. D. Evans, *Solid State Ionics* **2000**, *135*, 33–45; b) Y. Hamon, A. Douard, F. Sabary, C. Marcel, P. Vinatier, B. Pecquenard, A. Levasseur, *Solid State Ionics* **2006**, *177*, 257–261.
- [71] a) S.-J. Lee, J.-H. Bae, H.-W. Lee, H.-K. Baik, S.-M. Lee, *J. Power Sources* **2003**, *123*, 61–64; b) T. Famprikis, J. Galipaud, O. Clemens, B. Pecquenard, F. Le Cras, *ACS Appl. Energy Mater.* **2019**, *2*, 4782–4791.
- [72] a) M. Matsuo, Y. Nakamori, S.-I. Oriomo, H. Maeckawa, H. Takamura, *Appl. Phys. Lett.* **2007**, *91*, 224103; b) S.-I. Oriomo, Y. Nakamori, J. R. Eliseo, A. Züttel, C. M. Jensen, *Chem. Rev.* **2007**, *107*, 4111–4132; c) A. Borgschulte, S.-I. Oriomo, *Scr. Mater.* **2007**, *56*, 823–828; d) T. Aoki, T. Ichikawa, H. Miyaoka, Y. Kojima, *J. Phys. Chem. C* **2014**, *118*, 18412–18416.
- [73] H. Maeckawa, M. Matsuo, H. Takamura, M. Ando, Y. Noda, T. Karahashi, S.-I. Oriomo, *J. Am. Chem. Soc.* **2009**, *131*, 894–895.
- [74] a) H. Liu, Z. Ren, X. Zhang, J. Hu, M. Gao, H. Pan, Y. Liu, *Chem. Mater.* **2020**, *32*, 671–678; b) T. Zhang, Y. Wang, T. Song, H. Miyaoka, K. Shinzato, H. Miyaoka, T. Ichikawa, S. Shi, X. Zhang, S. Isobe, N. Hashimoto, Y. Kojima, *Joule* **2018**, *2*, 1522–1533.
- [75] D. Sveinbjörnsson, J. S. G. Myrdal, D. Blanchard, J. J. Bentzen, T. Hirata, M. B. Mogensen, P. Norby, S.-I. Oriomo, T. Vegge, *J. Phys. Chem. C* **2013**, *117*, 3249–3257.
- [76] Y. Zhu, X. He, Y. Mo, *ACS Appl. Mater. Interfaces* **2015**, *7*, 23685–23693.
- [77] a) M. Ue, *J. Electrochim. Soc.* **1994**, *141*, 2989–2996; b) K. R. Ward, R. G. Compton, *J. Electroanal. Chem.* **2014**, *724*, 43–47; c) Y. Sun, K. Suzuki, K. Hara, S. Horii, T.-A. Yano, M. Hara, M. Hirayama, R. Kanno, *J. Power Sources* **2016**, *324*, 798–803.
- [78] a) J. Trevey, J. S. Jang, Y. S. Jung, C. R. Stoldt, S.-H. Lee, *Electrochim. Commun.* **2009**, *11*, 1830–1833; b) B. R. Shin, Y. J. Nam, D. Y. Oh, D. H. Kim, J. W. Kim, Y. S. Jung, *Electrochim. Acta* **2014**, *146*, 395–402; c) S. Hori, K. Suzuki, M. Hirayama, Y. Kato, T. Saito, M. Yonemura, R. Kanno, *Faraday Discuss.* **2014**, *176*, 83–94; d) S. Boulineau, M. Courty, J.-M. Tarascon, V. Viallet, *Solid State Ionics* **2012**, *221*, 1–5.
- [79] G. F. Dewald, S. Ohno, M. A. Kraft, R. Koerver, P. Till, N. M. Vargas-Barbosa, J. Janek, W. G. Zeier, *Chem. Mater.* **2019**, *31*, 8328–8337.
- [80] L. Sang, R. T. Haasch, A. A. Gewirth, R. G. Nuzzo, *Chem. Mater.* **2017**, *29*, 3029–3037.
- [81] T. K. Schwietert, V. A. Arszelewski, C. Wang, C. Yu, A. Vasileiadis, N. J. J. de Klerk, J. Hageman, T. Hupfer, I. Kerkamm, Y. Xu, E. van der Maas, E. M. Kelder, S. Ganapathy, M. Wagemaker, *Nat. Mater.* **2020**, *19*, 428–435.
- [82] F. Han, Y. Zhu, X. He, Y. Mo, C. Wang, *Adv. Energy Mater.* **2016**, *6*, 1501590.
- [83] S. Wang, Q. Bai, A. M. Nolan, Y. Liu, S. Gong, Q. Sun, Y. Mo, *Angew. Chem. Int. Ed.* **2019**, *58*, 8039–8043.
- [84] Z. Xu, X. Chen, K. Liu, R. Chen, X. Zeng, H. Zhu, *Chem. Mater.* **2019**, *31*, 7425–7433.
- [85] X. Lü, J. W. Howard, A. Chen, J. Zhu, S. Li, G. Wu, P. Dowden, H. Xu, Y. Zhao, Q. Jia, *Adv. Sci.* **2016**, *3*, 1500359.
- [86] X. Huang, Y. Lu, Z. Song, T. Xiu, M. E. Badding, Z. Wen, *J. Energy Chem.* **2019**, *39*, 8–16.
- [87] A. Paolella, W. Zhu, G. Bertoni, S. Savoie, Z. Feng, H. Demers, V. Gariepy, G. Girard, E. Rivard, N. Delaporte, A. Guerfi, H. Lorrmann, C. George, K. Zaghib, *ACS Appl. Energy Mater.* **2020**, *3*, 3415–3424.
- [88] J. Su, X. Huang, Z. Song, T. Xiu, M. E. Badding, J. Jin, Z. Wen, *Ceram. Int.* **2019**, *45*, 14991–14996.
- [89] Q. Liu, Z. Geng, C. Han, Y. Fu, S. Li, Y.-b. He, F. Kang, B. Li, *J. Power Sources* **2018**, *389*, 120–134.
- [90] J. Sakamoto, E. Rangasamy, H. Kim, Y. Kim, J. Wolfenstine, *Nanotechnology* **2013**, *24*, 424005.
- [91] Y. Jin, P. J. McGinn, *J. Power Sources* **2013**, *239*, 326–331.
- [92] W. Xia, B. Xu, H. Duan, Y. Guo, H. Kang, H. Li, H. Liu, *ACS Appl. Mater. Interfaces* **2016**, *8*, 5335–5342.
- [93] W. Zhou, Y. Zhu, N. Grundish, X. Sen, S. Wang, Y. You, N. Wu, J. Gao, Z. Cui, Y. Li, J. B. Goodenough, *Nano Energy* **2018**, *53*, 926–931.
- [94] Y. Shen, Y. Zhang, S. Han, J. Wang, Z. Peng, L. Chen, *Joule* **2018**, *2*, 1674–1689.
- [95] H. Zhang, S. Hao, J. Lin, *J. Alloys Compd.* **2017**, *704*, 109–116.
- [96] K. Kerman, A. Luntz, V. Viswanathan, Y.-M. Chiang, Z. Chen, *J. Electrochim. Soc.* **2017**, *164*, A1731–A1744.
- [97] J. A. Dawson, P. Canepa, T. Famprikis, C. Masquelier, M. S. Islam, *J. Am. Chem. Soc.* **2018**, *140*, 362–368.
- [98] F. Han, T. Gao, Y. Zhu, K. J. Gaskell, C. Wang, *Adv. Mater.* **2015**, *27*, 3473–3483.
- [99] a) T. Hakari, M. Nagao, A. Hayashi, M. Tatsumisago, *J. Power Sources* **2015**, *293*, 721–725; b) T. Hakari, M. Nagao, A. Hayashi, M. Tatsumisago, *Solid State Ionics* **2014**, *262*, 147–150; c) Y. Zhang, R. Chen, T. Liu, B. Xu, X. Zhang, L. Li, Y. Lin, C.-W. Nan, Y. Shen, *ACS Appl. Mater. Interfaces* **2018**, *10*, 10029–10035; d) D. H. S. Tan, E. A. Wu, H. Nguyen, Z. Chen, M. A. T. Marple, J.-M. Doux, X. Wang, H. Yang, A. Banerjee, Y. S. Meng, *ACS Energy Lett.* **2019**, *4*, 2418–2427.
- [100] a) S. Wang, X. Xu, X. Zhang, C. Xin, B. Xu, L. Li, Y.-H. Lin, Y. Shen, B. Li, C.-W. Nan, *J. Mater. Chem. A* **2019**, *7*, 18612–18618; b) C. Yu, J. Hageman, S. Ganapathy, L. van Eijck, L. Zhang, K. R. Adair, X. Sun, M. Wagemaker, *J. Mater. Chem. A* **2019**, *7*, 10412–10421.
- [101] M. Sumita, Y. Tanaka, T. Ohno, *J. Phys. Chem. C* **2017**, *121*, 9698–9704.
- [102] A. Sakuda, A. Hayashi, M. Tatsumisago, *Chem. Mater.* **2010**, *22*, 949–956.
- [103] J. Auvergniot, A. Cassel, J.-B. Ledueil, V. Viallet, V. Seznec, R. Dedryvère, *Chem. Mater.* **2017**, *29*, 3883–3890.
- [104] C. Wang, X. Li, Y. Zhao, M. N. Banis, J. Liang, X. Li, Y. Sun, K. R. Adair, Q. Sun, Y. Liu, F. Zhao, S. Deng, X. Lin, R. Li, Y. Hu, T.-K. Sham, H. Huang, L. Zhang, R. Yang, S. Lu, X. Sun, *Small Methods* **2019**, *3*, 1900261.
- [105] a) J. Zhang, C. Zheng, L. Li, Y. Xia, H. Huang, Y. Gan, C. Liang, X. He, X. Tao, W. Zhang, *Adv. Energy Mater.* **2020**, *10*, 1903311; b) D. Cao, Y. Zhang, A. M. Nolan, X. Sun, C. Liu, J. Sheng, Y. Mo, Y. Wang, H. Zhu, *Nano Lett.* **2020**, *20*, 1483–1490; c) S. H. Jung, U.-H. Kim, J.-H. Kim, S. Jun, C. S. Yoon, Y. S. Jung, Y.-K. Sun, *Adv. Energy Mater.* **2020**, *10*, 1903360.
- [106] X. Li, Z. Ren, M. Norouzi Banis, S. Deng, Y. Zhao, Q. Sun, C. Wang, X. Yang, W. Li, J. Liang, X. Li, Y. Sun, K. Adair, R. Li, Y. Hu, T.-K. Sham, H. Huang, L. Zhang, S. Lu, J. Luo, X. Sun, *ACS Energy Lett.* **2019**, *4*, 2480–2488.
- [107] a) R. Koerver, I. Aygün, T. Leichtweiß, C. Dietrich, W. Zhang, J. O. Binder, P. Hartmann, W. G. Zeier, J. Janek, *Chem. Mater.* **2017**, *29*, 5574–5582; b) S. Ohno, R. Koerver, G. Dewald, C. Rosenbach, P. Titscher, D. Steckermeier, A. Kwade, J. Janek, W. G. Zeier, *Chem. Mater.* **2019**, *31*, 2930–2940.
- [108] X. Zhan, S. Lai, M. P. Gobet, S. G. Greenbaum, M. Shirpour, *Phys. Chem. Chem. Phys.* **2018**, *20*, 1447–1459.
- [109] L. J. Miara, W. D. Richards, Y. E. Wang, G. Ceder, *Chem. Mater.* **2015**, *27*, 4040–4047.
- [110] K. H. Kim, Y. Iriyama, K. Yamamoto, S. Kumazaki, T. Asaka, K. Tanabe, C. A. J. Fisher, T. Hirayama, R. Murugan, Z. Ogumi, *J. Power Sources* **2011**, *196*, 764–767.
- [111] K. Park, B.-C. Yu, J.-W. Jung, Y. Li, W. Zhou, H. Gao, S. Son, J. B. Goodenough, *Chem. Mater.* **2016**, *28*, 8051–8059.
- [112] L. Miara, A. Windmüller, C.-L. Tsai, W. D. Richards, Q. Ma, S. Uhlenbruck, O. Guillou, G. Ceder, *ACS Appl. Mater. Interfaces* **2016**, *8*, 26842–26850.
- [113] A. A. Delluva, J. Dudoff, G. Teeter, A. Holewinski, *ACS Appl. Mater. Interfaces* **2020**, *12*, 24992–24999.
- [114] C.-Y. Yu, J. Choi, V. Anandan, J.-H. Kim, *J. Phys. Chem. C* **2020**, *124*, 14963–14971.

- [115] Z. Wang, D. Santhanagopalan, W. Zhang, F. Wang, H. L. Xin, K. He, J. Li, N. Dudney, Y. S. Meng, *Nano Lett.* **2016**, *16*, 3760–3767.
- [116] W. Xu, J. Wang, F. Ding, X. Chen, E. Nasibulin, Y. Zhang, J.-G. Zhang, *Energy Environ. Sci.* **2014**, *7*, 513–537.
- [117] S. Ito, S. Fujiki, T. Yamada, Y. Aihara, Y. Park, T. Y. Kim, S.-W. Baek, J.-M. Lee, S. Doo, N. Machida, *J. Power Sources* **2014**, *248*, 943–950.
- [118] P.-H. Chien, X. Feng, M. Tang, J. T. Rosenberg, S. O'Neill, J. Zheng, S. C. Grant, Y.-Y. Hu, *J. Phys. Chem. Lett.* **2018**, *9*, 1990–1998.
- [119] a) S. Wenzel, D. A. Weber, T. Leichtweiss, M. R. Busche, J. Sann, J. Janek, *Solid State Ionics* **2016**, *286*, 24–33; b) S. Wenzel, S. Randau, T. Leichtweiss, D. A. Weber, J. Sann, W. G. Zeier, J. Janek, *Chem. Mater.* **2016**, *28*, 2400–2407; c) S. Wenzel, S. J. Sedlmaier, C. Dietrich, W. G. Zeier, J. Janek, *Solid State Ionics* **2018**, *318*, 102–112.
- [120] M. Sakuma, K. Suzuki, M. Hirayama, R. Kanno, *Solid State Ionics* **2016**, *285*, 101–105.
- [121] F. Han, A. S. Westover, J. Yue, X. Fan, F. Wang, M. Chi, D. N. Leonard, N. J. Dudney, H. Wang, C. Wang, *Nat. Energy* **2019**, *4*, 187–196.
- [122] N. Seitzman, H. Guthrey, D. B. Sulas, H. A. S. Platt, M. Al-Jassim, S. Pylypenko, *J. Electrochem. Soc.* **2018**, *165*, A3732–A3737.
- [123] K. N. Wood, K. X. Steirer, S. E. Hafner, C. Ban, S. Santhanagopalan, S.-H. Lee, G. Teeter, *Nat. Commun.* **2018**, *9*, 2490.
- [124] W. Xia, B. Xu, H. Duan, X. Tang, Y. Guo, H. Kang, H. Li, H. Liu, *J. Am. Ceram. Soc.* **2017**, *100*, 2832–2839.
- [125] J. Zhu, J. Zhao, Y. Xiang, M. Lin, H. Wang, B. Zheng, H. He, Q. Wu, J. Y. Huang, Y. Yang, *Chem. Mater.* **2020**, *32*, 4998–5008.
- [126] X. Fan, X. Ji, F. Han, J. Yue, J. Chen, L. Chen, T. Deng, J. Jiang, C. Wang, *Sci. Adv.* **2018**, *4*, eaau9245.
- [127] Q. Yu, D. Han, Q. Lu, Y.-B. He, S. Li, Q. Liu, C. Han, F. Kang, B. Li, *ACS Appl. Mater. Interfaces* **2019**, *11*, 9911–9918.
- [128] J.-Y. Liang, X.-X. Zeng, X.-D. Zhang, T.-T. Zuo, M. Yan, Y.-X. Yin, J.-L. Shi, X.-W. Wu, Y.-G. Guo, L.-J. Wan, *J. Am. Chem. Soc.* **2019**, *141*, 9165–9169.
- [129] Q. Cheng, A. Li, N. Li, S. Li, A. Zangiabadi, T.-D. Li, W. Huang, A. C. Li, T. Jin, Q. Song, W. Xu, N. Ni, H. Zhai, M. Dontigny, K. Zaghib, X. Chuan, D. Su, K. Yan, Y. Yang, *Joule* **2019**, *3*, 1510–1522.
- [130] a) Y. J. Nam, S.-J. Cho, D. Y. Oh, J.-M. Lim, S. Y. Kim, J. H. Song, Y.-G. Lee, S.-Y. Lee, Y. S. Jung, *Nano Lett.* **2015**, *15*, 3317–3323; b) K. Minami, A. Hayashi, S. Ujiiie, M. Tatsumisago, *Solid State Ionics* **2011**, *192*, 122–125.
- [131] X. Ma, Y. Xu, B. Zhang, X. Xue, C. Wang, S. He, J. Lin, L. Yang, *J. Power Sources* **2020**, *453*, 227881.
- [132] M. Yamamoto, Y. Terauchi, A. Sakuda, M. Takahashi, *J. Power Sources* **2018**, *402*, 506–512.
- [133] Y. Sun, K. Suzuki, S. Hori, M. Hirayama, R. Kanno, *Chem. Mater.* **2017**, *29*, 5858–5864.
- [134] L. Yang, Q. Dai, L. Liu, D. Shao, K. Luo, S. Jamil, H. Liu, Z. Luo, B. Chang, X. Wang, *Ceram. Int.* **2020**, *46*, 10917–10924.
- [135] M. Sumita, Y. Tanaka, M. Ikeda, T. Ohno, *J. Phys. Chem. C* **2016**, *120*, 13332–13339.
- [136] Z. Liu, A. Borodin, G. Li, X. Liu, Y. Li, F. Endres, *J. Phys. Chem. C* **2020**, *124*, 300–308.
- [137] a) J. Wei, H. Kim, D.-C. Lee, R. Hu, F. Wu, H. Zhao, F. M. Alamgir, G. Yushin, *J. Power Sources* **2015**, *294*, 494–500; b) X. Xu, K. S. Hui, K. N. Hui, H. Wang, J. Liu, *Mater. Horiz.* **2020**, *7*, 1246–1278; c) R. C. Xu, X. H. Xia, X. L. Wang, Y. Xia, J. P. Tu, *J. Mater. Chem. A* **2017**, *5*, 2829–2834; d) R. C. Xu, X. H. Xia, S. H. Li, S. Z. Zhang, X. L. Wang, J. P. Tu, *J. Mater. Chem. A* **2017**, *5*, 63106317.
- [138] J. Lau, R. H. DeBlock, D. M. Butts, D. S. Ashby, C. S. Choi, B. S. Dunn, *Adv. Energy Mater.* **2018**, *8*, 1800933.
- [139] M. Murayama, R. Kanno, M. Irie, S. Ito, T. Hata, N. Sonoyama, Y. Kawamoto, *J. Solid State Chem.* **2002**, *168*, 140–148.
- [140] a) D. Xie, S. Chen, Z. Zhang, J. Ren, L. Yao, L. Wu, X. Yao, X. Xu, *J. Power Sources* **2018**, *389*, 140–147; b) Z. Zhang, Y. Sun, X. Duan, L. Peng, H. Jia, Y. Zhang, B. Shan, J. Xie, *J. Mater. Chem. A* **2019**, *7*, 2717–2722.
- [141] S. Banerjee, X. Zhang, L.-W. Wang, *Chem. Mater.* **2019**, *31*, 7265–7276.
- [142] Z. Wu, Z. Xie, A. Yoshida, X. An, Z. Wang, X. Hao, A. Abudula, G. Guan, *Chem. Eng. J.* **2020**, *380*, 122419.
- [143] H. Wang, C. Yu, S. Ganapathy, E. R. H. van Eck, L. van Eijck, M. Wagemaker, *J. Power Sources* **2019**, *412*, 29–36.
- [144] K. B. Dermenci, E. Çekiç, S. Turan, *Int. J. Hydrogen Energy* **2016**, *41*, 9860–9867.
- [145] C. Deviannapoorni, L. S. Shankar, S. Ramakumar, R. Murugan, *Ionics* **2016**, *22*, 1281–1289.
- [146] F. Du, N. Zhao, Y. Li, C. Chen, Z. Liu, X. Guo, *J. Power Sources* **2015**, *300*, 24–28.
- [147] T. Teranishi, M. Yamamoto, H. Hayashi, A. Kishimoto, *Solid State Ionics* **2013**, *243*, 18–21.
- [148] H. T. T. Le, R. S. Kalubarme, D. T. Ngo, S.-Y. Jang, K.-N. Jung, K.-H. Shin, C.-J. Park, *J. Power Sources* **2015**, *274*, 1188–1199.
- [149] L. Yue, J. Ma, J. Zhang, J. Zhao, S. Dong, Z. Liu, G. Cui, L. Chen, *Energy Storage Mater.* **2016**, *5*, 139–164.
- [150] Y. Zhao, C. Wu, G. Peng, X. Chen, X. Yao, Y. Bai, F. Wu, S. Chen, X. Xu, *J. Power Sources* **2016**, *301*, 47–53.
- [151] J. Zheng, P. Wang, H. Liu, Y.-Y. Hu, *ACS Appl. Energy Mater.* **2019**, *2*, 1452–1459.
- [152] L. Cong, Y. Li, W. Lu, J. Jie, Y. Liu, L. Sun, H. Xie, *J. Power Sources* **2020**, *446*, 227365.
- [153] I. Villaluenga, K. H. Wujcik, W. Tong, D. Devaux, D. H. C. Wong, J. M. DeSimone, N. P. Balsara, *Proc. Mont. Acad. Sci.* **2016**, *113*, 52–57.
- [154] X. Li, D. Wang, H. Wang, H. Yan, Z. Gong, Y. Yang, *ACS Appl. Mater. Interfaces* **2019**, *11*, 22745–22753.
- [155] J. Ju, Y. Wang, B. Chen, J. Ma, S. Dong, J. Chai, H. Qu, L. Cui, X. Wu, G. Cui, *ACS Appl. Mater. Interfaces* **2018**, *10*, 13588–13579.
- [156] F. J. Simon, M. Hanauer, F. H. Richter, J. Janek, *ACS Appl. Mater. Interfaces* **2020**, *12*, 11713–11723.
- [157] S. Chen, J. Wang, Z. Zhang, L. Wu, L. Yao, Z. Wei, Y. Deng, D. Xie, X. Yao, X. Xu, *J. Power Sources* **2018**, *387*, 72–80.
- [158] Z. Wan, D. Lei, W. Yang, C. Liu, K. Shi, X. Hao, L. Shen, W. Lv, B. Li, Q.-H. Yang, F. Kang, Y.-B. He, *Adv. Funct. Mater.* **2019**, *29*, 1805301.
- [159] A. Li, X. Liao, H. Zhang, L. Shi, P. Wang, Q. Cheng, J. Borovilas, Z. Li, W. Huang, Z. Fu, M. Dontigny, K. Zaghib, K. Myers, X. Chuan, X. Chen, Y. Yang, *Adv. Mater.* **2020**, *32*, 1905517.
- [160] J. Bae, Y. Li, J. Zhang, X. Zhou, F. Zhao, Y. Shi, J. B. Goodenough, G. Yu, *Angew. Chem. Int. Ed.* **2018**, *57*, 2096–2100; *Angew. Chem.* **2018**, *130*, 2118–2122.
- [161] Y. Tao, S. Chen, D. Liu, G. Peng, X. Yao, X. Xu, *J. Electrochem. Soc.* **2015**, *163*, A96–A101.
- [162] X. Yao, N. Huang, F. Han, Q. Zhang, H. Wan, J. P. Mwizerwa, C. Wang, X. Xu, *Adv. Energy Mater.* **2017**, *7*, 1602923.
- [163] Q. Zhang, H. Wan, G. Liu, Z. Ding, J. P. Mwizerwa, X. Yao, *Nano Energy* **2019**, *57*, 771–782.
- [164] H. Wan, G. Peng, X. Yao, J. Yang, P. Cui, X. Xu, *Energy Storage Mater.* **2016**, *4*, 59–65.
- [165] W. Zhou, S. Wang, Y. Li, S. Xin, A. Manthiram, J. B. Goodenough, *J. Am. Chem. Soc.* **2016**, *138*, 9385–9388.
- [166] N. Ohta, K. Takada, L. Zhang, R. Ma, M. Osada, T. Sasaki, *Adv. Mater.* **2006**, *18*, 2226–2229.
- [167] N. Ohta, K. Takada, I. Sakaguchi, L. Zhang, R. Ma, K. Fukuda, M. Osada, T. Sasaki, *Electrochim. Commun.* **2007**, *9*, 1486–1490.
- [168] a) X. Li, L. Jin, D. Song, H. Zhang, X. Shi, Z. Wang, L. Zhang, L. Zhu, *J. Energy Chem.* **2020**, *40*, 39–45; b) G. Oh, M. Hirayama, O. Kwon, K. Suzuki, R. Kanno, *Chem. Mater.* **2016**, *28*, 2634–2640; c) A. Sakuda, H. Kitaura, A. Hayashi, K. Tadanaga, M. Tatsumisago, *J. Power Sources* **2009**, *189*, 527–530; d) S. Deng, X. Li, Z. Ren, W. Li, J. Luo, J. Liang, J. Liang, M. N. Banis, M. Li, Y. Zhao, X. Li, C. Wang, Y. Sun, Q. Sun, R. Li, Y. Hu, H. Huang, L. Zhang, S. Lu, J. Luo, X. Sun, *Energy Storage Mater.* **2020**, *27*, 117–123.
- [169] A. Sakuda, A. Hayashi, M. Tatsumisago, *Sci. Rep.* **2013**, *3*, 2261.
- [170] M. Otoyama, A. Sakuda, M. Tatsumisago, A. Hayashi, *ACS Appl. Mater. Interfaces* **2020**, *12*, 29228–29234.
- [171] M. Ogawa, R. Kanda, K. Yoshida, T. Uemura, K. Harada, *J. Power Sources* **2012**, *205*, 487–490.
- [172] Z. Zhang, S. Chen, J. Yang, J. Wang, L. Yao, X. Yao, P. Cui, X. Xu, *ACS Appl. Mater. Interfaces* **2018**, *10*, 2556–2565.
- [173] R. Xu, F. Han, X. Ji, X. Fan, J. Tu, C. Wang, *Nano Energy* **2018**, *53*, 958–966.
- [174] M. Nagao, A. Hayashi, M. Tatsumisago, *Electrochemistry* **2012**, *80*, 734–736.
- [175] a) A. Kato, A. Hayashi, M. Tatsumisago, *J. Power Sources* **2016**, *309*, 27–32; b) A. Kato, M. Suyama, C. Hotehama, H. Kowada, A. Sakuda, A. Hayashi, M. Tatsumisago, *J. Electrochem. Soc.* **2018**, *165*, A1950–A1954.
- [176] L. Sang, K. L. Bassett, F. C. Castro, M. J. Young, L. Chen, R. T. Haasch, J. W. Elam, V. P. Dravid, R. G. Nuzzo, A. A. Gewirth, *Chem. Mater.* **2018**, *30*, 8747–8756.
- [177] F. J. Simon, M. Hanauer, A. Henss, F. H. Richter, J. Janek, *ACS Appl. Mater. Interfaces* **2019**, *11*, 42186–42196.
- [178] S. Choi, M. Jeon, W. D. Jung, S. Yang, S. Park, H.-I. Ji, J.-H. Lee, B.-K. Kim, B.-I. Sang, H. Kim, *Solid State Ionics* **2020**, *346*, 115217.
- [179] C. Wang, Y. Zhao, Q. Sun, X. Li, Y. Liu, J. Liang, X. Li, X. Lin, R. Li, K. R. Adair, L. Zhang, R. Yang, S. Lu, X. Sun, *Nano Energy* **2018**, *53*, 168–174.

- [180] Y.-G. Lee, S. Fujiki, C. Jung, N. Suzuki, N. Yashiro, R. Omoda, D.-S. Ko, T. Shiratsuchi, T. Sugimoto, S. Ryu, J. H. Ku, T. Watanabe, Y. Park, Y. Aihara, D. Im, I. T. Han, *Nat. Energy* **2020**, *5*, 299–308.
- [181] J. Liu, T. Liu, Y. Pu, M. Guan, Z. Tang, F. Ding, Z. Xu, Y. Li, *RSC Adv.* **2017**, *7*, 46545–46552.
- [182] X. Hao, Q. Zhao, S. Su, S. Zhang, J. Ma, L. Shen, Q. Yu, L. Zhao, Y. Liu, F. Kang, Y.-B. He, *Adv. Energy Mater.* **2019**, *9*, 1901604.
- [183] X. Han, Y. Gong, K. Fu, X. He, G. T. Hitz, J. Dai, A. Pearse, B. Liu, H. Wang, G. Rubloff, Y. Mo, V. Thangadurai, E. D. Wachsman, L. Hu, *Nat. Mater.* **2017**, *16*, 572–579.
- [184] J. Lou, G. Wang, Y. Xia, C. Liang, H. Huang, Y. Gan, X. Tao, J. Zhang, W. Zhang, *J. Power Sources* **2020**, *448*, 227440.
- [185] J. Fu, P. Yu, N. Zhang, G. Ren, S. Zheng, W. Huang, X. Long, H. Li, X. Liu, *Energy Environ. Sci.* **2019**, *12*, 1404–1412.
- [186] X. Zhang, Q. Xiang, S. Tang, A. Wang, X. Liu, J. Luo, *Nano Lett.* **2020**, *20*, 2871–2878.
- [187] Y. Liu, C. Li, B. Li, H. Song, Z. Cheng, M. Chen, P. He, H. Zhou, *Adv. Energy Mater.* **2018**, *8*, 1702374.
- [188] F. Han, J. Yue, X. Fan, T. Gao, C. Luo, Z. Ma, L. Suo, C. Wang, *Nano Lett.* **2016**, *16*, 4521–4527.
- [189] R. C. Xu, X. L. Wang, S. Z. Zhang, Y. Xia, X. H. Xia, J. B. Wu, J. P. Tu, *J. Power Sources* **2018**, *374*, 107–112.
- [190] D. H. Kim, D. Y. Oh, K. H. Park, Y. E. Choi, Y. J. Nam, H. A. Lee, S.-M. Lee, Y. S. Jung, *Nano Lett.* **2017**, *17*, 3013–3020.
- [191] Y. E. Choi, K. H. Park, D. H. Kim, D. Y. Oh, H. R. Kwak, Y.-G. Lee, Y. S. Jung, *ChemSusChem* **2017**, *10*, 2605–2611.
- [192] N. H. H. Phuc, K. Morikawa, T. Mitsuhiro, H. Muto, A. Matsuda, *Ionics* **2017**, *23*, 2061–2067.
- [193] Y. B. Song, D. H. Kim, H. Kwak, D. Han, S. Kang, J. H. Lee, S.-M. Bak, K.-W. Nam, H.-W. Lee, Y. S. Jung, *Nano Lett.* **2020**, *20*, 4337–4345.
- [194] B. Liu, K. Fu, Y. Gong, C. Yang, Y. Yao, Y. Wang, C. Wang, Y. Kuang, G. Pastel, H. Xie, E. D. Wachsman, L. Hu, *Nano Lett.* **2017**, *17*, 4917–4923.
- [195] S. Ohta, J. Seki, Y. Yagi, Y. Kihira, T. Tani, T. Asaoka, *J. Power Sources* **2014**, *265*, 40–44.
- [196] J. H. Kennedy, Z. Zhang, H. Eckert, *J. Non-Cryst. Solids* **1990**, *123*, 328–338.
- [197] H.-J. Deiseroth, J. Maier, K. Weichert, V. Nickel, S.-T. Kong, C. Reiner, Z. Anorg. Allg. Chem. **2011**, *637*, 1287–1294.
- [198] N. Minafra, S. P. Culver, T. Krauskopf, A. Senyshyn, W. G. Zeier, *J. Mater. Chem. A* **2018**, *6*, 645–651.
- [199] A. Morata-Orrantia, S. García-Martín, E. Morán, M. Á. Alario-Franco, *Chem. Mater.* **2002**, *14*, 2871–2875.
- [200] a) K. Arbi, J. M. Rojo, J. Sanz, *J. Eur. Ceram. Soc.* **2007**, *27*, 4215; b) L. Fan, S. Wei, S. Li, Q. Li, Y. Lu, *Adv. Energy Mater.* **2018**, *8*, 1702657.
- [201] J. Fu, *Solid State Ionics* **1997**, *104*, 191–194.
- [202] V. Thangadurai, W. Weppner, *Adv. Funct. Mater.* **2005**, *15*, 107–112.
- [203] J. Gao, J. Zhu, X. Li, J. Li, X. Guo, H. Li, W. Zhou, *Adv. Funct. Mater.* **2020**, 2001918.
- [204] Y. Li, W. Zhou, S. Xin, S. Li, J. Zhu, X. Lü, Z. Cui, Q. Jia, J. Zhou, Y. Zhao, J. B. Goodenough, *Angew. Chem. Int. Ed.* **2016**, *55*, 9965–9968; *Angew. Chem.* **2016**, *128*, 10119–10122.
- [205] Y. Tomita, H. Matsushita, K. Kobayashi, Y. Maeda, K. Yamada, *Solid State Ionics* **2008**, *179*, 867–870.
- [206] X. Yu, J. B. Bates, G. E. Jellison Jr., F. X. Hart, *J. Electrochem. Soc.* **1997**, *144*, 524–532.
- [207] K. Chen, K. Yamamoto, Y. Orikasa, T. Uchiyama, Y. Ito, S. Yubuchi, A. Hayashi, M. Tatsumisago, K. Nitta, T. Uruga, Y. Uchimoto, *Solid State Ionics* **2018**, *327*, 150–156.
- [208] Y. Fujii, A. Miura, N. C. Rosero-Navarro, Y. Mizuguchi, C. Moriyoshi, Y. Kuroiwa, M. Higuchi, K. Tadanaga, *J. Electrochem. Soc.* **2018**, *165*, A2948–A2954.
- [209] A. Paolella, W. Zhu, G. Bertoni, A. Perea, H. Demers, S. Savoie, G. Girard, N. Delaporte, A. Guerfi, M. Rumpel, H. Lorrmann, G. P. Demopoulos, K. Zaghib, *Adv. Mater. Interfaces* **2020**, *7*, 2000164.
- [210] G. B. Kunshina, I. V. Bocharova, V. I. Ivanenko, *Inorg. Mater.* **2020**, *56*, 204–210.
- [211] N. D. Lepley, N. A. W. Holzwarth, Y. A. Du, *Phys. Rev. B* **2013**, *88*, 104103.
- [212] A. Kato, H. Kowada, M. Deguchi, C. Hotehama, A. Hayashi, M. Tatsumisago, *Solid State Ionics* **2018**, *322*, 1–4.
- [213] R. Chen, Q. Li, X. Yu, L. Chen, H. Li, *Chem. Rev.* **2020**, *120*, 6820–6877.
- [214] A. Paolella, W. Zhu, G.-L. Xu, A. La Monaca, S. Savoie, G. Girard, A. Vijh, H. Demers, A. Perea, N. Delaporte, A. Guerfi, X. Liu, Y. Ren, C.-J. Sun, J. Lu, K. Amine, K. Zaghib, *Adv. Energy Mater.* **2020**, 2001497.
- [215] A. Schwöbel, R. Hausbrand, W. Jaegermann, *Solid State Ionics* **2015**, *273*, 51–54.
- [216] J. Kim, M. Kim, S. Noh, G. Lee, D. Shin, *Ceram. Int.* **2016**, *42*, 2140–2146.
- [217] K. Okada, N. Machida, M. Naito, T. Shigematsu, S. Ito, S. Fujiki, M. Nakano, Y. Aihara, *Solid State Ionics* **2014**, *255*, 120–127.
- [218] S. Chida, A. Miura, N. C. Rosero-Navarro, M. Higuchi, N. H. H. Phuc, H. Muto, A. Matsuda, K. Tadanaga, *Ceram. Int.* **2018**, *44*, 742–746.
- [219] J. Yi, P. He, H. Liu, H. Ni, Z. Bai, L.-Z. Fan, *J. Energy Chem.* **2021**, *52*, 202–209.
- [220] X. Li, Q. Sun, Z. Wang, D. Song, H. Zhang, X. Shi, C. Li, L. Zhang, L. Zhu, *J. Power Sources* **2020**, *456*, 227997.
- [221] Y. Seino, T. Ota, K. Takada, *J. Power Sources* **2011**, *196*, 6488–6492.
- [222] X. Li, M. Liang, J. Sheng, D. Song, H. Zhang, X. Shi, L. Zhang, *Energy Storage Mater.* **2019**, *18*, 100–106.
- [223] S. Yubuchi, Y. Ito, T. Matsuyama, A. Hayashi, M. Tatsumisago, *Solid State Ionics* **2016**, *285*, 79–82.
- [224] T. Kato, T. Hamanaka, K. Yamamoto, T. Hirayama, F. Sagane, M. Motoyama, Y. Iriyama, *J. Power Sources* **2014**, *260*, 292–298.
- [225] T. Liu, Y. Zhang, X. Zhang, L. Wang, S.-X. Zhao, Y.-H. Lin, Y. Shen, J. Luo, L. Li, C.-W. Nan, *J. Mater. Chem. A* **2018**, *6*, 4649–4657.
- [226] A. Kato, M. Suyama, C. Hotehama, H. Kowada, A. Sakuda, A. Hayashi, M. Tatsumisago, *J. Electrochem. Soc.* **2018**, *165*, A1950–A1954.
- [227] Y. Huang, B. Chen, J. Duan, F. Yang, T. Wang, Z. Wang, W. Yang, C. Hu, W. Luo, Y. Huang, *Angew. Chem. Int. Ed.* **2020**, *59*, 3699–3704.
- [228] W. Feng, X. Dong, Z. Lai, X. Zhang, Y. Wang, C. Wang, J. Luo, Y. Xia, *ACS Energy Lett.* **2019**, *4*, 1725–1731.
- [229] Y. Liu, P. He, H. Zhou, *Adv. Energy Mater.* **2018**, *8*, 1701602.
- [230] F. J. Q. Cortes, J. A. Lewis, J. Tippens, T. S. Marchese, M. T. McDowell, *J. Electrochem. Soc.* **2019**, *167*, 050502.
- [231] Q. Liu, D. Zhou, D. Shanmukaraj, P. Li, F. Kang, B. Li, M. Armand, G. Wang, *ACS Energy Lett.* **2020**, *5*, 1456–1464.

Manuscript received: June 26, 2020

Revised manuscript received: July 30, 2020

Accepted manuscript online: July 30, 2020

Version of record online: September 7, 2020